POLITECNICO DI TORINO

Corso di Laurea Magistrale
in Ingegneria Chimica e dei Processi Sostenibili

Tesi di Laurea Magistrale

SYNTHESIS AND CHARACTERIZATION OF NOVEL CATALYTIC MATERIALS FOR THE OXYGEN REDUCTION REACTION

Relatori

prof. Juqin Zeng

Corelatori

prof. Specchia Stefania

researcher Mirtha Lourenço

Candidato

Luca Basile

Contents

Riassunto in italiano per tesi in inglese

1. INTRODUZIONE

Il cambiamento climatico è un fenomeno globale che pone sfide significative al nostro pianeta e ai suoi abitanti. Negli ultimi anni, le cause e le conseguenze del cambiamento climatico sono diventate sempre più evidenti, sottolineando l'urgente necessità di agire.
L'aumento della concentrazione di gas serra nell'atmosfera negli ultimi due secoli, principalmente dovuto alla combustione di combustibili fossili è la causa principale che ha portato, e continua a portare, a un aumento delle temperature globali e ad altri cambiamenti del clima terrestre. In termini numerici, dall'inizio dell'era industriale nel XVIII secolo, le attività umane hanno aumentato l'anidride carbonica (CO_2) atmosferica del 50%, portandola a un livello pari al 150% di quello del 1750.
In sintesi, è facile capire che è necessario prendere provvedimenti radicali per preservare il nostro pianeta. Tra questi, uno dei più importanti è la produzione di energia ecosostenibile, attraverso l'utilizzo dell'idrogeno come vettore energetico nelle celle a combustibile a membrana a scambio protonico (PEMFC).
Le PEMFC sono emerse come dispositivi promettenti per la produzione di energia pulita grazie alle loro caratteristiche interessanti, quali un'elevata efficienza nella conversione dell'energia chimica in elettricità, un design compatto che porta a un'alta densità di energia, e la possibilità di emissioni quasi zero.

Tuttavia, la diffusione commerciale della tecnologia PEMFC si scontra con due sfide tecniche chiave: il costo e la durata. I catalizzatori più performanti impiegati come catodi in queste celle, secondo l'attuale stato dell'arte, sono a base di platino (Pt): l'elevato costo del Pt aumenta notevolmente i prezzi complessivi dei sistemi a celle a combustibile e, inoltre, i catalizzatori a base di Pt possono subire degradazioni e perdite di attività nel tempo, ostacolando le prestazioni e l'affidabilità a lungo termine delle celle a combustibile.
Di conseguenza, lo sviluppo di catalizzatori innovativi, più convenienti, con attività migliorata e maggiore durata rappresenta una spinta critica della ricerca nella tecnologia PEMFC.
Tra le alternative più promettenti rientrano i catalizzatori "M-N-C" a base di metalli non preziosi. Questi catalizzatori incorporano ioni metallici (come Fe, Co, ecc.) all'interno di un supporto di carbonio mesoporoso drogati con azoto.
I siti attivi per la reazione di riduzione dell'ossigeno (ORR) sono forniti dagli ioni metallici, che si coordinano con difetti e/o gruppi azotati legati alla struttura del carbonio. Allo stesso tempo, il carbonio poroso funge sia da supporto che da conduttore elettrico.
Tra i diversi metodi di sintesi, il metodo a stampo sacrificale (SSM) è particolarmente interessante per la sua semplicità ed efficacia. Tale approccio sfrutta la struttura porosa della silice come stampo (o template) sacrificale per ottenere un materiale finale con porosità controllata (grazie alla replicazione negativa della struttura porosa della silice) e siti atomicamente dispersi.

In particolare, tra i diversi tipi di catalizzatori M-N-C troviamo i cosiddetti "catalizzatori a singolo atomo". Questi risultano essere una delle alternative più promettenti in termini di efficienza di conversione, attività catalitica, e di sostenibilità. Essi sono costituiti da singoli atomi metallici isolati, ancorati individualmente agli atomi adiacenti nel materiale che funge da supporto, e rappresentano i siti attivi per le reazioni. Questi nuovi materiali hanno attirato molta attenzione per il massimo utilizzo degli atomi metallici, che consente di ridurre lo spreco di materiale e denaro, per la loro elevata selettività e attività nelle reazioni elettrochimiche, e per le loro proprietà catalitiche modulabili.

Lo scopo di questa tesi è studiare l'influenza della scelta di diversi modelli in silice mesoporosa sulle proprietà morfologiche ed elettrocataliche finali dei catalizzatori ottenuti, nonché valutare l'impatto di variazioni negli approcci di nanocasting su campioni derivati dallo stesso modello di silice.
Sono stati sintetizzati sei catalizzatori, tre da diverse sorgenti di silice e tre con variazioni nelle fasi e nelle condizioni di impregnazione. Tutti i catalizzatori a base di carbonio sono stati prodotti mediante pirolisi ad alta temperatura, seguita da fasi di etching acido e alcalino. Inoltre, nel tentativo di migliorare le proprietà fisiche e catalitiche dei materiali, sono stati sottoposti a un secondo ciclo di pirolisi.
I materiali sintetizzati sono stati caratterizzati utilizzando metodi fisico-chimici, rivelando vari gradi di cristallinità, un'elevata area superficiale specifica e diverse strutture porose a seconda della scelta della silice e delle fasi di impregnazione seguite.
Successivamente, questi campioni sono stati testati per la reazione di riduzione dell'ossigeno (ORR) utilizzando un elettrodo a disco rotante ad anello (RRDE) in soluzioni elettrolitiche sia acide che alcaline.

1.1. CELLE A COMBUSTIBILE A MEMBRANA A SCAMBIO PROTONICO E REAZIONE DI RIDUZIONE DELL'OSSIGENO

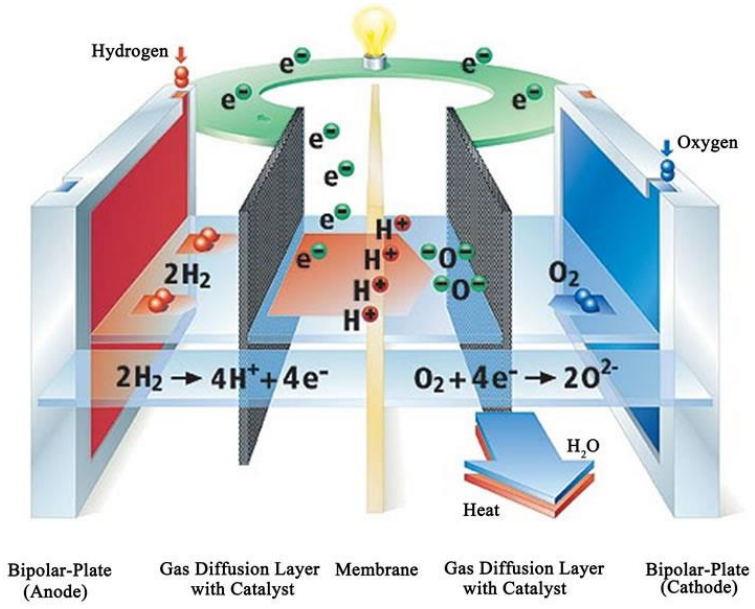

Figura 1. Struttura di una cella a combustibile a scambio protonico.

Le celle a combustibile a membrana a scambio protonico (PEMFC), come rappresentato in figura 1, funzionano attraverso una serie di reazioni elettrochimiche che avvengono all'interfaccia tra gli elettrodi e la membrana elettrolitica.
Un elemento chiave è l'assemblaggio membrana-elettrodo (MEA), costituito dall'elettrocatalizzatore e dalla membrana. Il gas combustibile (solitamente idrogeno) e l'ossidante (aria o ossigeno) vengono forniti alla MEA attraverso una serie di piastre che hanno lo scopo di diffonderli in modo uniforme sulle due facce della membrana. Il materiale più comune per la membrana è Nafion®, un polimero acido solfonico perfluorinato. La membrana è posizionata tra i due elettrodi di carbonio poroso.
L'idrogeno gassoso viene alimentato nel compartimento dell'anodo dove, a contatto con l'elettrodo, subisce la reazione di ossidazione dell'idrogeno (HOR). Simultaneamente, ossigeno o aria vengono forniti al compartimento del catodo, dove ha luogo la reazione di riduzione dell'ossigeno (ORR). Queste due semi-reazioni, separate dalla membrana conduttrice di protoni, si combinano per generare

energia elettrica all'interno della cella a combustibile. Durante il primo stadio si verificano le reazioni elettrochimiche, mentre la membrana consente la conduzione dei protoni prodotti dall'anodo al catodo.

La reazione anodica di ossidazione dell'idrogeno può essere riassunta come segue:

$$H_2 \rightarrow 2H^+ + 2e^- \qquad (1)$$

La reazione catodica di riduzione dell'ossigeno invece consiste di numerosi passaggi intermedi, i quali variano in base alle caratteristiche sia del catalizzatore che dell'elettrolita.
Essa può seguire due percorsi principali:

- Riduzione a quattro elettroni (equazione (2)) con trasferimento di quattro elettroni e di quattro protoni con successiva formazione di H_2O se avviene in ambienti acidi o di OH^- in ambienti alcalini.

- Riduzione a due elettroni (equazioni (3)-(6)) con formazione di H_2O_2 in ambienti acidi o di HO_2^- in ambienti basici.

Se la reazione di riduzione avvenisse secondo l'ultimo percorso con successiva formazione di perossido di idrogeno, questo potrebbe reagire con alcuni ioni metallici lisciviati dal catalizzatore, innescando così delle reazioni di tipo Fenton che produrrebbero radicali altamente reattivi come •OH che possono danneggiare il supporto di carbonio del catalizzatore stesso, riducendone così l'efficienza e la durata.
La riduzione completa dell'ossigeno ad acqua (H_2O) attraverso il percorso a quattro elettroni invece permette di estrarre tutta l'energia immagazzinata nel legame O-O della molecola di ossigeno. Questo si traduce in una maggiore efficienza di conversione dell'energia per la cella a combustibile. Inoltre, evitando la formazione di perossido di idrogeno e le conseguenti reazioni collaterali indesiderate, si riduce il degrado del catalizzatore e se ne aumenta la vita operativa.
Di seguito viene riportato lo schema della reazione di riduzione dell'ossigeno.

$$\mathrm{OH}^- O_2 + 4H^+ + 4e^- \rightarrow 2H_2O \qquad (2)$$

$$O_2 + 2H^+ + 2e^- \rightarrow H_2O_2 \qquad (3)$$

$$H_2O_2 + 2H^+ + 2e^- \rightarrow 2H_2O \qquad (4)$$

$$2H_2O_2 \rightarrow 2H_2O + O_2 \qquad (5)$$

Se la reazione viene avviene in elettroliti alcalini, invece, il prodotto finale sarà OH^- . La reazione può comunque avvenire in modo diretto (equazione (6)) o attraverso un percorso a due step (equazioni (7)-(9)).

$$O_2 + 2H_2O + 4e^- \rightarrow 4OH^- \qquad (6)$$

$$O_2 + 2H_2O + 2e^- \rightarrow 4HO_2^- + OH^- \qquad (7)$$

$$HO_2^- + H_2O + 2e^- \rightarrow 3OH^- \qquad (8)$$

$$HO_2^- \rightarrow 2OH^- + O_2 \qquad (9)$$

I catalizzatori a singolo atomo risultano essere estremamente promettenti per superare le limitazioni dei catalizzatori tradizionali impiegati nelle PEMFC grazie proprio alla loro elevata attività e selettività: la possibilità di avere dei singoli atomi di metallo (in questo caso ferro) ancorati al supporto carbonioso funzionalizzato con azoto (gli atomi di metallo si legano ai diversi gruppi azotati presenti nel materiale di supporto) consente in via teorica di evitare il percorso a 2 elettroni (che generalmente viene seguito a causa della presenza di aggregati di particelle di ferro). Inoltre, l'ampia superfice e la struttura porosa ben definita del carbonio consentono di superare le limitazioni legate al trasporto di massa verso i siti attivi, incrementando dunque la resa e la selettività verso il percorso a quattro elettroni.

2. SINTESI E METODOLOGIE

In questa sezione verranno presentati i diversi metodi utilizzati sia per la sintesi dei vari supporti in silice con diverse strutture e caratteristiche, sia per la sintesi dei catalizzatori Fe-N-C col metodo del supporto sacrificale.

2.1. SINTESI DEI MATERIALI SILICEI MESOPOROSI

In questo lavoro di tesi, quattro tipi di silice mesoporosa sono stati sintetizzati in modo tale da studiare gli effetti della struttura porosa della silice sull'impregnazione e sulle caratteristiche finali dei catalizzatori.
Per raggiungere questo obiettivo sono stati utilizzati tre protocolli differenti relativi alla silice denominata KIT-6 (Korea Advanced Institute of Science and Technology-6), al fine di ottenere tre diverse strutture in termini di porosità e di proprietà: struttura bidimensionale esagonale, struttura mista esagonale 2D/cubica 3D, e struttura cubica 3D con simmetria cubica $Ia\bar{3}d$ tipica del KIT-6.
Infine, è stato impiegato il protocollo classico della silice SBA-15 ((Santa Barbara Amorphous type materials-15) per ottenere la disposizione esagonale 2D dei pori con simmetria *p6mm*.

- Protocollo a: Sintesi della silice a struttura esagonale bidimensionale derivata da KIT-6 (KIT-6-*p6mm*)

Questo materiale è stato sintetizzato seguendo il rapporto molare tra i reagenti proposto da Kleitz et al., ma i quantitativi sono stati proporzionalmente scalati in modo da poter usare un reattore da 200 ml:

TEOS : P123 : HCl : H2O : BuOH = 1 : 0.017 : 1.83 : 195 : 1.31

Quantitativamente parlando, 4.836 g di Pluronic P123 (EO20PO70EO20, MW=5800) sono stati completamente sciolti in 175 g di acqua distillata e 9.516 g di HCl concentrato (37%). A questa miscela sono stati aggiunti 4.84 g di 1-butanolo e il tutto è stato mescolato vigorosamente a 35°C per 1 ora in un contenitore di reazione aperto. Successivamente, sono stati aggiunti 10.408 g di tetraetosisilano (TEOS) e il composto è stato lasciato sotto agitazione per 24 ore alla stessa temperatura.
Per ottenere un materiale con pori esagonali 2D, il contenitore della reazione è stato mantenuto aperto per consentire l'evaporazione simultanea di 1-butanolo e HCl, poiché è l' 1-butanolo che consente di ottenere una mesofase cubica.
Trascorso questo tempo, la miscela è stata trasferita in un reattore chiuso in teflon e trattata termicamente a 100°C per altre 24 ore in un forno statico. È stata poi filtrata a caldo senza lavaggio ed essiccata per una notte alla stessa temperatura. Il Pluronic è stato rimosso per estrazione con solvente utilizzando un pallone con refrigerante a monte per evitare perdite di evaporazione. L'estrazione è avvenuta utilizzando 7.5 ml di HCl (37%) e 500 ml di etanolo a 80°C. Successivamente, il materiale è stato calcinato in una muffola a 550°C per 5 ore.
Il campione finale è stato denominato "KIT-6-*p6mm*".

- Protocollo b: Sintesi della silice con struttura mista esagonale 2D/cubica 3D derivata da KIT-6 (KIT-6-*dual*)

La sintesi di questo materiale è avvenuta seguendo comunque il protocollo di Kleitz -mantenendo le stesse quantità e procedure- tranne per il recipiente di reazione che in questo caso è rimasto sigillato. Se durante la prima sintesi si è vista l'importanza del butanolo, in questa è stato utilizzato il ruolo dell'ambiente acido: il materiale finale, chiamato "KIT-6-*dual*",mostra alcune proprietà peculiari e molto interessanti, che possono essere classificate come a metà strada tra le proprietà strutturali di KIT-6 e SBA-15.

- Protocollo c: Sintesi della silice KIT-6 con struttura cubica 3D e simmetria $Ia\bar{3}d$ (KIT-6)

È stata successivamente sintetizzata una silice KIT-6 con struttura tridimensionale e simmetria cubica $Ia\bar{3}d$ seguendo il protocollo di Tae-Wan Kim et al.
Per ottenere questa cristallinità è emerso che un intervallo di HCl 0,25-0,75 M fornisce rese elevate di silice mesoporosa cubica altamente ordinata, vicine al 100% in base al recupero di silice.
Considerando tutte le possibili variabili e il loro contributo, per la sintesi è stato scelto il seguente rapporto molare dei materiali:

TEOS : P123 : HCl : H2O : BuOH = 1.5 : 0.017 : 1.83 : 195 : 1.7

In termini di quantitativi in peso, sono stati impiegati 6 g di Pluronic P123 (EO20PO70EO20, MW=5800), 144 g di acqua distillata, 7.47 g di HCl (37%), 5.17 di 1-butanolo, e 12.8 g di tetraetosisilano (TEOS). Il procedimento di mixing è lo stesso dei due protocolli elencati in precedenza. Il trattamento termico è avvenuto ad una temperatura di 373 K per 24 ore, seguita da filtraggio a caldo, essiccazione, e calcinazione a 550 °C.
Il materiale finale è stato denominato KIT-6, ed è caratterizzato dalle proprietà tipiche di questo tipo di silice.

- Protocollo d: Sintesi della silice SBA-15 con struttura esagonale 2D (SBA-15)

Per quanto riguarda l'SBA-15, la sintesi è stata sviluppata sulla base del lavoro di Guillet-Nicolas et al.
Gli step per la preparazione di questa silice sono molto simili a quella precedente per KIT-6, tuttavia alcune differenze sono cruciali per ottenere tale materiale.
Più precisamente, sono stati utilizzati una soluzione acquosa di copolimero Pluronic P123, acido cloridrico (HCl, 37,5%), e tetraetossisilano (TEOS) come sorgente di silice. Il rapporto molare della miscela di reazione è:

TEOS : P123 : HCl : H2O = 1 : 0,022 : 0,7 : 130

In termini di peso, 8,0 g di Pluronic P123 sono stati disciolti in 146,25 g di acqua distillata e 4,43 g di HCl (37%) sotto agitazione vigorosa. Dopo la completa dissoluzione, 13,0 g di TEOS sono stati aggiunti in un'unica volta alla soluzione limpida omogenea. Questa miscela è stata ulteriormente lasciata sotto agitazione a T = 35 °C per 24 ore a circa 1000 rpm, trattandosi di una soluzione molto viscosa. Successivamente, la miscela di sintesi è stata posta in un forno a 80 °C per altre 24 ore in

condizioni statiche. In seguito, la miscela è stata essiccata a 140 °C per tutta la notte. Per la rimozione del template di silice, le polveri di silice sintetizzate sono state dapprima brevemente disperse in una miscela di etanolo/HCl a 80 °C - seguendo la stessa procedura descritta per KIT-6 - e successivamente calcinate a 550 °C per 5 ore.
Questo metodo di sintesi offre alcuni vantaggi rispetto ad altre procedure riportate per la preparazione di SBA-15, in quanto queste condizioni consentono un'eccellente riproducibilità, un ordine strutturale molto elevato, la purezza della mesofase e un facile scale-up.
Il composto finale è una silice SBA-15 mesoporosa altamente ordinato, denominata SBA-15.

2.2. SINTESI DEI CATALIZZATORI

La sintesi degli elettrocatalizzatori utilizza diverse tecniche che condividono alcuni principi comuni. Questi principi includono la miscelazione iniziale dei materiali precursori, seguita da un trattamento ad alta temperatura (pirolisi) e da un successivo passaggio di pulizia (lavaggio acido).
Come fonte di carbonio, sono particolarmente ricercati composti con un alto rapporto atomico azoto/carbonio (N:C). Esempi sono la nicarbazina, la 1,10-fenantrolina, ecc. Questi materiali facilitano l'incorporazione di un'alta densità di siti attivi nella struttura finale dell'elettrocatalizzatore grazie all'abbondanza di atomi di azoto.
La pirolisi gioca un ruolo cruciale nel modellare la struttura finale dell'elettrocatalizzatore. Durante questo processo, temperature elevate (tipicamente 700-1100 °C) forniscono l'energia necessaria per riorganizzare e formare nuovi legami chimici all'interno della miscela precursore. Questa decomposizione termochimica avviene in assenza di ossigeno (condizioni anossiche). Controllando attentamente variabili come la velocità di riscaldamento, la temperatura finale e la composizione del gas utilizzata durante la pirolisi, è possibile mettere a punto le caratteristiche finali dell'elettrocatalizzatore. Gli studi hanno dimostrato che una velocità di rampa più lenta (circa 5-10 °C/min) può massimizzare il volume dei pori all'interno del materiale. La selezione della temperatura finale ottimale è fondamentale per prevenire l'agglomerazione indesiderata delle particelle metalliche e la grafitizzazione eccessiva.
Dopo la pirolisi, viene spesso impiegato un passaggio di lavaggio acido ed uno basico. Questi trattamenti rimuovono rispettivamente i composti contenenti metalli (come nanoparticelle di metallo o ossido di metallo) debolmente legati all'intelaiatura di carbonio e considerati elettrochimicamente indesiderabili, ed eventuali tracce di silice rimasta all’interno della struttura porosa. Questi materiali indesiderati contribuiscono alla massa senza aumentare l'attività, e vengono generalmente eliminati utilizzando rispettivamente soluzioni di acido cloridrico (HCl) o acido solforico (H_2SO_4) e di idrossido di sodio (NaOH).
Uno schema rappresentativo per questi processi di sintesi è raffigurato in figura 2.

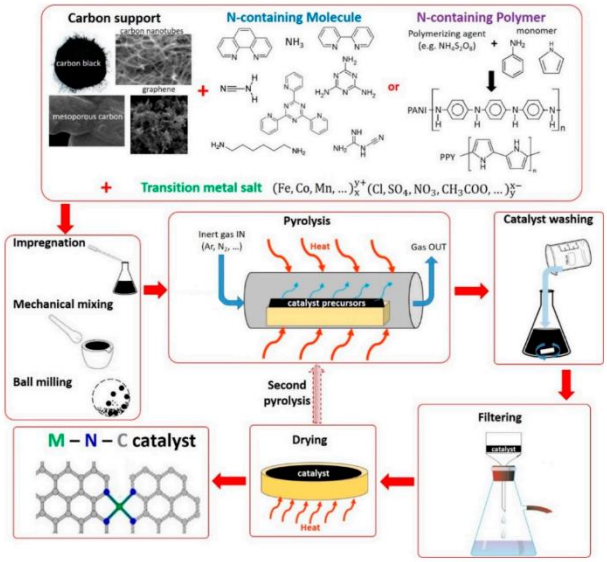

Figura 2. Schema rappresentante il processo di sintesi attraverso il metodo di nanocasting dei catalizzatori M-N-C.

In questa tesi, la sintesi è stata effettuata secondo il lavoro di Yu Xiong et al. utilizzando 1,10-fenantrolina come fonte di C/N, e di Ferro(III) nitrato nonaidrato ($Fe(NO_3)_3 \cdot 9H_2O$) come precursore metallico.
Sono stati realizzati sei catalizzatori con approcci diversi, in quanto lo scopo ultimo di questa tesi è lo studio dell'influenza del supporto in silice utilizzata durante la sintesi sul catalizzatore finale in termini di struttura e di attività catalitica, lo studio dell'influenza del metodo di nanocasting sui campioni ottenuti a partire rispettivamente dalle tre silici KIT-6 con struttura diversa, e dalle silici SBA-15.

- Protocollo 1: studio dell'influenza della scelta del supporto in silice sulla struttura del supporto carbonioso (sintesi dei catalizzatori 1a_Fe@N-CMK-8, 1b_Fe-N@CMK-3/8, e 1d_Fe-N@CMK-3)

Per la prima sintesi, 404 mg di $Fe(NO_3)_3 \cdot 9H_2O$ sono stati disciolti in 10 ml di soluzione acqua/etanolo (v:v=1:1) attraverso l'utilizzo di un sonicatore. La miscela è stata successivamente aggiunta in un'altra soluzione acqua/etanolo (v:v=1:1) contenente 500 mg di KIT-6-*p6mm* (protocollo a) e 540.6 mg di 1,10-fenantrolina precedentemente messe a miscelare, portato a 80 °C e tenuto sotto mixing per 24 ore in modo da lasciare evaporare il solvente.
Successivamente, il composto arancione ottenuto è stato finemente pestato in un mortaio e trasferito nel reattore di pirolisi, lasciato venti minuti sotto flusso di azoto per rimuovere ogni altro tipo di gas presente e successivamente pirolizzato a 900 °C per 3 ore, con una velocità di riscaldamento di 5°C/min.
Il campione ottenuto, etichettato come 1a_Fe-N@CMK-8, è stato quindi trattato con una soluzione acquosa di NaOH 6M (15 ml) sotto agitazione vigorosa a 60 °C per 24 ore, per rimuovere il supporto in silice.
La miscela è stata poi filtrata, lavata fino a pH neutro, e successivamente essiccata in forno per tutta la notte a 100 °C.
Per quanto riguarda le possibili nanoparticelle di Fe e/o ossido di ferro, queste sono state rimosse mediante etching acido con 50 ml di HCl (37%) per 3 ore a temperatura ambiente, dopodiché il campione è stato nuovamente filtrato e asciugato.

Lo stesso protocollo è stato seguito utilizzando come supporti in silice KIT-6-*dual* e SBA-15, producendo rispettivamente i campioni chiamati 1b_Fe-N@CMK-3/8 e 1d_Fe-N@CMK-3.

- Protocollo 2: studio dell'influenza della procedura di nanocasting usando i supporti in silice KIT_6: sintesi del materiale 1c_Fe-N@CMK-8

In questo protocollo, il processo di nanocasting è stato modificato per cercare di migliorare la diffusione delle fonti di carbonio nei canali dei pori della silice.
Come sorgente di silice è stato utilizzato KIT-6 proveniente dal protocollo c (con fase cubica $Ia\bar{3}d$).
Il materiale carbonioso derivato, etichettato come 1c_Fe-N@CMK-8, sarà confrontato con il campione 1a_Fe-N@CMK-8 e 1b_Fe-N@CMK-3/8 per osservare e confrontare le differenze in termini di struttura, quantità di ferro coordinato e attività catalitica.
Questo processo prevede due impregnazioni consecutive e comprende trattamenti termici in muffola:

1. **Prima impregnazione:** 500 mg di KIT-6 sono stati miscelati con 414 mg di 1,10-fenantrolina in una soluzione di 3 ml di acqua/etanolo (v:v = 1:1). Mentre le due polveri venivano miscelate finemente insieme, 187,5 mg di $Fe(NO_3)_3 \cdot 9H_2O$ venivano disciolti con un sonicatore in una soluzione 2 ml di acqua/etanolo (v:v = 1:1).

   La miscela è stata lasciata sotto agitazione vigorosa per 1 ora a temperatura ambiente, dopodiché la sospensione così preparata è stata sottoposta a un processo di trattamento termico in tre fasi all'interno di una muffola in presenza di aria. Il profilo di temperatura prevedeva un mantenimento iniziale a 100 °C per 6 ore, seguito da un successivo aumento a 140 °C mantenuto per 2 ore e un ultimo step a 160 °C per 6 ore.

2. **Seconda impregnazione:** La procedura appena descritta è stata ripetuta per la seconda impregnazione, con una riduzione delle quantità iniziali dei reagenti impiegati: la polvere trattata termicamente è stata miscelata con 250 mg di 1,10-fenantrolina in una soluzione 2 ml acqua/etanolo (v:v= 1:1), alla quale sono stati successivamente aggiunti 95 mg di $Fe(NO_3)_3 \cdot 9H_2O$ disciolta. Il tutto è stato miscelato per 1 ora, e nuovamente messo in muffola a 100 °C per 6 ore e a 140 °C per 2 ore.

Le condizioni di pirolisi sono state mantenute come in precedenza, raggiungendo i 900 °C con una velocità di riscaldamento di 5 °C/min e mantenendo questa temperatura per 3 ore. Una volta raffreddata, la miscela è stata trattata con NaOH e HCl utilizzando le stesse quantità e temperature di prima.

- Protocollo 3: studio dell'influenza della procedura di nanocasting usando i supporti in silice SBA-15: sintesi dei materiali 2d_Fe-N@CMK-3 e 3d_Fe-N@CMK-3

Sono stati sintetizzati altri due catalizzatori a partire dalla silice SBA-15 del protocollo d, modificando leggermente alcune condizioni.
Per quanto riguarda la prima sintesi, le quantità delle due impregnazioni sono le stesse del protocollo 2 ma, dopo una fase iniziale di agitazione di 1 ora a temperatura ambiente, il trattamento termico è

stato effettuato in atmosfera inerte (nel reattore di pirolisi sotto flusso costante di N2). I profili di temperatura e i tempi sono stati i seguenti: 6 ore a 100 °C, 2 ore a 140 °C e 6 ore a 160 °C.
Una volta raffreddato a temperatura ambiente, il campione è stato pirolizzato a 900 °C per 3 ore. In questo modo si è potuto evitare una possibile ossidazione del carbonio durante i processi di impregnazione termica.
Dopo i processi di etching per rimuovere lo stampo di silice e le nanoparticelle di Fe, si è ottenuto il campione etichettato come "2d_Fe-N@CMK-3".
La seconda sintesi è avvenuta in modo simile, utilizzando le stesse quantità e precursori descritti, ad eccezione che i reagenti sono stati miscelati a temperatura ambiente all'interno di un reattore chiuso di Teflon. Successivamente, il reattore sigillato è stato posizionato nella muffola per il trattamento termico e riscaldato a 100 °C per 6 ore e successivamente a 160 °C per altre 6 ore.
In questo modo, a causa dell'aumento della pressione interna, si suppone che una maggiore quantità delle sorgenti del materiale desiderato venga forzata a entrare nella rete di pori della silice, come inizialmente confermato dal peso maggiore del catalizzatore rimasto dopo le fasi di pirolisi ed etching. Questo può essere collegato a una minore quantità di Fe/C che potrebbe essersi coordinata all'esterno della rete di pori della silice; di conseguenza, è stato rimosso meno materiale durante le fasi di pirolisi e pulizia.
Il catalizzatore prodotto è etichettato come "3d_Fe-N@CMK-3".

3. CARATTERIZZAZIONE DEI MATERIALI

Una caratterizzazione fisico-chimica completa dei materiali sintetizzati è stata condotta utilizzando tecniche analitiche che includono la diffrazione a raggi X (XRD), la microscopia elettronica a scansione e a trasmissione (STEM) accoppiata alla spettroscopia a raggi X ad energia dispersiva (EDS), e l'assorbimento di azoto a 77 K combinata con il modello per superficie specifica secondo Brunauer-Emmett-Teller (BET) e di Barrett-Joyner-Halenda (BJH).

Sono state inoltre misurate le prestazioni elettrocataliche dei catalizzatori per la reazione di riduzione dell'ossigeno (ORR), valutate utilizzando un elettrodo a disco rotante ad anello (RRDE) in un sistema a tre elettrodi, con elettroliti sia acidi che alcalini saturati di ossigeno.
Le curve di polarizzazione sono state ottenute all'interno della finestra di potenziale tipica per l'ORR, mostrando la densità di corrente in funzione del potenziale applicato all'elettrodo di lavoro.

3.1. CARATTERIZZAZIONE DEI SUPPORTI IN SILICA

Per comprendere le proprietà dei catalizzatori oggetto di studio, questa sottosezione analizzerà i dati provenienti dalla caratterizzazione dei template sacrificabili in silice da cui derivano i campioni SAC. In figura 3 sono stati presentati i grafici ottenuti dall'analisi XRD di tutti i materiali silicei in esame.

Come già suggerito dal nome stesso, il campione denominato KIT-6-*p6mm* (dal protocollo a) mostra un diagramma di diffrazione molto simile a quello del campione SBA-15. Questa somiglianza deriva dal fatto che, seguendo il protocollo di Freddy Kleitz, durante la fase iniziale di agitazione, il recipiente di reazione è rimasto aperto per 24 ore, consentendo l'evaporazione simultanea di butanolo e acido cloridrico. Questo processo è fondamentale per ottenere una disposizione dei pori esagonale 2D.
Nonostante derivi da un protocollo KIT-6 e manchi di una struttura porosa 3D, il materiale finale presenta una disposizione ben organizzata di pori 2D con simmetria *p6mm*. I picchi principali osservati a $2\theta \approx 0{,}96°$, 1,60° e 1,90° sono infatti tipici della silice mesoporosa con un network poroso esagonale 2D, corrispondenti rispettivamente ai piani di diffrazione [100], [110] e [200].

D'altro canto, si può affermare che solo il grafico verde del materiale KIT-6 mostra i due picchi principali caratteristici di questa specifica silice per un angolo di incidenza $2\theta \approx 1{,}00°$, 1,15° relativi ai piani [211] e [220], e coerenti con il modello previsto per la silice mesoporosa KIT-6 con simmetria cubica $Ia\bar{3}d$.

Infine, il grafico intermedio del KIT-6-*dual* presenta somiglianze sia con i materiali strutturati 3D che con quelli strutturati 2D, dimostrando la sua struttura duale come infatti dimostrato dalle immagini STEM. Ciò è stato possibile grazie all'utilizzo di condizioni più acide durante la sintesi. Più precisamente, sono stati aggiunti 0,2 g (o 0,17 ml) di HCl in più rispetto alla procedura standard, poiché un ambiente più acido consente la formazione di pori esagonali 2D.

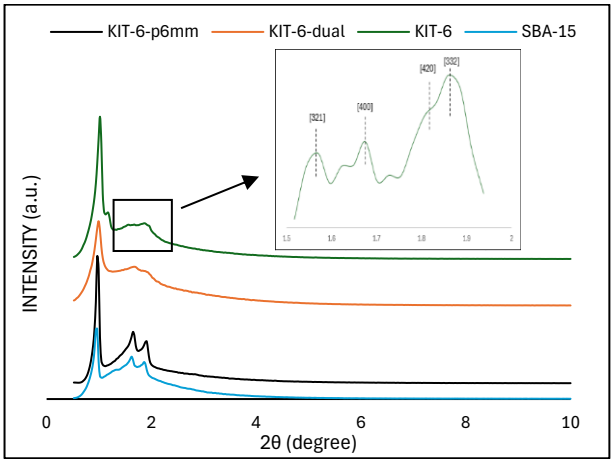

Figura 3. Grafici PXRD dei template KIT-6s ed SBA-15.

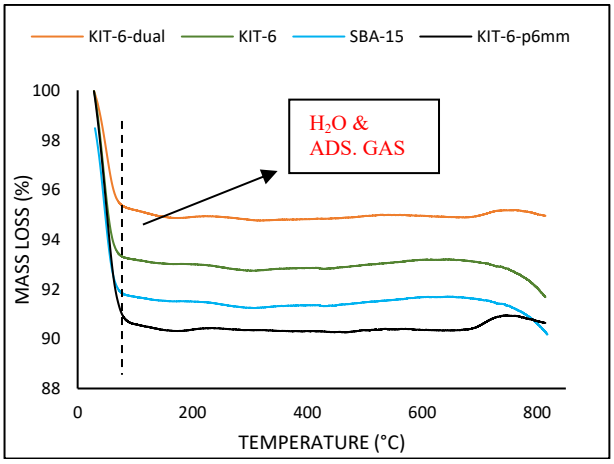

Figura 4. Risultati dell'analisi termogravimetrica sui template KIT-6 ed SBA-15.

La Figura 4 mostra la stabilità termica dei campioni derivati dalla silice.
L'analisi TGA (Analisi Termogravimetrica) mostra un picco di perdita di peso a circa 100 ºC attribuibile al desorbimento di acqua e di eventuali gas adsorbiti. L'assenza di altre perdite di peso indica che il tensioattivo è stato rimosso in modo efficiente attraverso la combinazione del metodo di estrazione con solvente e la calcinazione a 550 ºC.

Le isoterme di adsorbimento-desorbimento di N2 a 77 K sono state raccolte per ottenere le proprietà testuali dei campioni di silice e i risultati sono riassunti nella figura 5 e nella Tabella 1.
La Figura 5 (a) mostra che le silici sintetizzate presentano un'isoterma di tipo IV con un ciclo di isteresi H1, classificata secondo gli standard IUPAC, caratteristica dei materiali mesoporosi come discusso in precedenza (Capitolo 2).
Tuttavia, il campione KIT-6 con struttura cubica a simmetria $Ia\bar{3}d$ ricorda anche un'isoterma di tipo II a causa dell'aumento dell'adsorbimento senza limite quando p/p0 = 1. Questo può essere correlato alla presenza di alcune fasi non porose o macroporose nella struttura.

Tabella 1. Proprietà strutturali dei campioni in silice.

	KIT-6-*p6mm*	KIT-6-dual	KIT-6	SBA-15
STRUTTURA DEI PORI	ESAGONALE (*p6mm*)	ESAGONALE/ CUBICA	CUBICA ($Ia\bar{3}d$)	ESAGONALE (*p6mm*)
S_{BET} (m^2/g)	554	555	833	734
V_p (cc/g)	0.6	0.4	2.84	0.76
D_p (nm)	7.4	7.4	5.78	8.1

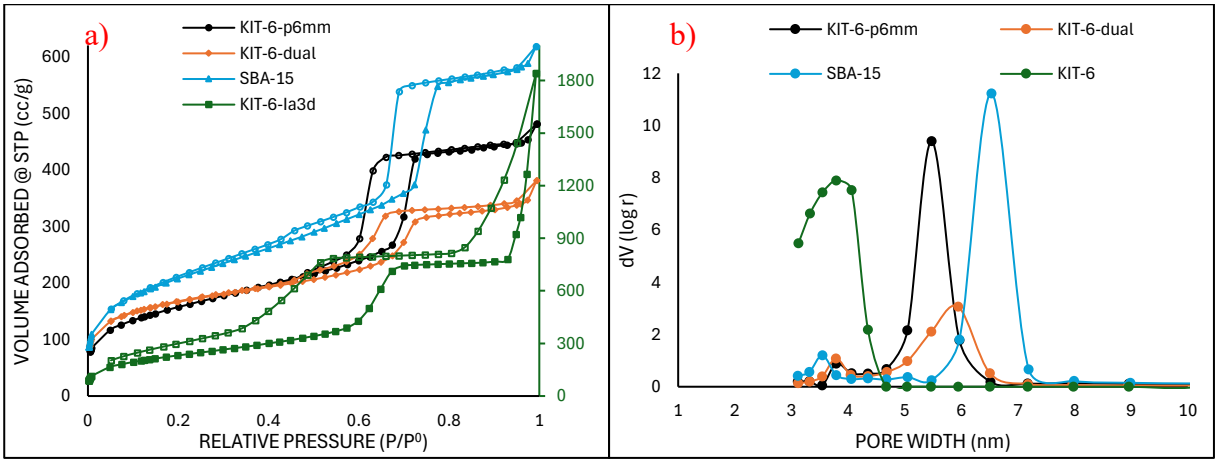

Figura 5. (a) Isoterme di adsorbimento-desorbimento di azoto a 77 K dei campioni in silice. I simboli pieni corrispondono al ramo di adsorbimento, mentre quelli vuoti corrispondono al desorbimento. (b) Curve di distribuzione delle dimensioni dei pori calcolate dal ramo di desorbimento.

Applicando le teorie BET e BJH alle isoterme di adsorbimento/desorbimento di N_2, è possibile determinare la superficie specifica (SBET), il volume dei pori (Vp) (Tabella 1) e le curve di distribuzione delle dimensioni dei pori (Figura 22 (b)).
La distribuzione delle dimensioni dei pori indica che la maggior parte delle silici sintetizzate presenta una distribuzione ristretta delle dimensioni dei pori, ad eccezione del campione KIT-6. I diametri dei pori rientrano nell'intervallo mesoporoso, compresi tra 5,8 e 8,1 nm. Tuttavia, nonostante queste caratteristiche favorevoli, i primi due campioni KIT-6 possiedono un'area superficiale relativamente bassa, pari a circa 555 m^2/g rispetto ai materiali mesoporosi in generale. Al contrario, il campione KIT-6 presenta la più alta area superficiale, superando persino quella del campione SBA-15. Inoltre, esso mostra un volume dei pori notevolmente alto, quasi il doppio di quello riportato in letteratura. Questo valore richiede una doppia conferma.

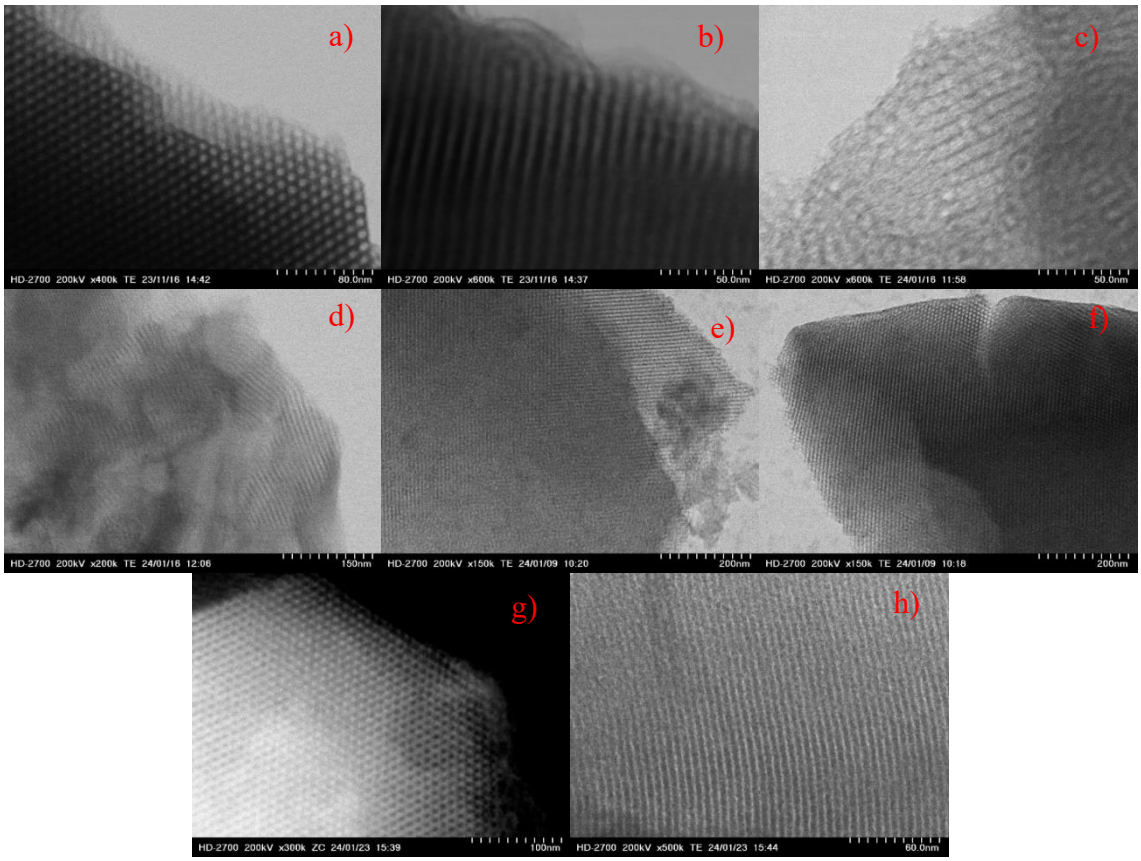

Figura 6. (a), (b) immagini TEM di KIT-6-*p6mm.* (c), (d) immagini TEM di KIT-6-*dual*. (e), (f) immagini TEM di KIT-6. (g), (h) immagini TEM e ZC di SBA-15.

Le immagini di microscopia elettronica a trasmissione (TEM) dei materiali sono presentate in figura 6.

In primo luogo, le figure 6 (a), (b) e (c) offrono ulteriori prove a sostegno della formazione di una rete di pori esagonale nella silice KIT-6-*p6mm*, e la stessa organizzazione dei pori è visibile nel campione SBA-15 in figura 6 (g) ed (h), pur mostrando differenze nelle proprietà strutturali che suggeriscono essere diversa dalla silice SBA-15.

La figura 6 (c) relativa al campione KIT-6-*dual* invece mostra la presenza di pori cubici e, allo stesso tempo, anche un'organizzazione porosa esagonale come indicato in figura 6 (d).

Le immagini 6 (e), (f) del campione KIT-6 invece mostrano una struttura cubica perfetta, con simmetria $Ia\bar{3}d$ tipica di questa tipa di silice.

3.2 CARATTERIZZAZIONE DEI CATALIZZATORI

Nei paragrafi seguenti verrà presentata una descrizione dettagliata delle proprietà morfologiche e strutturali di tutti i catalizzatori, evidenziando le molteplici influenze sia delle sorgenti di silice che delle differenze nella procedura di nanocasting sui campioni finali.

3.2.1. STUDIO DELL'INFLUENZA DELLA MORFOLOGIA DEL TEMPLATE IN SILICE

In figura 7 vengono mostrati i grafici XRD dei catalizzatori 1a_Fe-N@CMK-8, 1b_Fe-N@CMK-3/8 e 1d_Fe-N@CMK-3 derivati rispettivamente dai template rigidi di silice KIT-6-*p6mm*, KIT-6-*dual* e SBA-15. I catalizzatori sono stati ottenuti utilizzando gli stessi metodi di impregnazione e pirolisi, seguendo il protocollo 1 (per maggiori dettagli vedere Capitolo 2).

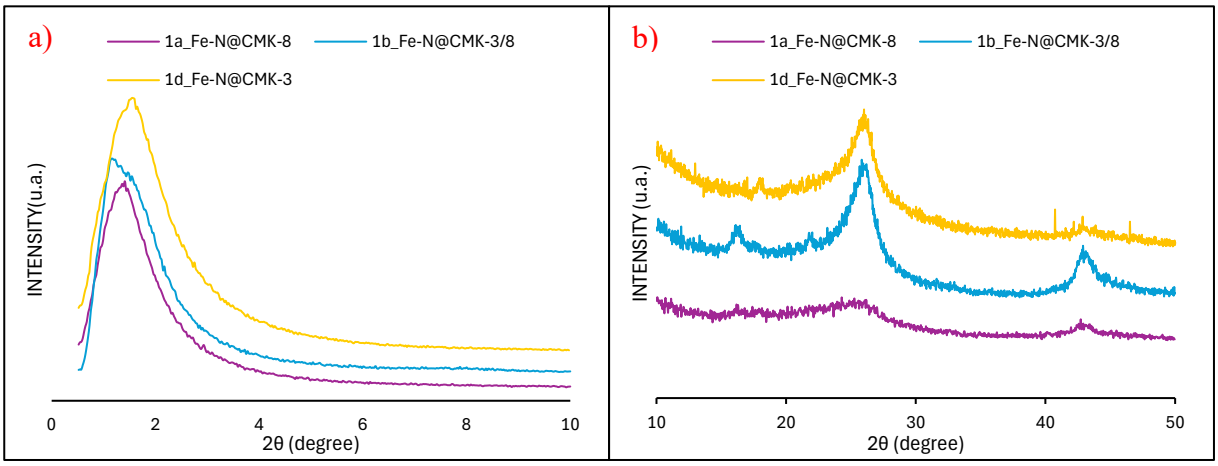

Figure 7. (a) XRD a bassi angoli di incidenza di 1a_Fe-CMK-8, 1b_Fe-N@CMK-3/8, e 1d_Fe-CMK-3. (b) XRD ad alti angoli di incidenza di 1a_Fe-CMK-8, 1b_Fe-N@CMK-3/8, e 1d_Fe-CMK-3.

I grafici di diffrazione XRD a basso angolo (Figura 7a) di tutti i compositi a base di carbonio provenienti da KIT-6 e SBA-15 hanno mostrato un'intensità complessiva molto inferiore rispetto ai corrispondenti template di silice.
Un primo picco largo è presente in tutti i campioni sintetizzati, a circa $2\theta \approx 1{,}5°$, probabilmente originato dalla diffrazione dei raggi X da un certo grado di periodicità dei canali mesoporosi, correlato ai piani di diffrazione [100]. L'assenza dei due modelli di diffrazione aggiuntivi corrispondenti ai piani [110] e [200] può essere attribuita a un potenziale disordine dei pori, probabilmente dovuto alla mancata formazione di disposizioni cubiche ed esagonali dei pori durante il processo di nanocasting. Ad angoli di diffrazione più alti (Figura 24 b) si possono osservare due picchi acuti a circa $2\theta \approx 25°$ e 43°, attribuibili al carbonio grafitizzato, e corrispondenti rispettivamente ai suoi piani di diffrazione [002] e [101]. Questa riorganizzazione del carbonio è più evidente nel campione 1b_Fe-N@CMK-3/8, come confermato dalle immagini TEM nella Figura 13 (a) e (b).
D'altra parte, è evidente che il 1a_Fe-N@CMK-8 sintetizzato da KIT-6-*p6mm* presenta la struttura meno grafitizzata, poiché i suoi picchi sono appena osservabili.

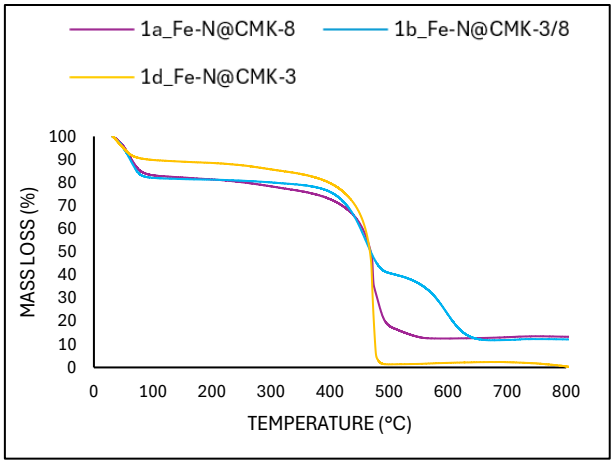

Figura 8. Curve dall'analisi TG sui catalizzatori derivanti dai carboni CMK-3 and CMK-8.

La stabilità termica dei catalizzatori e la loro composizione approssimativa, ottenute mediante analisi TGA, sono state presentate nella Figura 8.
Un'analisi iniziale dei risultati TGA rivela una tendenza coerente per tutti i materiali, suggerendo un meccanismo di degradazione condiviso nonostante i diversi template rigidi utilizzati. Questo suggerisce una similitudine in termini di strutture e componenti presenti, i quali si decompongono a temperature simili.

Dopo una perdita di massa iniziale compresa tra il 10% e il 20% in massa attribuita all'evaporazione di umidità e gas adsorbiti, nell'intervallo di temperatura di 400-650 °C -finestra che tipicamente coincide con la degradazione di specie carboniose e azotate- il campione 1a_Fe-N@CMK-8 mostra una perdita in peso di circa il 65%, lasciando quasi il 13% di materiale non degradato fino a 800 °C. Questo suggerisce che una quantità considerevole di nanoparticelle di Fe e silice residua del template è ancora presente nella struttura porosa, nonostante le due fasi di etching sia acido che alcalino.
D'altra parte, il campione 1d_Fe-N@CMK-3 mostra il più alto tasso di degradazione all'interno di questa finestra di temperatura, pari a quasi l'83% in peso, segnale che meno del 2% di questo campione è costituito da nanoparticelle di Fe o silice residua.
Ciò indica che la silice SBA-15 ha permesso una migliore diffusione dei precursori -grazie al suo diametro dei pori più grande e di una struttura più accessibile rispetto ai pori dei KIT-6- che dunque ha consentito anche una penetrazione più facile di NaOH/HCl durante i processi di etching, portando infine ad una rimozione più efficiente di Si e Fe.

Il campione 1b_Fe-N@CMK-3/8 è l'unico che presenta un grafico di degradazione a tre stadi: dopo la perdita di massa iniziale del 18% relativa all'umidità/gas adsorbiti, esso mostra una perdita del 38% tra 400 °C e 500 °C seguita da un ulteriore perdita del 27% nell'intervallo 550-650 °C, lasciando il 12% di materiale non degradato.
Altre analisi sono necessarie per comprendere al meglio le ragioni dietro queste osservazioni, ad esempio tramite *operando* TG-IR in modo da poter studiare l'evoluzione dei gas rilasciati durante la degradazione.

Per quanto riguarda le proprietà strutturali, nella tabella 2 mostrata di seguito e nelle figure 9 (a) e (b) sono presentati rispettivamente i valori numerici, le isoterme di adsorbimento-desorbimento di N_2 a 77 K, e le curve di distribuzione delle dimensioni dei pori calcolate con il metodo di Barrett-Joyner-Halenda (BJH).

Rispetto ai rispettivi template rigidi, i catalizzatori mostrano un volume di adsorbimento leggermente inferiore. Tuttavia, l'analisi della porosità rivela la presenza di strutture porose all'interno dei compositi. In particolare, la dimensione dei pori è rimasta costante in tutti i campioni, variando da 3,1 a 7 nm, e mostrando un picco nella distribuzione della dimensione dei pori comune ai tre catalizzatori (figura 9 b), indice che la maggior parte hanno dimensione uniforme nel range mesoporoso. Inoltre, è anche possibile notare una distribuzione di dimensioni non uniforme, presente dai 9 nm in su, indice della presenza di mesopori di dimensioni diverse.

Tabella 2. Proprietà strutturali dei catalizzatori sintetizzati tramite il protocollo 1.

	1b_Fe-CMK-3/8	1c_Fe-N@CMK-8	1d_Fe-N@CMK-3
S_{BET} (m^2/g)	695	488	625
V_p (cc/g)	0.45	0.20	0.36
D_p (nm)	3.78	3.79	3.77

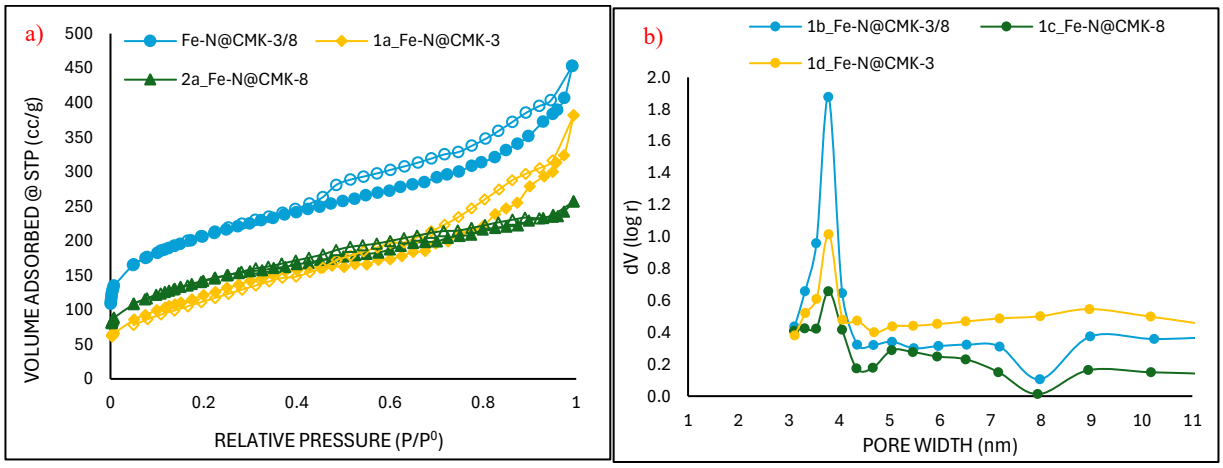

Figura 9. (a) Isoterme di adsorbimento-desorbimento di azoto a 77 K dei catalizzatori Fe-CMK. I simboli pieni corrispondono al ramo di adsorbimento, mentre quelli vuoti corrispondono al desorbimento. (b) Curve di distribuzione delle dimensioni dei pori dal metodo BJH calcolate dal ramo di desorbimento.

Dalle isoterme di adsorbimento/desorbimento di N2 in figura 9 (a) si può osservare che, a differenza delle silici di tipo IV, le isoterme ottenute per le repliche di carbonio provenienti dai tre diversi template di silice si collocano tra il tipo I(b) – per valori di pressione parziale più bassi - e il tipo II. Inoltre, essi mostrano la presenza di un ciclo di isteresi H4, che si verifica quando la regione iniziale di riempimento reversibile dei pori è seguita da un adsorbimento multistrato e condensazione capillare. (32)
Questa descrizione è coerente con quanto osservato dalla distribuzione delle dimensioni dei pori, poiché le isoterme di tipo I(b) si riscontrano in materiali con distribuzioni di dimensioni dei pori su

una gamma più ampia, mentre l'isoterma di tipo II, dalla classificazione IUPAC (27), è direttamente correlata all'adsorbimento di materiali non porosi - confermato dalle immagini STEM riportate in precedenza che mostrano un alto grado di grafitizzazione e amorfismo - dove questa forma è il risultato di un adsorbimento non limitato monostrato-multistrato a valori alti di P/P^0.
Inoltre, dalla classificazione teorica si può anche dedurre che il punto di flesso è meno distintivo (dunque una curvatura più graduale), indice di una sovrapposizione significativa della copertura monomolecolare e l'inizio dell'adsorbimento multistrato.

3.2.2. STUDIO DELL'INFLUENZA DEL'APPROCCIO DI NANOCASTING PARTENDO DAI TEMPLATE KIT-6

Dopo una prima analisi sull'impatto della scelta dei diversi template di silice, in questo paragrafo viene studiato l'effetto dei diversi processi di nanocasting utilizzando i template KIT-6 e simili, ovvero i catalizzatori sintetizzati dai protocolli 1 e 2 descritti nella sezione 2.2.
In figura 10 vengono presentati i grafici dell'analisi XRD, e in figura 11 quelli relativi alla TGA, mentre in figura 12,13, e 14 vengono riportate alcune delle immagini al microscopio STEM.

Dalla figura 10 risulta come tutti i campioni presentino due picchi a valori di 2θ intorno a 26° e 43°, corrispondenti alla diffrazione dei piani grafitici [002] e [101], suggerendo la prevalenza amorfa e con un certo grado di grafitizzazione, come già discusso nel paragrafo precedente.
Tuttavia, i nanotubi di carbonio (CNT) seppur presenti nel campione 1b_Fe-N@CMK-3/8 come visibili nella figura 12 (c) non sono facilmente rilevabili attraverso questa analisi, poiché il grafico di diffrazione XRD dei CNT mostra delle sovrapposizioni con quello della grafite a causa delle loro proprietà intrinseche simili al grafene.
Inoltre, si può notare che il picco che appare a 16° è comune a tutti i campioni, così come un altro più piccolo a 2θ≈ 21°, correlati alla diffrazione di SiO_2, ulteriore conferma che, pur cambiando i processi di impregnazione, i materiali finali mostrano delle somiglianze dovute al diametro dei pori intrinsecamente più piccolo e alla rete porosa complessa dei materiali derivati da KIT-6. Ciò potrebbe aver reso più difficile la penetrazione della soluzione di etching in tutte le regioni interne della silice rendendo difficile la sua completa rimozione.

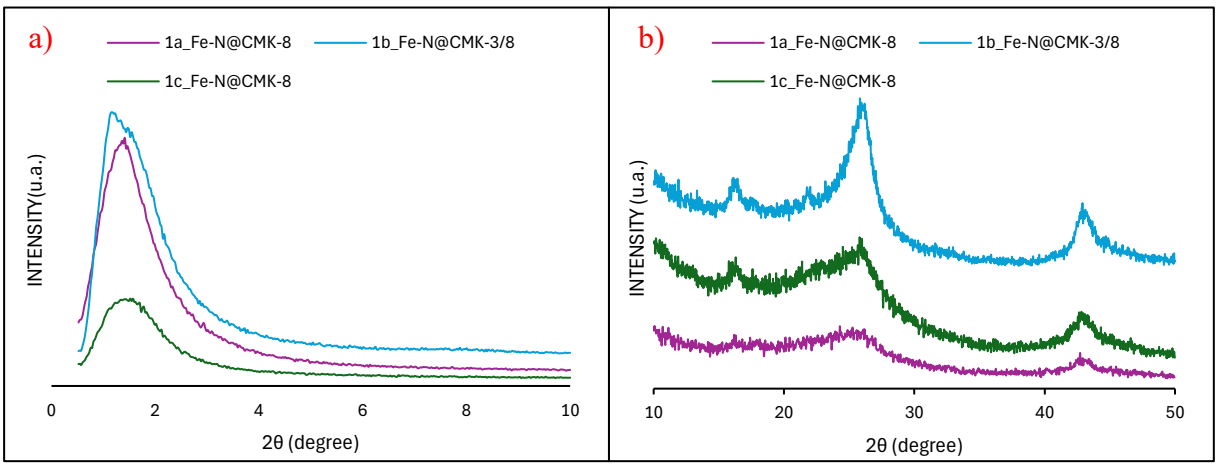

Figura 10. (a) XRD a bassi angoli di incidenza di 1a_Fe-CMK-8, 1b_Fe-N@CMK-3/8, e 1c_Fe-CMK-8. (b) XRD ad alti angoli di incidenza di 1a_Fe-CMK-8, 1b_Fe-N@CMK-3/8, e 1c_Fe-CMK-8.

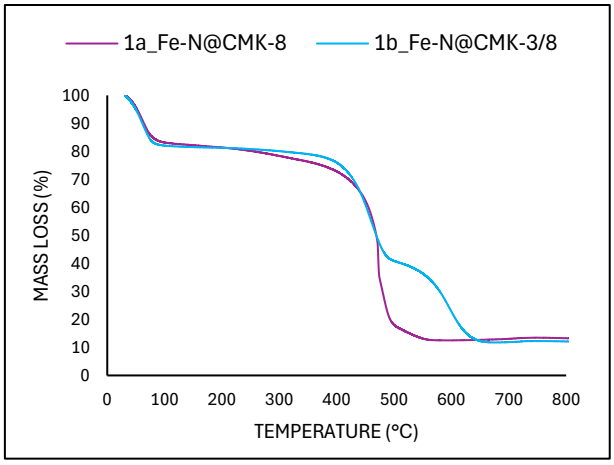

Figura 11. Risultati dell'analisi TG dei campioni 1a_Fe-N@CMK-8 e 1b_Fe-N@CMK-3/8.

Dall'analisi termogravimetrica in figura 11 risulta che i materiali mostrano lo stesso processo di degradazione, così come la stessa percentuale in massa residua di circa il 12% in peso a temperature maggiori di 800 °C relativa alla presenza di silice e di nanoparticelle di ferro.

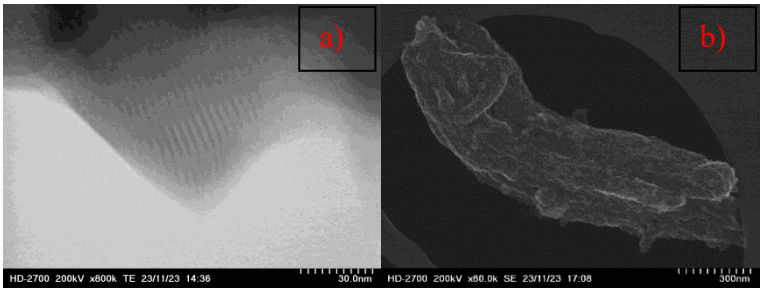

Figura 12. (a),(b) Immagini STEM del catalizzatore 1a_Fe-N@CMK-8 da KIT-6-*p6mm*.

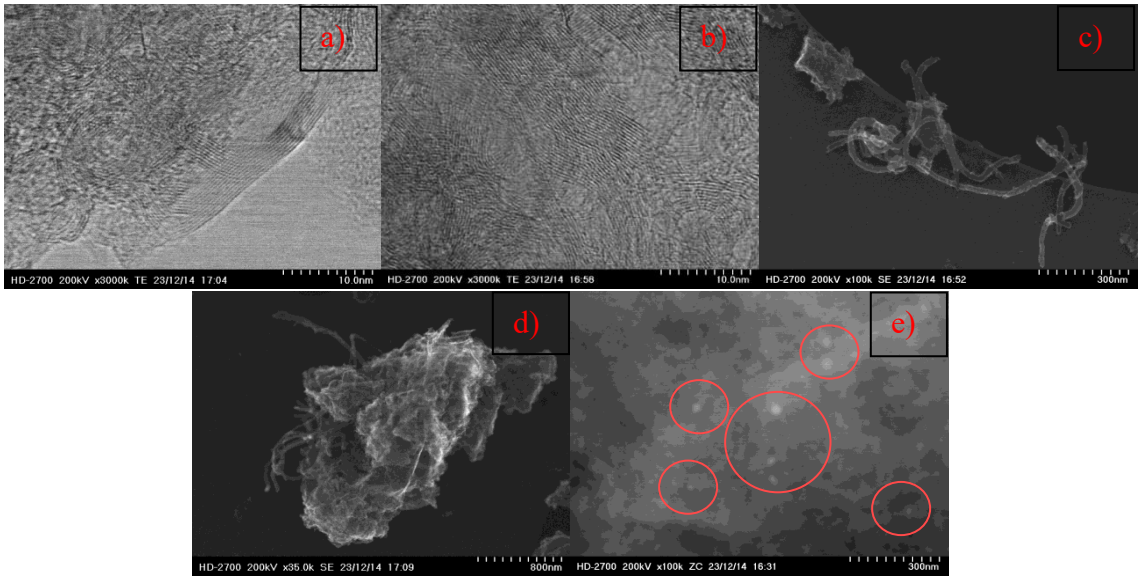

Figure 13. (a),(b),(c),(d),(e) Immagini STEM e ZC di 1b_Fe-N@CMK-3/8 da kit-6-*dual*.

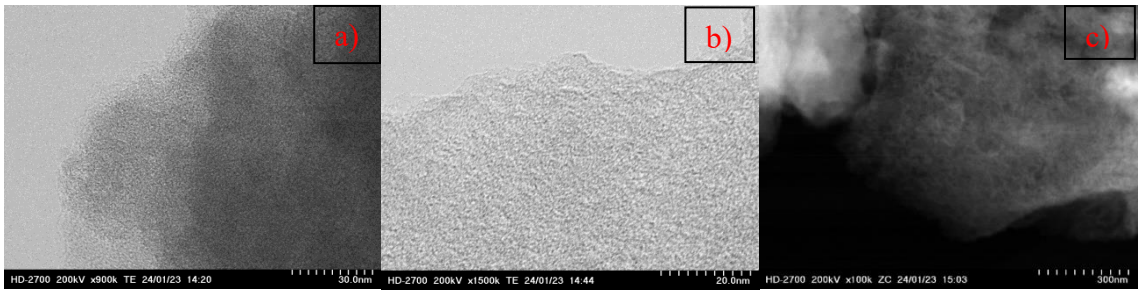

Figure 14. (a),(b),(c) Immagini TEM and ZC di 1c_Fe-N@CMK-8 da KIT-6, protocollo 2.

Le immagini STEM rivelano che il campione 1a_Fe-N@CMK-8 (figura 12 (b)) è l'unico che ha conservato la forma macroscopica a bastoncino del template originale, mentre in figura 12 (a) è ancora visibile la struttura mesoporosa esagonale. Ciò indica che questo catalizzatore ha mantenuto molto bene sia la struttura a livello macroscopico e mesoscopico.
Il campione 1b_Fe-N@CMK-3/8 mostra una struttura macroscopica amorfa (figura 13 (d)). Tuttavia, è il campione più interessante - da un punto di vista morfologico – in quanto mostra diversi tipi di strutture, compresi dei nanotubi di carbonio nella macrostruttura (figura 13 (c)), insieme alla grafite (figura 13 (b)).
Nonostante l'organizzazione ordinata del carbonio, alcune nanoparticelle di ferro sono ancora presenti anche dopo le fasi di etching acido come evidenziato dalla figura 13 (e) dai punti più luminosi cerchiati in rosso, così come della silice residua dall'analisi EDS (figura 15 (f)). Da quest'ultima analisi si può vedere la distribuzione omogenea dell'azoto coordinato al carbonio, e la coordinazione degli atomi di ferro sia in forma di singolo atomo, sia in clusters più grandi.

Le immagini TEM del campione 1c_Fe-N@CMK-8 nelle figure 14 (a) e (b) sottolineano la presenza di una struttura porosa anche se non mostrano alcuna disposizione cristallina, situazione attribuibile al tempo di agitazione troppo breve che non ha permesso alla sorgente di carbonio di diffondersi correttamente all'interno dei pori, nonostante l'impregnazione sia avvenuta in due step successivi.
Questa situazione è stata ulteriormente confermata dall'evaporazione della 1,10-fenantrolina rimasta all'esterno del template, successivamente ricristallizzata su tutte le pareti del reattore di pirolisi a circa 400 °C, visibile in figura 16.
D'altro canto, questo protocollo ha permesso la sintesi di un catalizzatore veramente disperso a livello atomico, poiché l'immagine ZC nella figura 14 (c) non mostra alcun punto luminoso (cluster di Fe).

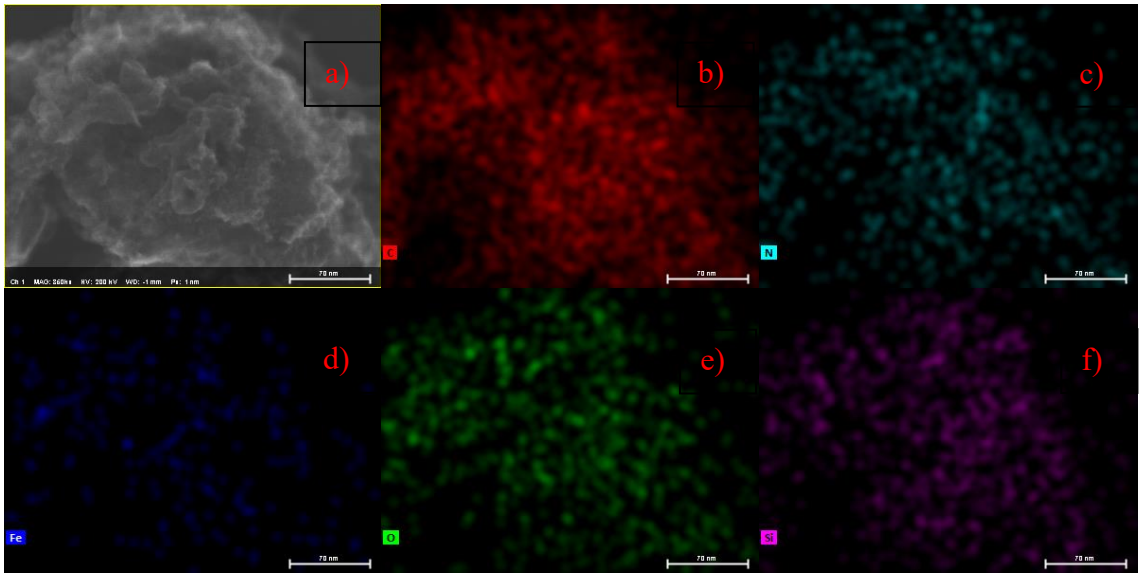

Figura 15. (a),(b),(c),(d),(e),(f) Analisi EDS del campione 1b_Fe-N@CMK-3/8.

Figura 16. 1,10-fenantrolina ricristallizzata sul fondo del reattore di pirolisi.

3.2.3. STUDIO DELL'INFLUENZA DEL'APPROCCIO DI NANOCASTING PARTENDO DAI TEMPLATE SBA-15

Similmente a quanto visto prima, in questa sezione viene presentata l'influenza della scelta del processo di nanocasting sui catalizzatori finali.
Vengono presentati di seguito i risultati della caratterizzazione dei materiali sintetizzati partendo dalla stessa silice SBA-15 seguendo i processi di impregnazione 1 e 3 presentati in sezione 2.2.

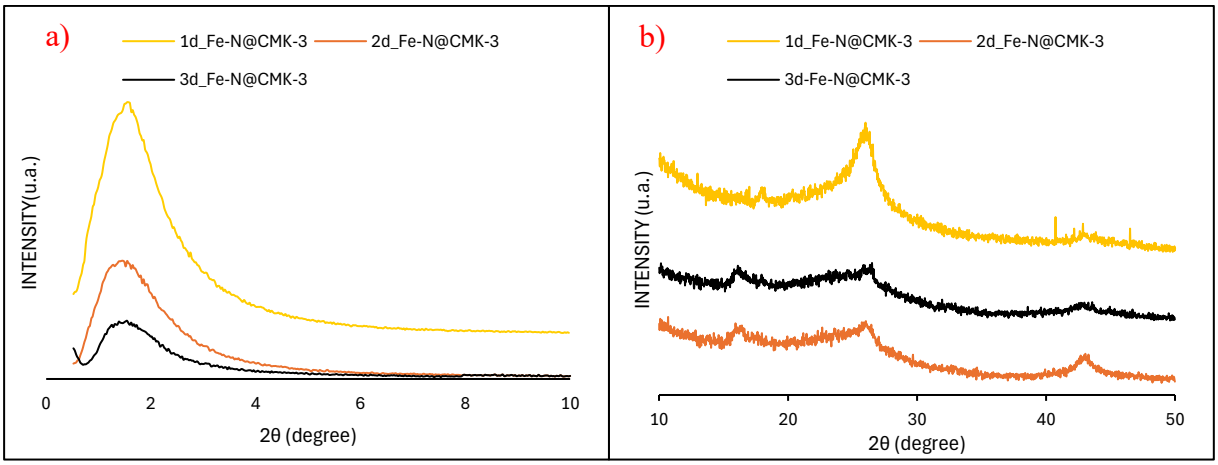

Figura 17. (a) XRD a bassi angoli di incidenza di 1d_Fe-CMK-3, 2d_Fe-N@CMK-3, e 3d_Fe-CMK-8.(b) XRD ad alti angoli di incidenza di 1d_Fe-CMK-3, 2d_Fe-N@CMK-3, e 3d_Fe-CMK-3.

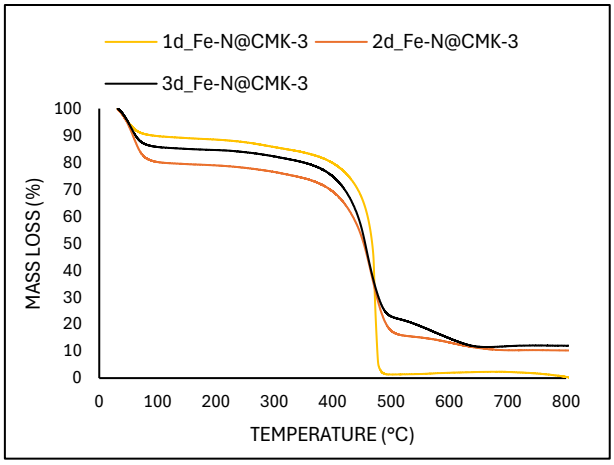

Figura 18. Analisi TG dei catalizzatori derivati dalla silice SBA-15.

I materiali 2d_Fe-N@CMK-3 e 3d_Fe-N@CMK-3 presentano esattamente gli stessi picchi a $2\theta \approx 16°$ (proprio come il campione derivato dal protocollo 2), 26° e 43°, mentre 1d_Fe-N@CMK-3 presenta solo picchi a 26° e 43° relativi al carbonio grafitico, indice che nei campioni 2d e 3d è ancora presente della silice residua.

Le curve TG mostrano la stessa tendenza per i materiali 2d e 3d Fe-N@CMK-3, con lo stesso processo di degradazione per ogni finestra di temperatura e la stessa massa residua del 12%, conferma della presenza di silice residua ipotizzata dal picco di diffrazione a 16°, e di eventuali nanoparticelle di ferro.
Il campione 1d_Fe-N@CMK-3 invece, come già discusso, mostra una degradazione quasi completa, con quasi l'1-2% della massa totale rimanente attribuibile alla silice e nanoparticelle di Fe.

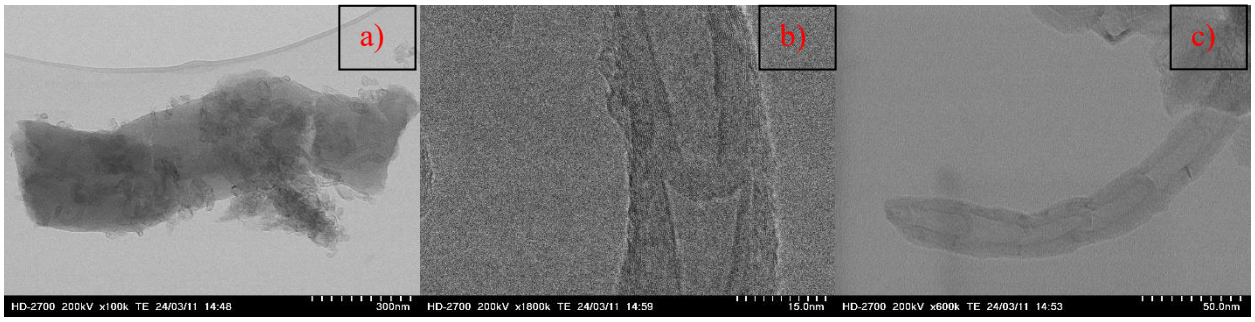

Figura 19. (a),(b),(c). Immagini TEM di 1d_Fe-N@CMK-3.

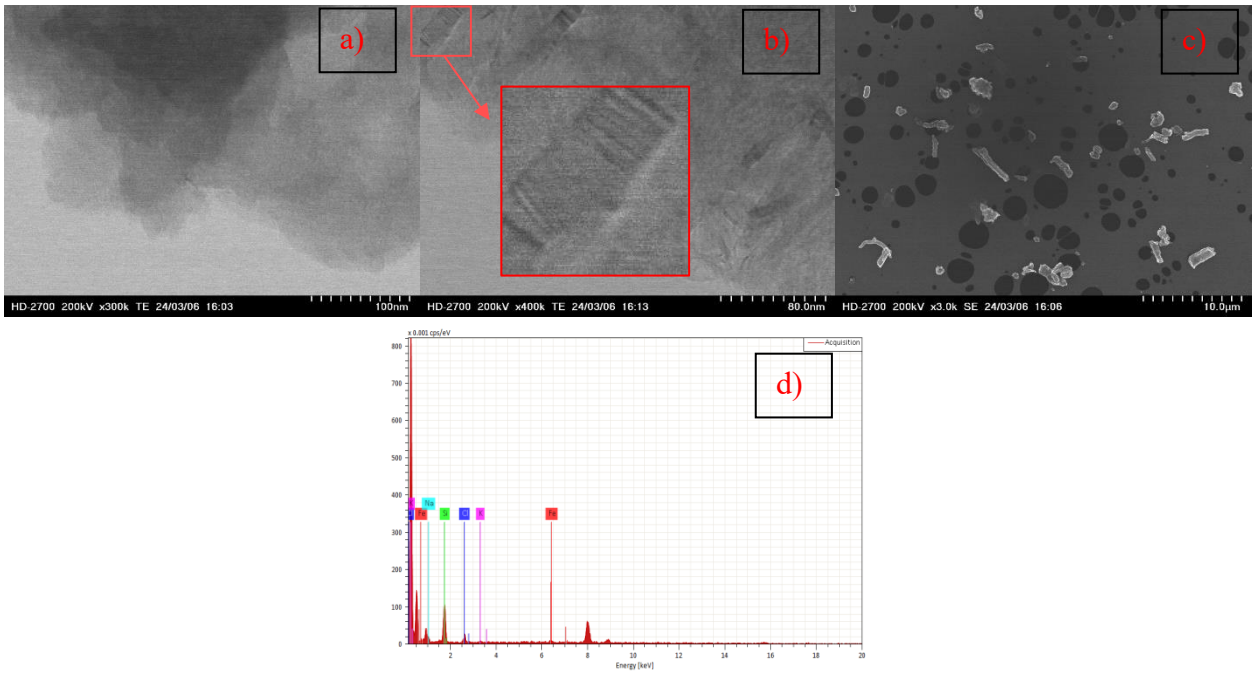

Figura 20. (a),(b),(c),(d) Immagini STEM ed analisi EDS di 2d_Fe-N@CMK-3.

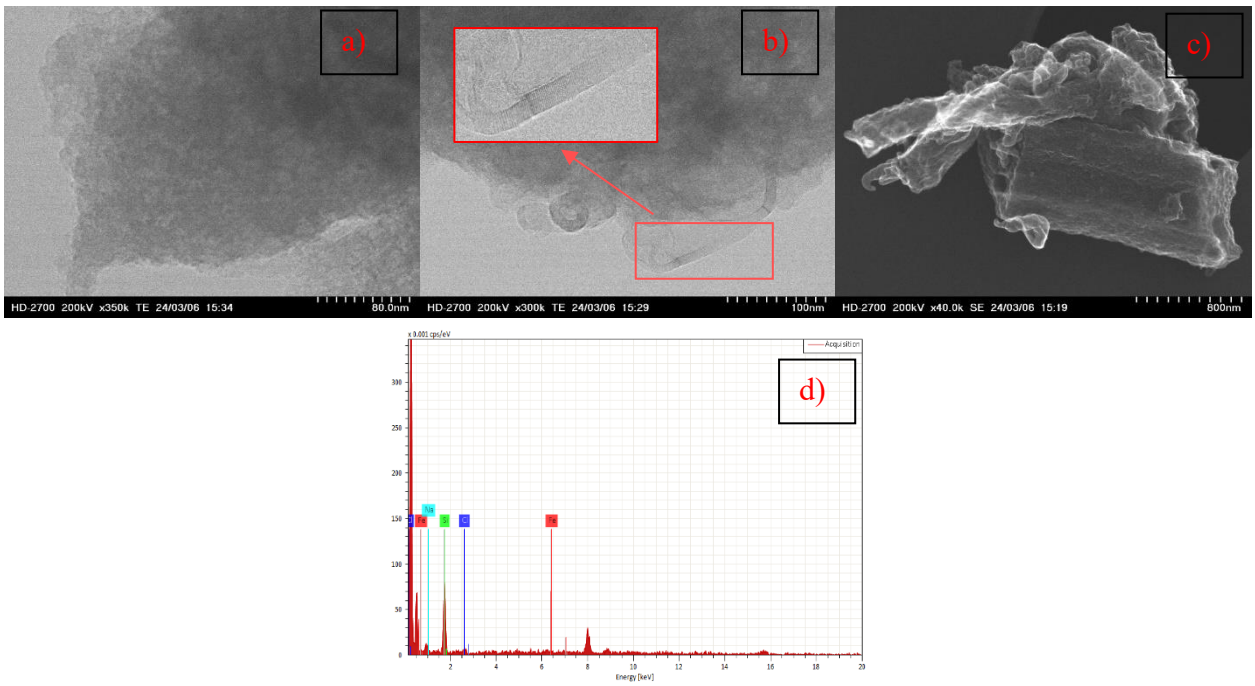

Figura 21. (a),(b),(c),(d) Immagini STEM e analisi EDS di 3d_Fe-N@CMK-3.

Proseguendo con i risultati, le immagini TEM della figura 19 relative a 1d_Fe-N@CMK-3 rivelano un'elevatissima quantità di nanotubi di carbonio (Figura (a)) e la presenza di carbonio grafitico (Figura (b)), in accordo con il picco più netto a 26° discusso in precedenza.
I campioni 2d_Fe-N@CMK-3 e 3d_Fe-N@CMK-3 -sintetizzati rispettivamente seguendo i due passaggi di impregnazione nel pirolizzatore in flusso di azoto e all'interno del reattore chiuso in Teflon - presentano una struttura porosa ma, nonostante l'impregnazione teoricamente migliorata, come il campione 1c_Fe-N@CMK-8 non mostrano alcuna disposizione organizzata della struttura porosa, come si può vedere dalle figure 20 (a) e 21 (a).

Nonostante la mancanza di una struttura ben organizzata rispetto al template di silice, dalle figure 19 (a), 20 (c) e 21 (c) è evidente che mantengono principalmente la macrostruttura a bastoncino tipica del template. Inoltre, tutti mostrano la presenza di nanotubi di carbonio (figure 19 (c), 20 (b), 21 (b)). Più in dettaglio, negli ingrandimenti evidenziati in rosso, si osserva anche la presenza di nanotubi di carbonio a struttura di bambù (BCNT). Questi sono costituiti da compartimenti vuoti separati e "nodi di bambù" che creano una struttura segmentata, simile ai fusti di bambù. I compartimenti aperti nei BCNT facilitano il trasporto di massa di reagenti e prodotti verso e dagli atomi di ferro. Ciò migliora l'efficienza della reazione garantendo un flusso più fluido dei materiali all'interno del catalizzatore.
Tuttavia, dagli spettri EDS (figure 20 (d), 21 (d)) si può notare che, esattamente come nei campioni precedenti, è presente una quantità relativamente alta di silice residua, così come del cloro e del sodio derivanti dai processi di etching.

3.2.4. STUDIO DELL'EFFETTO DEL SECONDO STEP DI PIROLISI PER INCREMENTARE IL GRADO DI GRAFITIZZAZIONE

Dai risultati sopra citati appare evidente che due problemi principali ostacolano il raggiungimento di una struttura ottimale, che si rifletterebbe anche sull'attività elettrocatalitica:

1. La presenza di silice residua nonostante i due step di etching;
2. La mancanza di una struttura cristallina ordinata.

Nel tentativo di risolvere tali problemi, un secondo processo di pirolisi a 900°C per un'ora è stato eseguito sui campioni 1b_Fe-N@CMK-3/8, 1c_Fe-N@CMK-8, e 1d_Fe-N@CMK-3.
Tuttavia, nonostante il risultato aspettato in linea con la letteratura, dall'analisi XRD mostrata in figura 22 e dalle immagini al TEM in figura 23 è possibile notare come non solo vi è stata una mancanza di ricristallizzazione ma, al contrario, essi abbiano anche perso le strutture cristalline che possedevano.

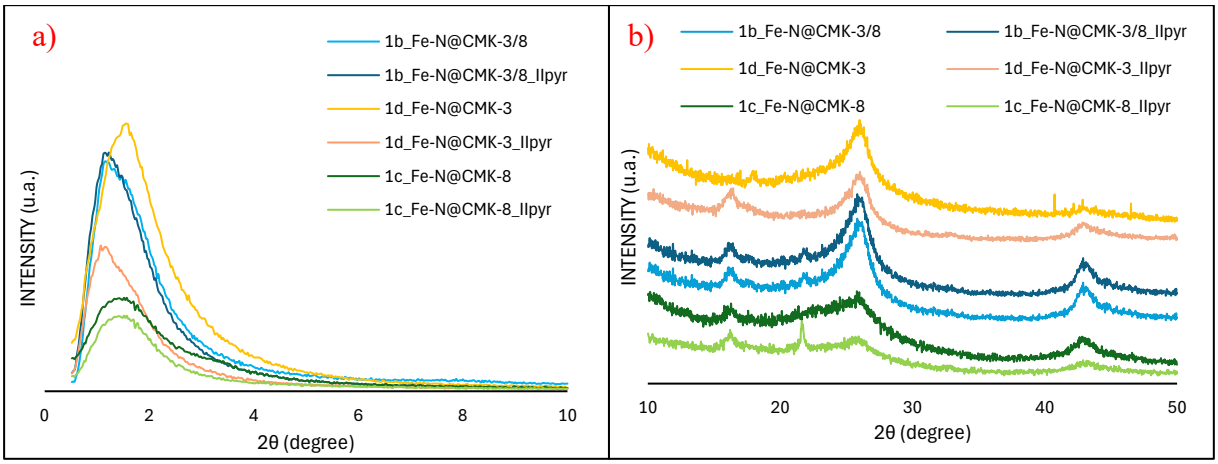

Figura 22. (a),(b). Confronto tra grafici XRD di 1b_Fe-N@CMK-3/8, 1c_Fe-N@CMK-8, e 1d_Fe-N@CMK-3 originali e pirolizzati due volte.

Si può notare una diminuzione complessiva nell'intensità dei picchi di diffrazione, segno di un incremento della percentuale amorfa nei materiali, condizione confermata dalle immagini TEM in figura 23 che mostrano la presenza di una struttura appena porosa e senza alcun tipo di organizzazione. I picchi di diffrazione a raggi X appaiono agli stessi valori di 2θ (16°,22°, 26°, e 43°) attribuibili alla presenza SiO_2 ed alla presenza di una piccola percentuale di grafite.

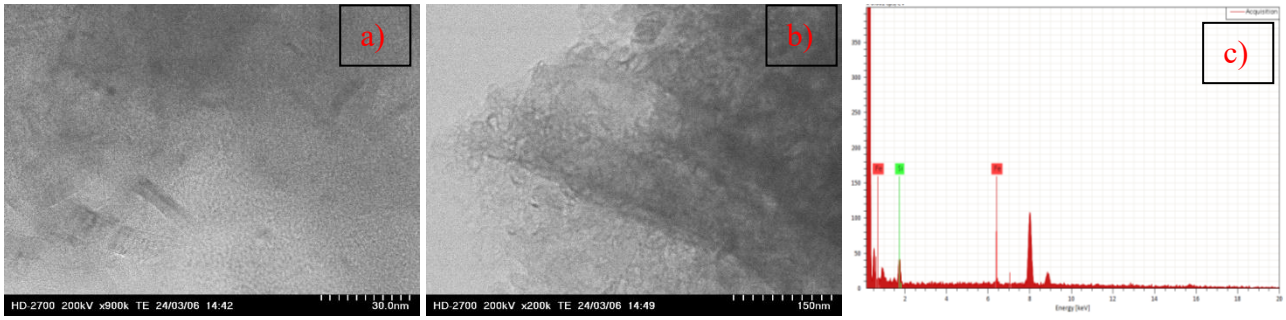

Figura 23. (a),(b),(c). Immagini TEM e spettro EDS del campione 1b_Fe-N@CMK-3/8_IIpyr.

3.3. STUDIO DELLE PRESTAZIONI ELETTROCATALITICHE

Le prove elettrochimiche sui catalizzatori appena sintetizzati sono state condotte in un sistema a tre elettrodi con un elettrodo a disco rotante (RDE) e con un elettrodo a disco-anello rotante (RRDE) con un anello di platino come secondo elettrodo di lavoro.

I catalizzatori sono stati depositati sul disco carbonio vetroso, con una superficie di 0,1256 cm^2.
La prova prevede l'utilizzo del disco rivestito del catalizzatore in esame e l'anello in platino come elettrodi di lavoro, un contro elettrodo costituito da un'asta di carbonio grafitico e un elettrodo di riferimento.
La prima parte sperimentale è stata eseguita negli Stati Uniti con un elettrodo di riferimento ad idrogeno reversibile (RHE), mentre la seconda parte è stata eseguita in Italia con un elettrodo di riferimento Ag/AgCl.
In quest'ultimo caso, per poter effettuare confronti, il potenziale misurato è stato riportato all'RHE sulla base dell'equazione di Nernst.
I catalizzatori sono stati prima dispersi in una soluzione nafion/isopropanolo, dove il nafion funge da legante, e poi depositati tramite drop-casting sull'elettrodo a disco.
Per ogni catalizzatore l'inchiostro da depositare è stato preparato miscelando 2 mg di polvere di catalizzatore, 400 μl di isopropanolo e 10 μl di Soluzione di resina perfluorurata Nafion (5 wt.%). Tale sospensione è stata sonicata per 10 minuti per poi depositare 10.3 μl di inchiostro sul supporto in carbonio vetroso per ottenere il loading di catalizzatore desiderato di 0.4 mg/cm^2. L'elettrodo rivestito è stato successivamente lasciato ad asciugare all'aria.

Le misurazioni effettuate sono le seguenti, sia in ambiente acido (in soluzione 0.1 M $HClO_4$, pH=1)sia alcalino (soluzione 0.1 M KOH, pH=13):

1. Voltammetria ciclica (CV) in N_2 e O_2 ad una velocità di 100 mV/s in seguito ad una più rapida a 500 mV/s fatta per 100 cicli in N_2 per attivare e pulire l'elettrodo da eventuali contaminazioni e/o ossidi presenti.
2. Voltammetria a scansione lineare (LSV) a 400, 900, 1600 e 2500 giri al minuto (rpm).
3. Voltammetria a scansione lineare (LSV) a 1600 rpm con il setup RRDE per calcolare il quantitativo di H_2O_2 prodotto durante ORR ed il numero di elettroni che prendono parte alla reazione di riduzione.

Le correnti misurate sono state normalizzate per la superficie geometrica del disco (0.1256 cm^2).
Le curve di polarizzazione anodica sono state analizzate per estrapolare i descrittori tipici per la reazione ORR: il potenziale di onset (E_{on}) che corrisponde a una densità di corrente di 0.1 mA/cm^2, il potenziale di mezza onda ($E_{1/2}$) calcolato attraverso il metodo della derivata prima, il numero di elettroni trasferiti attraverso la reazione elettrochimica (n) e la resa in perossido di idrogeno ($\%H_2O_2$) valutate attraverso le equazioni 10 e 11:

$$n = \frac{4\, I_d\, N}{I_d\, N + I_r} \qquad (10)$$

$$\%H_2O_2 = 100\frac{2\, I_r}{I_d\, N + I_r} \qquad (11)$$

Dove I_d è la corrente misurata al disco, I_r è la corrente all'anello ed N è il collection efficiency funzione della geometria del RRDE e delle proprietà di diffusione dei prodotti di reazione, il cui valore corrisponde a 0.4 per il macchinario in Italia, 0.37 per quello negli Stati Uniti.

In linea teorica, un numero di elettroni uguale a 4 implica che il la reazione di riduzione segue il percorso a 4 e^- e che quindi non viene prodotto perossido di idrogeno, vantaggioso per la performance, mentre elevati valori di E_{on} e di $E_{1/2}$ sono indicatori di un'elevata attività elettrocatalitica, in quanto è richiesto una sovratensione minore per ottenere un determinato valore di densità di corrente.

3.3.1. STUDIO DELL'INFLUENZA DELLA SCELTA DEL TEMPLATE SULLE PERFORMANCE CATALITICHE

In figura 24 e 25 vengono presentate rispettivamente le curve di polarizzazione ed il numero di elettroni/$\%H_2O_2$ formati durante la reazione di riduzione dell'ossigeno, utilizzando i catalizzatori sintetizzati partendo dalle silici KIT-6-*p6mm*, KIT-6-*dual*, e SBA-15.

Le curve LSV di 1b_Fe-N@CMK-3/8 e 1d_Fe-N@CMK-3 mostrano andamento e valori simili a quelli del catalizzatore commerciale al platino in condizioni sia acide che alcaline.
Il campione 1a_Fe-N@CMK-8 sintetizzato da KIT-6-*p6mm* mostra buoni risultati in condizioni alcaline, mentre in ambiente acido è meno performante. Questo risultato è ulteriormente confermato dai valori riportati nella tabella 3, dove mostra la più alta quantità di specie a base di perossido di idrogeno e un numero di elettroni inferiore alla media. Nel complesso, il miglior catalizzatore Fe-N-C risulta essere 1d_Fe-N@CMK-3 immediatamente seguito da 1b_Fe-N@CMK-3/8, i cui valori di E_{on} ed $E_{1/2}$ in KOH sono molto simili a quelli del Pt/C, mentre in $HClO_4$ i valori sono solo 16 mV e

22 mV inferiori, rispettivamente. Considerando il metodo di sintesi uniforme per tutti i catalizzatori, le differenze osservate nell'attività ORR possono essere attribuite all'influenza del supporto di carbonio. Si ipotizza che l'utilizzo di un template in silice con elevata area superficiale specifica e una struttura porosa più ordinata promuova la formazione ed una migliore accessibilità dei siti attivi per la reazione.

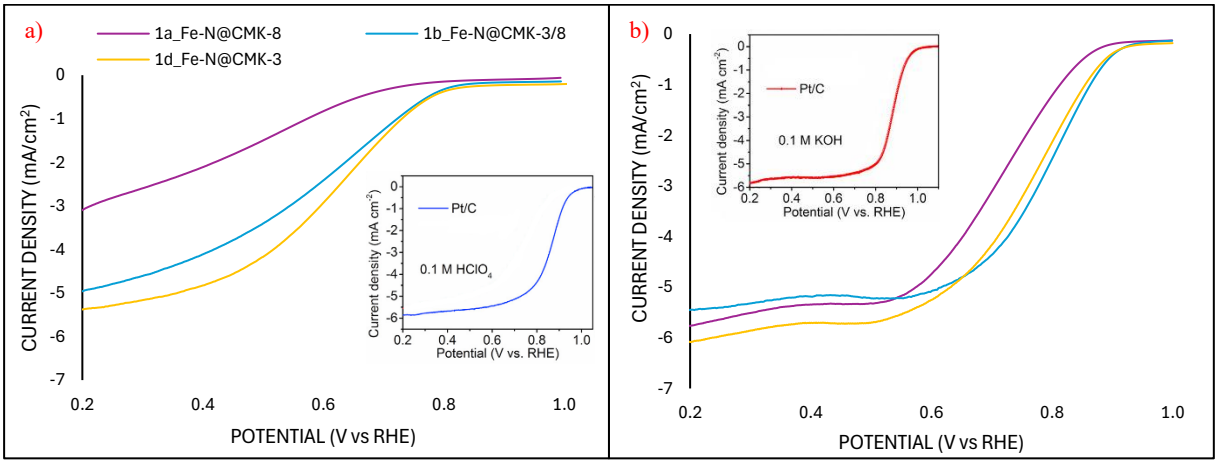

Figura 24. Test elettrochimici fatti negli Stati Uniti su RRDE e confronto con i catalizzatori commerciali a base di platino Pt/C (20 wt.%): curve di polarizzazione ORR a 1600 rpm. (a) in soluzione 0.1 M $HClO_4$. (b) in soluzione 0.1 M KOH.

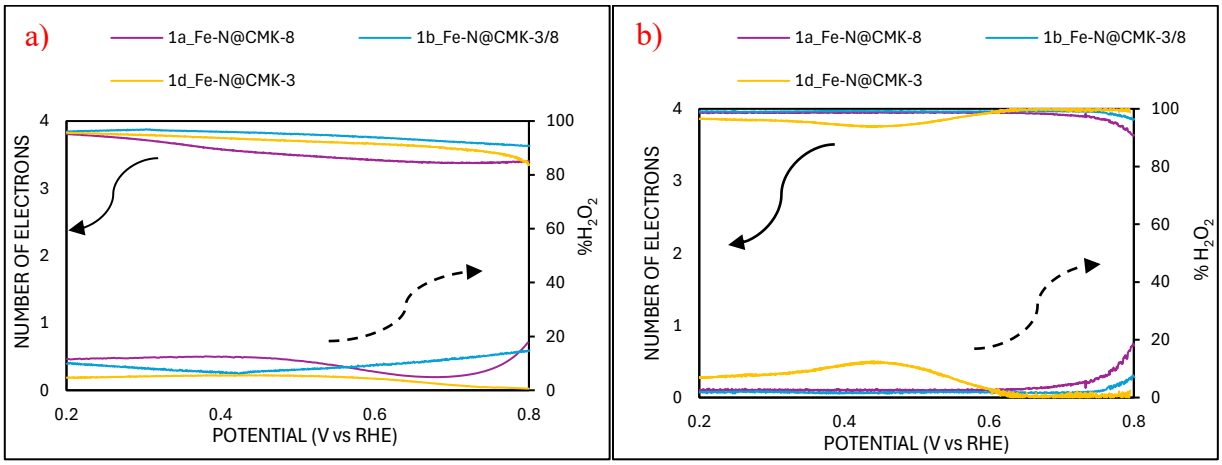

Figura 25. Numero di elettroni e percentuale di H_2O_2 calcolati da RRDE a 1600 rpm. (a) in soluzione 0.1 M $HClO_4$. (b) in soluzione 0.1 M KOH.

Tabella 3. Confronto delle performance durante ORR tra i catalizzatori testati negli Stati Uniti e quello commerciale Pt/C (20 wt.%) in 0.1 M KOH and 0.1 M $HClO_4$ a 1600 rpm.

	E_{onset} (V vs. RHE)		**$E_{1/2}$ (V vs. RHE)**		**n_{medio} (-)**		**$\%H_2O_{2,\ medio}$ (-)**	
	0.1 M KOH	0.1 M $HClO_4$	0.1 M KOH	0.1 M $HClO_4$	0.1 M KOH	0.1 M $HClO_4$	0.1 M KOH	0.1 M $HClO_4$
1a_Fe-N@CMK-8	0.87	0.69	0.75	0.6	3.93	3.49	3.60	10.91
1b_Fe-N@CMK-3/8	0.91	0.80	0.82	0.69	3.95	3.81	2.02	9.21
1d_Fe-N@CMK-3	0.91	0.89	0.8	0.64	3.87	3.74	3.61	4.17
Pt/C	0.90	0.96	0.82	0.88	3.99	3.99	0.35	0.49

3.3.2. STUDIO DELL'INFLUENZA DELL'APPROCCIO DI NANOCASTING A PARTIRE DA KIT-6 E DERIVATI SULLE PERFORMANCE CATALITICHE

In questa sezione viene studiato l'effetto dei diversi approcci di nanocasting descritti nei protocolli 1 e 2 della sezione 2.2 sull'attività catalitica.
Riassumendo brevemente, i campioni 1a_Fe-N@CMK-8 e 1b_Fe-N@CMK-3/8 sono stati sintetizzati rispettivamente da KIT-6-*p6mm* e KIT-6-*dual* seguendo i classici passaggi di impregnazione citati nel protocollo 1. Il campione 1c_Fe-N@CMK-8 invece deriva dalla silice KIT-6 ed è stato impregnato all'interno della muffola come descritto nel protocollo 2 della stessa sezione.

La figura 26 mostra le curve LSV dei campioni citati, mentre la figura 27 mostra il numero di elettroni che partecipano alla reazione e la quantità di H_2O_2 prodotta all'interno dell'intervallo di potenziale di lavoro. Infine, nella tabella 4 è riportato un riepilogo delle prestazioni rispetto al Pt/C commerciale.
I catalizzatori ottenuti con il protocollo 1 mostrano buoni risultati - in particolare 1b_Fe-N@CMK-3/8 come già accennato nella sezione 3.4.1- e il numero medio di elettroni che partecipano all'ORR e la quantità di H_2O_2 suggeriscono che il percorso principalmente seguito sia quello a 4 e-, dimostrando le loro buone prestazioni sia in ambiente acido che alcalino.
Le prestazioni catalitiche del campione 1c_Fe-N@CMK-8 rispecchiano le sue peggiori proprietà morfologiche analizzate nella sezione 3.2.2 rispetto agli altri: la migliore dispersione degli atomi di ferro all'interno della matrice di carbonio (evidenziata dall'assenza di cluster di Fe nell'immagine ZC 14 (c)) non è sufficiente a superare la mancanza di una buona organizzazione della rete porosa, confermando le limitazioni del trasporto di massa che si verificano nei carboni altamente amorfi.
I valori di E_{on} ed $E_{1/2}$ sono inferiori di 20-30 mV rispetto agli altri catalizzatori Fe-N-C, mentre la figura 27 suggerisce che con questo campione il percorso principale sia quello a 2+2 e-, confermato anche dalla grande quantità di perossido di idrogeno prodotta.

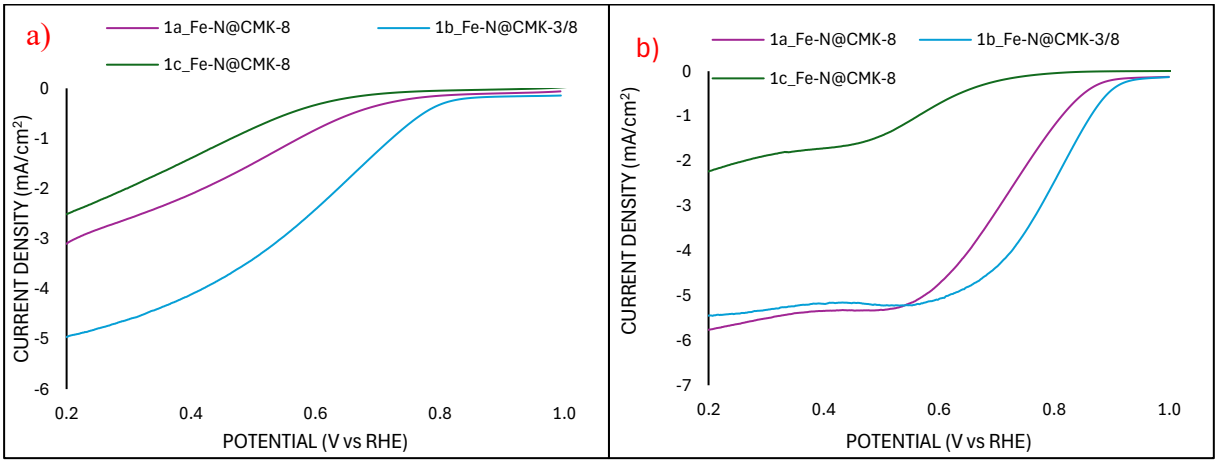

Figura 26. Test elettrochimici fatti negli Stati Uniti e in Italia su RRDE dei catalizzatori provenienti dai template KIT-6: curve di polarizzazione ORR a 1600 rpm. (a) in soluzione 0.1 M $HClO_4$. (b) in soluzione 0.1 M KOH.

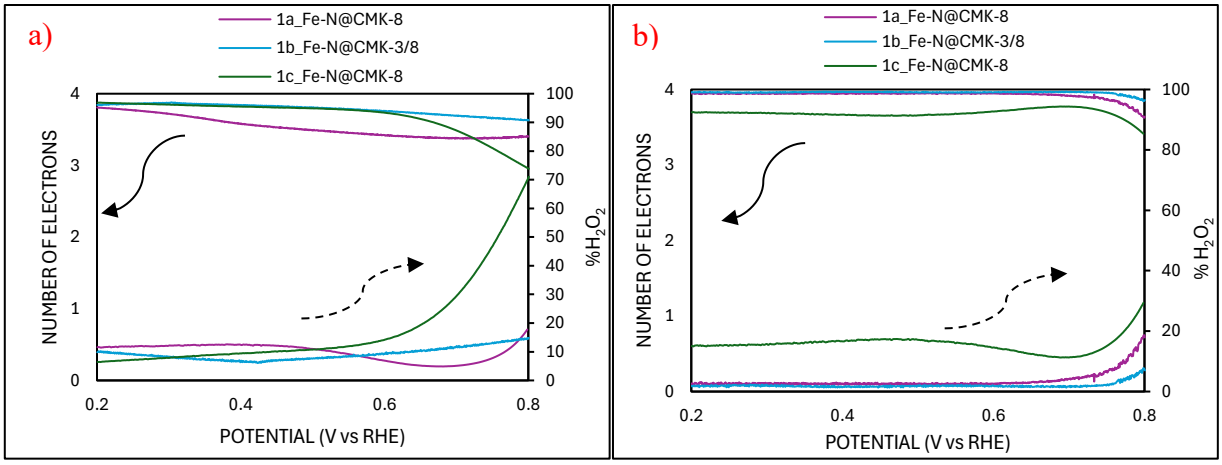

Figura 27. Numero di elettroni e percentuale di H_2O_2 calcolati da RRDE a 1600 rpm. (a) in soluzione 0.1 M $HClO_4$. (b) in soluzione 0.1 M KOH.

Tabella 4. Confronto delle performance durante ORR tra i catalizzatori Fe-N-C e quello commerciale Pt/C (20 wt.%) in 0.1 M KOH and 0.1 M $HClO_4$ a 1600 rpm

	E_{on} (V vs. RHE)		**$E_{1/2}$ (V vs. RHE)**		**n_{medio} (-)**		**$\%H_2O_{2,\,medio}$ (-)**	
	0.1 M KOH	0.1 M $HClO_4$	0.1 M KOH	0.1 M $HClO_4$	0.1 M KOH	0.1 M $HClO_4$	0.1 M KOH	0.1 M $HClO_4$
1a_Fe-N@CMK-8	0.87	0.69	0.75	0.6	3.93	3.49	3.60	10.91
1b_Fe-N@CMK-3/8	0.91	0.80	0.82	0.69	3.95	3.81	2.02	9.21
1c_Fe-N@CMK-8	0.68	0.61	0.56	0.43	3.68	3.70	15.68	17.80
Pt/C	0.90	0.96	0.82	0.88	3.99	3.99	0.35	0.49

3.3.3. STUDIO DELL'INFLUENZA DELL'APPROCCIO DI NANOCASTING A PARTIRE DA SBA-15 SULLE PERFORMANCE CATALITICHE

Nelle figure 28 e 29 viene confrontata l'attività catalitica dei campioni sintetizzati dallo stesso template SBA-15 con diversi processi di impregnazione, mentre la tabella 5 riassume i risultati citati. Si osserva una migliore attività catalitica per i catalizzatori 2d_Fe-N@CMK-3 e 3d_Fe-N@CMK-3 sintetizzati dallo stampo SBA-15 mediante impregnazione rispettivamente sotto flusso di azoto e in reattore chiuso in Teflon rispetto al catalizzatore proveniente da KIT-6 sintetizzato all'interno della muffola discusso nella sezione 3.4.2.

Più precisamente, il campione 3d_Fe-N@CMK-3 mostra la migliore attività tra i catalizzatori provenienti dai protocolli 2 e 3, indicando che la maggiore pressione all'interno del reattore chiuso durante il trattamento termico ha effettivamente permesso una migliore diffusione dei precursori.

Tuttavia, il miglior catalizzatore risulta essere 1d_Fe-N@CMK-3 ottenuto dalla classica via di sintesi nel protocollo 1, il quale presenta valori di E_{on} ed $E_{1/2}$ quasi uguali a quelli del catalizzatore Pt/C in elettrolita alcalino, mentre in acido differisce solo di 16 mV e 24 mV, rispettivamente.

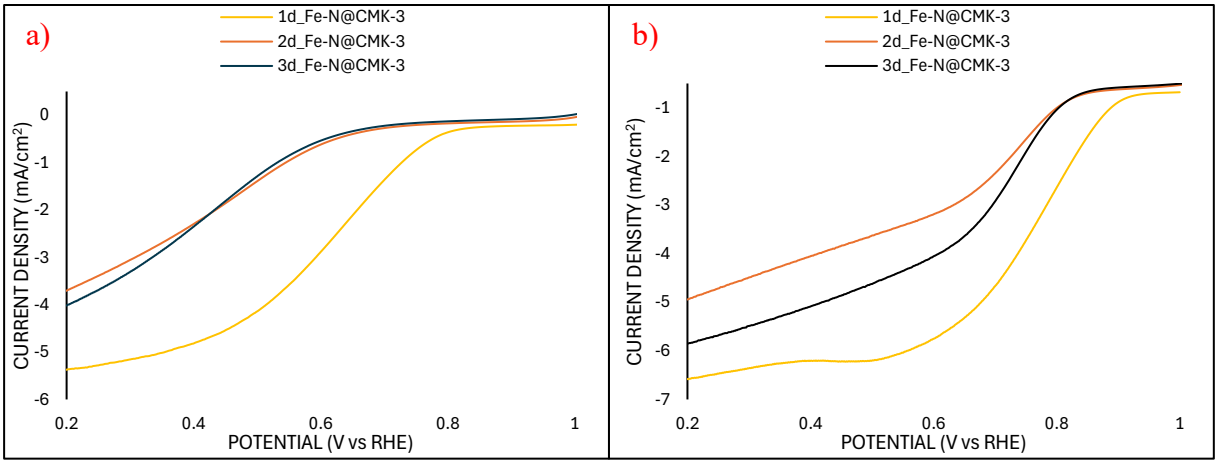

Figura 28. Test elettrochimici fatti negli Stati Uniti e in Italia su RRDE dei catalizzatori provenienti da SBA-15: curve di polarizzazione ORR a 1600 rpm. (a) in soluzione 0.1 M $HClO_4$. (b) in soluzione 0.1 M KOH.

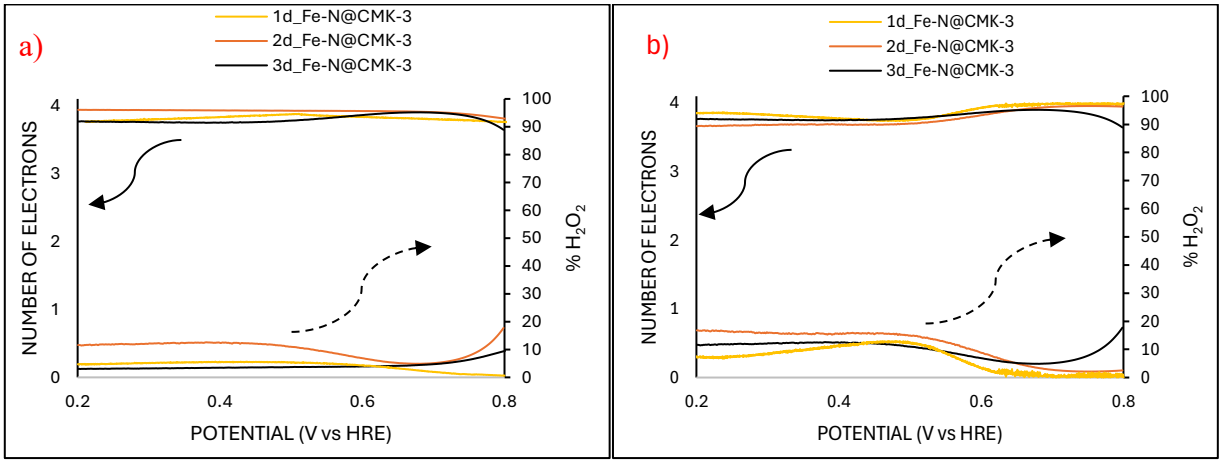

Figura 29. Numero di elettroni e percentuale di H_2O_2 calcolati da RRDE a 1600 rpm. (a) in soluzione 0.1 M $HClO_4$. (b) in soluzione 0.1 M KOH.

Tabella 5. Confronto delle performance durante ORR tra i catalizzatori Fe-N-C e quello commerciale Pt/C (20 wt.%) in 0.1 M KOH and 0.1 M $HClO_4$ a 1600 rpm

	E_{on} (V vs. RHE)		**$E_{1/2}$ (V vs. RHE)**		**n_{medio} (-)**		**$\%H_2O_{2,\,medio}$(-)**	
	0.1 M KOH	0.1 M $HClO_4$	0.1 M KOH	0.1 M $HClO_4$	0.1 M KOH	0.1 M $HClO_4$	0.1 M KOH	0.1 M $HClO_4$
1d_Fe-N@CMK-3	0.91	0.89	0.8	0.64	3.87	3.74	3.61	4.17
2d_Fe-N@CMK-3	0.81	0.62	0.75	0.42	3.77	3.91	11.26	4.12
3d_Fe-N@CMK-3	0.68	0.61	0.56	0.43	3.8	3.78	9.93	9.21
Pt/C	0.90	0.96	0.82	0.88	3.99	3.99	0.35	0.49

3.3.4. STUDIO DELL'EFFETTO DEL SECONDO STEP DI PIROLISI SULL'ATTIVITÀ ELETTROCATALITICA

In quest'ultima sezione viene confrontata l'attività catalitica dei campioni sintetizzati con la rispettiva versione pirolizzata due volte nel tentativo di aumentare il tasso di cristallinità e distribuire meglio il ferro all'interno della struttura.

Nonostante quanto previsto dalla diminuzione complessiva del grado di cristallinità dopo la seconda pirolisi, confrontando le curve LSV in condizioni sia acide che basiche alla stessa velocità di rotazione in figura 30, si osserva un potenziale di onset 20 mV più alto per il campione 1c_Fe-N@CMK-8_IIpyr rispetto al campione pirolizzato una sola volta, mentre si verifica una diminuzione del potenziale di mezza onda di quasi lo stesso valore. Il numero medio di elettroni è aumentato sia in condizioni acide che alcaline, ed è stato registrato un drastico calo del 4,4% e del 13,7% nell'H_2O_2 generata rispettivamente negli elettroliti alcalini e acidi.
Questo può essere collegato a una migliore ridispersione degli atomi di ferro e a un maggiore grado di grafitizzazione nel campione che originariamente mostrava solo un accenno di porosità all'interno della struttura mesoporosa, direttamente collegato a un maggior numero di siti attivi disponibili per la reazione ORR.
Sugli altri due campioni i risultati sono appena visibili; i miglioramenti mostrati in un elettrolita vengono bilanciati da un peggioramento simultaneo nell'altro.

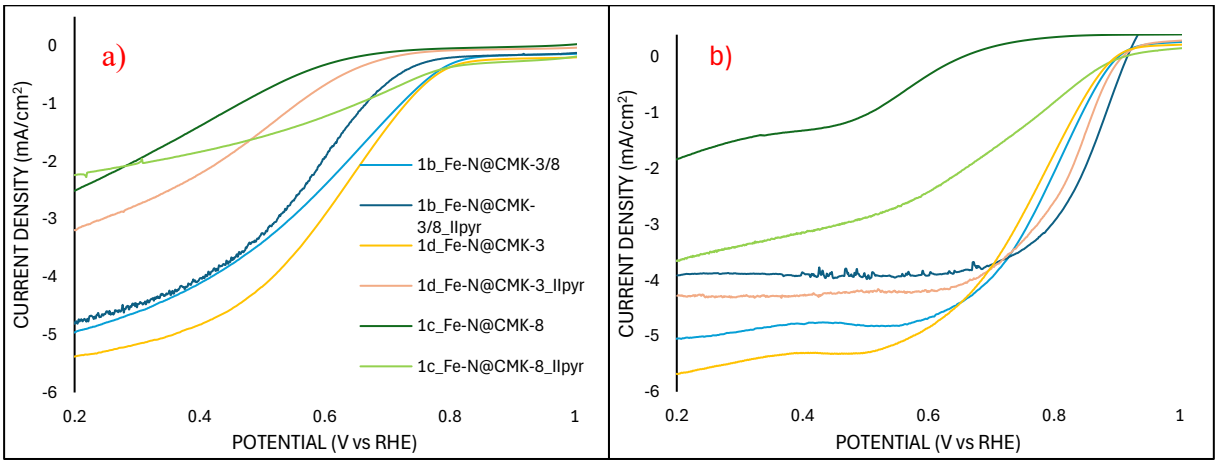

Figura 30. Confronto delle performance elettrochimiche dei materiali pirolizzati di nuovo. (a) in soluzione 0.1 M $HClO_4$. (b) in soluzione 0.1 M KOH .

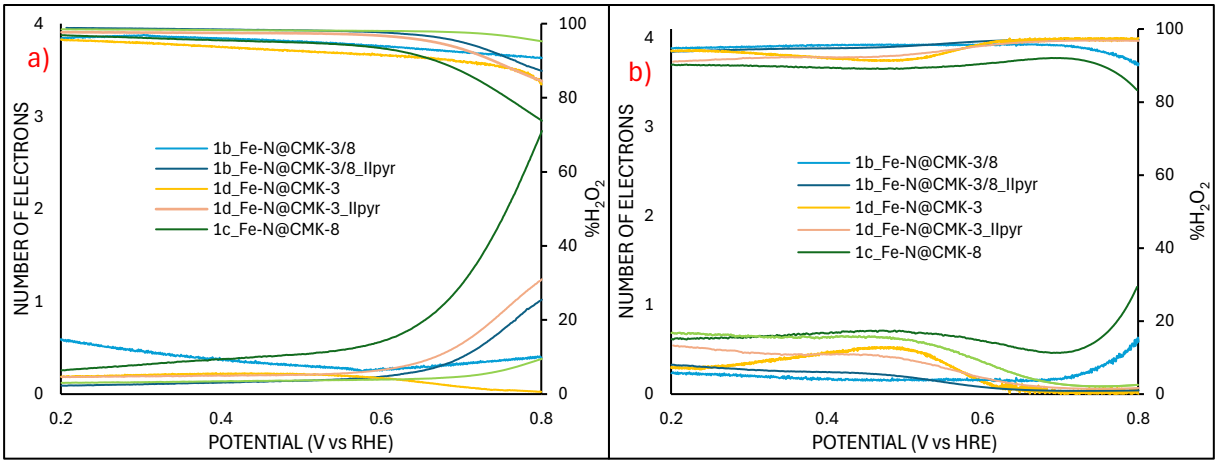

Figura 29. Numero di elettroni e percentuale di H_2O_2 calcolati da RRDE a 1600 rpm. (a) in soluzione 0.1 M $HClO_4$. (b) in soluzione 0.1 M KOH.

Tabella 6. Confronto delle performance durante ORR tra i catalizzatori Fe-N-C pirolizzati rispettivamente una e due volte.

	E_{on} (V vs. RHE)		**$E_{1/2}$ (V vs. RHE)**		**n_{medio} (-)**		**$\%H_2O_{2,\,medio}$ (-)**	
	0.1 M KOH	0.1 M $HClO_4$	0.1 M KOH	0.1 M $HClO_4$	0.1 M KOH	0.1 M $HClO_4$	0.1 M KOH	0.1 M $HClO_4$
1b_Fe-N@CMK-3/8	0.91	0.80	0.82	0.69	3.95	3.81	2.02	9.21
1b_Fe-N@CMK-3/8_IIpyr	0.93	0.71	0.81	0.49	3.91	3.88	4.11	6.14
1c_Fe-N@CMK-8	0.68	0.61	0.56	0.43	3.68	3.69	15.68	17.80
1c_Fe-N@CMK-8_IIpyr	0.88	0.8	0.25	0.22	3.77	3.91	11.24	4.11
1d_Fe-N@CMK-3	0.91	0.89	0.8	0.64	3.87	3.74	3.61	4.17
1d_Fe-N@CMK-3_IIpyr	0.68	0.61	0.56	0.43	3.85	3.83	7.53	8.62
Pt/C	0.90	0.96	0.82	0.88	3.99	3.99	0.35	0.49

CONCLUSIONI E PROSPETTIVE FUTURE

In conclusione, questo studio ha esplorato lo sviluppo di un catalizzatore a base di metalli non preziosi per la reazione di riduzione dell'ossigeno (ORR) nelle celle a combustibile. L'obiettivo principale era quello di creare un catalizzatore con elevata attività e selettività verso il percorso a quattro elettroni, per superare la cinetica lenta al catodo e ridurre la formazione di perossido di idrogeno che influisce sull'efficienza. Questo approccio si allinea con la necessità di tecnologie per l'energia pulita economiche e ampiamente disponibili. I catalizzatori Fe-N-C sintetizzati hanno mostrato buone caratteristiche morfologiche, confermate dall'analisi dell'adsorbimento di azoto, con un'ampia superficie specifica e dimensioni dei pori adeguate. Lo studio ha inoltre evidenziato il ruolo cruciale giocato dalla scelta del template di silice e dall'approccio di nanocasting seguito sui risultati finali.

In futuro, ulteriori ricerche potrebbero indagare l'impatto della variazione del contenuto di ferro all'interno del catalizzatore sulle sue prestazioni. Inoltre, è fondamentale ottimizzare il processo di etching per rimuovere completamente il template e ridurre al minimo la contaminazione di silicio, al fine di garantire il vero comportamento elettrochimico del catalizzatore.

Da un punto di vista commerciale, una valutazione del ciclo di vita (LCA) e un'analisi di fattibilità economica della produzione su larga scala fornirebbero preziose informazioni sulla sostenibilità complessiva e praticità di questo catalizzatore Fe-N-C rispetto alle alternative esistenti a base di Pt.

1. Introduction

Climate change is a global phenomenon that poses significant challenges to our planet and its inhabitants. In recent years, the causes and consequences of climate change have become increasingly evident, highlighting the urgent need for action.
The increase of the CO_2 concentration in the atmosphere over the past two hundred years, mainly from fossil fuel combustion, is the root cause that leaded, and keeps leading, to an increase in the global temperatures and other changes in Earth's climate. In terms of numbers, since the onset of industrial times in the 18th century, human activities have raised atmospheric CO_2 by 50% – meaning the amount of CO_2 is now 150% of its value in 1750.
In the figure 1, it is possible to see this increase trend over the decades. [1]

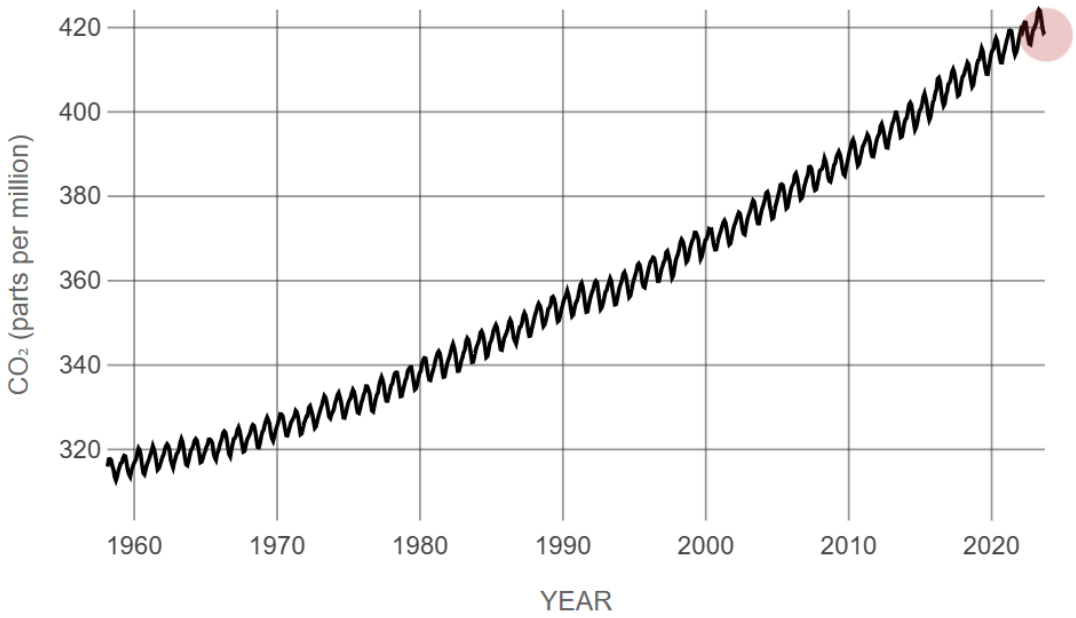

Figure 1. *Atmospheric CO_2 levels measured by NOAA at Mauna Loa Observatory, Hawaii.*[1]

With that being said, it is straightforward to understand that radical actions must be taken in order to preserve our planet.
Among them, one of the most important is the production of environmentally friendly energy, through the use of hydrogen as energy carrier in the proton exchange membrane fuel cells (PEMFC).
PEMFCs have emerged as promising clean energy conversion devices due to their attractive characteristics. These include high efficiency in converting chemical energy to electricity, a compact design leading to high energy density, and the potential for near-zero emissions. PEMFCs hold significant application potential in various sectors, including transportation (electric vehicles), stationary and portable power generation, and micro-power applications for powering electronic devices. [3]
However, widespread commercialisation of PEMFC technology faces two key technical challenges: cost and durability. Fuel cell catalysts, particularly platinum (Pt)-based materials and the catalyst layers they form, are a major contributor to both limitations. High Pt costs significantly inflate overall fuel cell system prices. Additionally, Pt-based catalysts suffer from degradation and activity loss over time, hindering long-term fuel cell performance and reliability.

Consequently, the development of novel and more affordable catalysts with improved activity and enhanced durability represents a critical research thrust in PEMFC technology. Optimising catalyst design, exploring alternative materials to Pt, and reducing Pt content in catalysts are all active areas of research aimed at overcoming these hurdles and paving the way for broader PEMFC commercialisation.

On overall, we can list the main problems that nowadays humper this technology from being fully functional:

a) The high bond energy of the O_2 molecule (498 kJ/mol) makes it very stable. Due to this sluggish kinetics, the ORR is considered the potential limiting step that reduces the overall performance of fuel cell devices.
b) If the reaction follows the 2+2 e^- electrons pathway, the H_2O_2 and OOH^- peroxide species' formation both reduces the overall energy conversion efficiency and causes corrosion of the cell's components. [2]

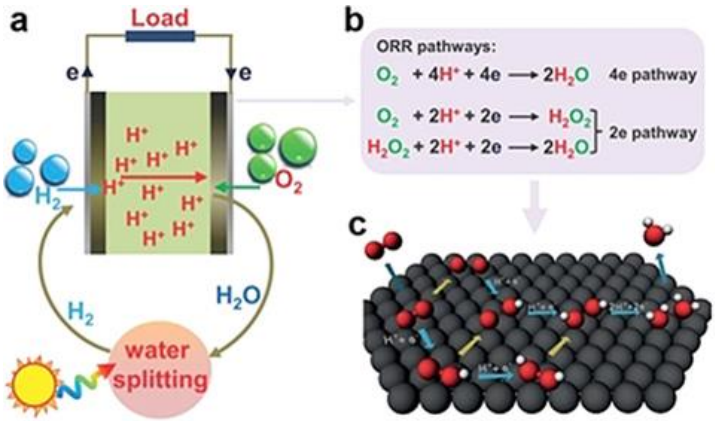

Figure 2. *Schematic representation of a H_2-O_2 fuel cell with H2 generated from the water splitting driven by solar energy.*[3]

In figure 2 it is represented a possible configuration of environmentally friendly electrical energy production, involving the PEMFC fuel cell coupled with solar driven water splitting system in order to produce the needed hydrogen.

Several efforts have been done to overcome those problems and, among the best solutions, the single-atom catalysts (SACs) have emerged due to their nonprecious metal-based synthesis and their distinct and remarkable performance in many industrially relevant thermo-, photo-, and electrochemical conversions.
SACs consist of isolated metal atoms, which are individually anchored to the adjacent atoms in the host material and represent the active sites for the reactions. [2]
These new materials have attracted much attention for their maximised atom utilisation, which allows to reduce waste of material and money, for their high selectivity and activity in electrochemical reactions, and for their tunable catalytic properties.
A further understanding of the SACs is described in the paragraph 1.4.

1.1. *ORR*: thermodynamics and kinetics

PEMFCs function through a series of electrochemical reactions occurring at the interface between the electrodes and the electrolyte membrane. [4] Hydrogen gas is fed to the anode compartment where, when in contact with the electrode, it undergoes the hydrogen oxidation reaction (HOR). Simultaneously, oxygen or air is supplied to the cathode compartment, where the oxygen reduction reaction (ORR) takes place. These two half-reactions, separated by the proton-conducting membrane, combine to generate electrical power within the fuel cell. This kind of fuel cell is represented in figure 3.
Here, the most important part is named membrane electrode assembly (MEA), consisting of the electrocatalyst and the membrane. During the first step, the electrochemical reactions take place, while the membrane allows the conduction of produced protons from the anode to the cathode.
At the anode, the reaction can be resumed as follows:

$$H_2 \rightarrow 2H^+ + 2e^- \qquad (1)$$

Typically, if the reaction is driven in an acid medium, O_2 can be reduced to H_2O via two pathways; direct 4 e^- pathway which requires the transfer of 4 e^- and $4H^+$ (equation (1)), or 2+2 e^- pathway, in which the oxygen is reduced to hydrogen peroxide, which is further reduced to water (equations (3)-(5)). [5]

$$O_2 + 4H^+ + 4e^- \rightarrow 2H_2O \qquad (2)$$

$$O_2 + 2H^+ + 2e^- \rightarrow H_2O_2 \qquad (3)$$

$$H_2O_2 + 2H^+ + 2e^- \rightarrow 2H_2O \qquad (4)$$

$$2H_2O_2 \rightarrow 2H_2O + O_2 \qquad (5)$$

On the other hand, if driven in alkaline medium, we can also have a direct pathway (equation (6)) or a two steps pathway (equations (7)-(9)). In both cases we have the OH^- formation:

$$O_2 + 2H_2O + 4e^- \rightarrow 4OH^- \qquad (6)$$

$$O_2 + 2H_2O + 2e^- \rightarrow 4HO_2^- + OH^- \qquad (7)$$

$$HO_2^- + H_2O + 2e^- \rightarrow 3OH^- \qquad (8)$$

$$HO_2^- \rightarrow 2OH^- + O_2 \qquad (9)$$

However, as already mentioned before, hydrogen peroxide (H_2O_2)- which is extremely likely to be formed because of the lack of active sites for $O-O$ bond scission when catalysing the ORR of SACs- and peroxide species (OOH^-) could be generated via 2 e^- pathway in acid or alkaline media respectively. [6]
Furthermore, the hydrogen peroxide could react with some leached metal ions, leading to the onset of Fenton/Fenton-like reactions, resulting in the formation of highly reactive radicals (i.e., $OH\bullet$, $HO_2\bullet$). These radicals are very dangerous since they could react with the carbon support, damaging the active sites etc.
Then, as a first observation, we can conclude that a good catalyst should not promote the 2+2 e^- pathway.

From a thermodynamic perspective, an ideal ORR should have a free energy drop of -1.23 eV for each step. However, in real cases we have some energy loss due to the formation of intermediates in each step, which result in an overpotential that will reduce the potential output of the fuel cell. Those losses can be collectively generalised as polarisation. [7]

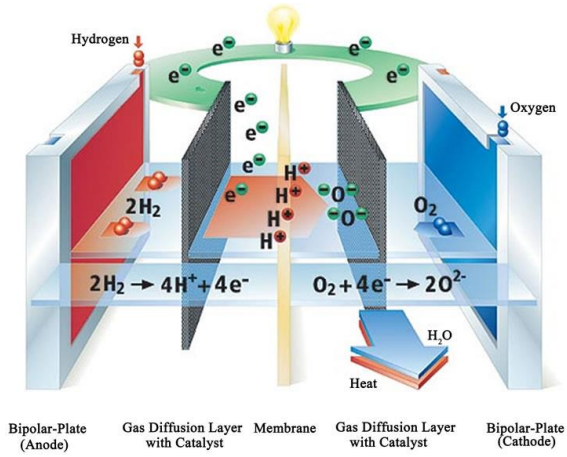

Figure 3. *PEMFC design.* [7]

1.2. The Faraday's law and the Butler-Volmer Equation

Generally speaking, to evaluate the rate of an electrochemical reaction and thus the feasibility and the production rate, the Faraday's law is used. [8]
For this purpose, it must be taken into account the activation energy barrier that the charge has to overcome in order to freely move from the liquid electrolyte to the solid electrode and/or vice versa; this quantity is typically described by the electrical current- more precisely a current density (charge per unit area of the surface).
The latter, expressed with "i" takes into account the charge transferred, the surface area, and the reactant consumptions, and it is expressed by the Faraday's law:

$$i = nFv \qquad (10)$$

The current density is directly related to the reaction rate through Faraday's constant (F), which represents the charge transferred per mole of electrons (96485 C/mol). The product of F and the number of electrons transferred per reaction (n) signifies the net charge transferred per mole of reactant (nF). v represents the consumed reactants, expressed as $^{mol}/_{s\ cm^2}$. Since this is a net current density, it is already the difference between the forward and the reverse current densities on the electrode; thus, it can be written as follows:

$$i = nF(k_f C_{Ox} - k_b C_{Rd}) \qquad (11)$$

where k_f is the forward reaction rate constant (s^{-1}), C_{Ox} is the surface concentration of the reacting species (mol/cm^{-2}), k_b is the reverse reaction rate constant (s^{-1}), and C_{Rd} is the surface concentration of the reacting species (mol/cm^{-2}). O_x stands for the oxidised form of the reactant and R_d stands for the reduced form of the reactant. [8]
It is worth underlining that at electrochemical equilibrium, the net current flowing through the electrode becomes zero. This does not signify the complete cessation of both forward and backward

reactions. In fact, both reactions continue to occur simultaneously but at precisely equal rates. The rate at which these reactions proceed under equilibrium conditions is referred to as the exchange current density, denoted by i_0.

$$i_0 = nFk_f C_{Ox} = nFk_b C_{Rd} \qquad (12)$$

With that being said, it is straightforward to state that the magnitude of the exchange current density (i_0) is intrinsically linked to the kinetics of the electrode reaction; thus, a sluggish reaction, characterised by a low exchange current density, needs a larger overpotential to achieve a desired current density compared to a faster reaction with a high exchange current density. In simpler terms, electrodes facilitating faster electron transfer reactions (higher i_0) require a lower overpotential to generate a specific current density. [8]

The other important equation in electrochemistry is the *Butler-Volmer* equation which focuses on the kinetics of electrode reactions.
In practical terms, it describes the relationship between the current density (current per unit area) at an electrode and the potential difference applied to it.
The equation itself can be obtained introducing the relationships among the reaction rate constants (introduced in the previous equations) and the Gibbs free energy, and the transfer coefficient (α), whose value is between 0 and 1- and typically it is 0.5 for reactions occurring on a metallic surface. The relationship between the two transfer coefficient is:

$$\alpha_{Rd} + \alpha_{Ox} = 1 \qquad (13)$$

skipping the intermediate steps, the forward reduction and the backward oxidation reaction rate constants are expressed as follows:

$$k_f = k_{0,f} \exp\left[\frac{-\alpha_{Rd} nFE}{RT}\right] \qquad (14)$$

$$k_b = k_{0,b} \exp\left[\frac{-\alpha_{Ox} nFE}{RT}\right] \qquad (15)$$

Where E is the potential, R is the universal gas constant, and T is the temperature, while $k_{0,f}$ and $k_{0,b}$ are the standard rate constants for the forward and backward reactions respectively- in other words the rate constant when the two electrodes are at thermodynamic standard potential.
Putting equations (13), (14), and (15) in the equation (11) it is possible to reformulate the current density as:

$$i = nF\left[k_{0,f} C_{Ox} \exp\left(\frac{-\alpha_{Rd} nFE}{RT}\right) - k_{0,b} C_{Rd} \exp\left(\frac{(1-\alpha_{Rd}) nFE}{RT}\right)\right] \qquad (16)$$

While at the equilibrium we have:

$$i_0 = nFk_{0,f} C_{Ox}^b \exp\left(\frac{-\alpha_{Rd} nFE_{eq}}{RT}\right) = nFk_{0,b} C_{Rd}^b \exp\left(\frac{(1-\alpha_{Rd}) nFE_{eq}}{RT}\right)] \qquad (17)$$

In which is possible to identify the E_{eq} as the reversible (or equilibrium potential), C_{Ox}^b and C_{Rd}^b as the bulk concentration of reacting species (expressed as mol/cm^2).
Is it straightforward to reformulate the current density as a function of i_0. Additionally, by

identifying α_{Rd} as α, and $(E - E_{eq}) = \eta$ -the overpotential so that for the anode reaction $\eta_a = E_a - E_{eq} > 0$, while for the cathode reaction $\eta_c = E_c - E_{eq} < 0$ -and assuming $C_{Ox}^b = C_{Ox}$ and $C_{Rd}^b = C_{Rd}$, we can finally type the *Butler-Volmer equation*:

$$i = i_0[\exp\left(\frac{-\alpha n F \eta}{RT}\right) - \exp\left(\frac{(1-\alpha) n F \eta}{RT}\right)] \quad (18)$$

To obtain the operative equations used in the fuel cell measurements,

$$i_a = i_{0,H_2}[\exp\left(\frac{-\alpha_H n_{\alpha,H} F \eta_a}{RT}\right) - \exp\left(\frac{(1-\alpha_H) n_{\alpha,H} F \eta_a}{RT}\right)] \quad (19)$$

$$i_c = i_{0,O_2}[\exp\left(\frac{-\alpha_O n_{\alpha,O} F \eta_c}{RT}\right) - \exp\left(\frac{(1-\alpha_O) n_{\alpha,O} F \eta_c}{RT}\right)] \quad (20)$$

Where:

- i_c = the cathodic current density
- i_a= the anodic current density
- i_{0,O_2} = the apparent exchange current density for cathodic O2 reduction
- i_{0,H_2} = the apparent exchange current density for the anodic H2 oxidation reaction
- R = the universal gas constant (8.314 J / $mol\ K$)
- T = the temperature (K).
- F = Faraday constant (96485 C/mol)
- $n_{\alpha,O}$ = the electron transfer number in the rate determining step for cathodic O_2 reduction
- $n_{\alpha,H}$ = the electron transfer number in the rate determining step for anodic H_2 oxidation
- α_O = the transfer coefficient in the rate determining step for cathodic O_2 reduction (α_O=$\alpha_{O,Rd}$)
- α_H = the transfer coefficient in the rate determining step for anodic H_2 oxidation (α_H=$\alpha_{H,Rd}$)

1.3. Three electrode systems and rotating disk electrode

In this thesis work, the electrochemical performances of the synthesised catalysts have been carried out using three-electrode cells configuration and, more in detail, the rotating disk electrode system. [8]

The three-electrode setup is the standard one and provides information about the overall electrochemical activity at the working electrode.
As the word itself suggests, it consists of three electrodes:

1. **Working electrode (WE)**: The electrode where the main electrochemical reaction of interest takes place. In PEMFC research, the WE typically consists of a catalyst-coated electrode whose performance are going to be tested. It is typically deposited on a rotating disk electrode (RDE) made from a conductive yet inert material like glassy carbon or Teflon.
2. **Counter electrode (CE)**: Provides the current to balance the reaction at the working electrode. In other terms it acts as a current sink: As the WE drives the ORR and generates current, the CE takes up an equal amount of current but in the opposite direction, completing the electrical circuit within the cell. Material choice is not crucial as long as it conducts

electricity and doesn't interfere with the reactions at WE or RE.

3. **Reference electrode (RE):** This provides and maintains a stable and well-defined potential throughout the experiment. It serves as a reference point for measuring the potential applied to the WE.

The rotating disk electrode is privileged since, as the reaction proceeds, oxygen molecules near the electrode surface are depleted. This creates concentration gradients that can limit the reaction rate. The RDE elegantly solves this problem thanks to its spinning at controlled set speed: this rotation disrupts the stagnant layer of electrolyte near the electrode surface, constantly bringing fresh solution containing oxygen. This ensures a uniform concentration of reactant at the interface.
Among the measurements done with those electrodes, two key techniques reign supreme: Cyclic Voltammetry (CV) and Linear Sweep Voltammetry (LSV). [8]

Cyclic voltammetry (CV) stands as a widely employed electroanalytical technique for investigating the intricacies of electrochemical reactions and their kinetics. This versatile technique offers valuable insights into various aspects of electrocatalysis, including:

- **Redox Behaviour:** CV measurements reveal the redox behaviour of electroactive materials, providing information on their ability to undergo oxidation and reduction reactions.
- **Electron Transfer Kinetics:** The technique sheds light on the kinetics of heterogeneous electron transfer reactions, which govern the rate of electron exchange between the electrode and the electrolyte.
- **Coupled Processes:** CV can identify instances where chemical reactions are coupled to electron transfer, providing a more comprehensive picture of the overall process.
- **Adsorption Phenomena:** The technique is adept at elucidating the adsorption of molecules onto the electrode surface, a crucial aspect in many electrocatalytic reactions.

During a typical CV experiment, a working electrode remains stationary within an unstirred solution. The potential applied to this electrode is ramped linearly at a constant scan rate. The resulting current, a consequence of electron transfer at active reaction sites, is plotted against the applied potential, generating a characteristic cyclic voltammogram.
By analysing the CV profiles of catalysts in acidic or alkaline electrolytes, researchers can gather information about the adsorption/desorption of oxygen species on the catalyst surface. The presence of distinct peaks at lower potentials often signifies these phenomena. Similarly, peaks observed at higher potentials during the forward and backward scans can be attributed to the oxidation and reduction of oxygen species, respectively.
The wealth of information extracted from CV profiles empowers researchers to evaluate key parameters of electrocatalysts. These parameters include the electrochemically active surface area (ECSA), the reduction peak potential, and the current associated with the reaction, all of which contribute to assessing the catalyst's performance, particularly for the oxygen reduction reaction (ORR).

On the other hand, linear sweep voltammetry (LSV) is also employed as a key technique to investigate the electrochemical behaviour of the target species. LSV involves applying a potential sweep in a single direction, either anodic or cathodic, allowing for the analysis of redox processes. Compared to cyclic voltammetry (CV), LSV offers a simpler approach for studying electron transfer kinetics and mass transport phenomena at the electrode-electrolyte interface. The LSV profiles provide valuable insights into the rate-determining factors of the electrochemical reactions, including electron transfer rate, reactant reactivity, and potential scan rate. Through analysis of LSV data, parameters such as limiting current density, kinetic current density, and mass and specific activities can be extracted, enabling the determination of the oxygen reduction reaction (ORR) kinetics. Furthermore, hydrodynamic LSV experiments performed at varying electrode rotation speeds can be employed

alongside the Koutecky-Levich equation, in this work defined as equation (27), to elucidate mass transfer effects across the electrode surface. Ultimately, LSV analysis under controlled conditions facilitates a precise evaluation of the actual electrocatalytic performance of the material.

Additionally, another common measurement typically done is the Electrochemical impedance spectroscopy (EIS). [9]
This is a powerful electroanalytical technique employed to better analyse the electron transfer mechanisms occurring at the electrode-electrolyte interface during electrochemical reactions. This technique offers valuable insights into the chemical transformations involved, enabling the extraction of mechanistic and kinetic information from electrode materials.
The significance of EIS lies in its ability to probe the intrinsic properties of catalyst materials that govern their conductivity, a critical factor influencing fuel cell efficiency. The underlying theory of EIS suggests that several factors influence the electrochemical behaviour of catalysts, which are reflected in the measured impedance:

1. ohmic resistance, representing the ease of ion or electron movement,
2. double-layer capacitance, indicative of the kinetic limitations at the interface
3. charge transfer resistance or polarisation resistance, which reflects the rate of mass transfer processes.

The test operates by applying a small sinusoidal AC (alternating current) perturbation, either voltage or current, to the cell. The system's response to this perturbation is measured by recording the amplitude and phase shift of the resulting AC signal across a range of frequencies. In essence, EIS measures the impedance, which quantifies the opposition a material offers to the flow of the constantly changing AC current.

The collected EIS data is typically analysed using two graphical representations: Bode plots and Nyquist plots. A Bode plot displays both the magnitude (absolute value) and phase angle of the impedance as functions of frequency. This allows for visualisation of how the impedance changes with varying frequencies. Conversely, a Nyquist plot presents the imaginary component of the impedance plotted against the real component for each measured frequency. This graphical format provides insights into the different processes contributing to the overall impedance.

EIS data can be further interpreted using equivalent circuit models that represent the various electrochemical processes occurring within the fuel cell. A simple equivalent circuit for a typical Nyquist plot with two arcs (Figure 4) can be depicted as shown in Figure 5. The high-frequency intercept of the Nyquist plot corresponds to the ohmic resistance (R_Ω) of the fuel cell stack. This value can be directly compared with measurements obtained from separate current interrupt experiments for verification.
The high-frequency arc in the Nyquist plot reflects the combined effects of the double-layer capacitance in the catalyst layer and the charge transfer resistance. This arc highlights the limitations associated with the initial stages of the electrochemical reaction at the electrode surface. The low-frequency arc, on the other hand, corresponds to the impedance arising from mass transport limitations. These limitations can be caused by the slow diffusion of reactants and products within the porous electrode structure.

The use of a constant phase element (CPE) instead of a simple capacitor (C) in the equivalent circuit model acknowledges the non-ideal behaviour of the double-layer capacitance. This deviation from ideal capacitance arises due to the distributed nature of the electrical double layer within the porous structure of the catalyst layer.

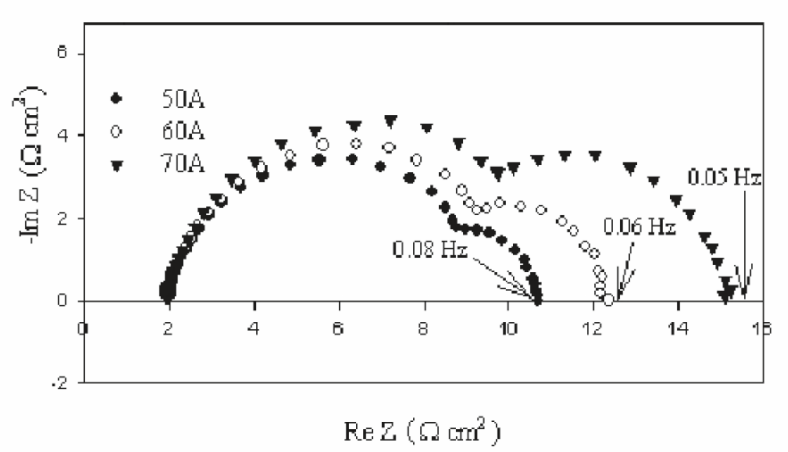

Figure 4. *Typical impedance spectra of a PEM fuel cell.* [10]

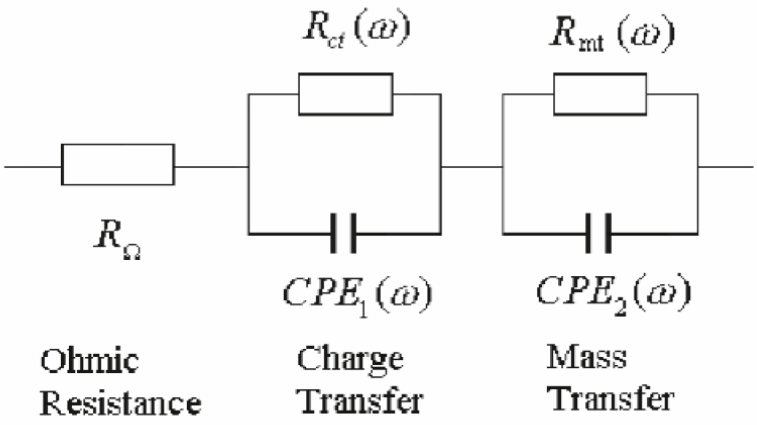

Figure 5. *Simple equivalent circuit for the spectra in Figure 4.* [10]

Stepping back to the Koutecky–Levich equation, one can combine the measured current (i_m) with the kinetic current from the electrochemical reactions (i_K) and the mass transport current (i_{MT}). [10]

$$\frac{1}{i_m} = \frac{1}{i_K} + \frac{1}{i_{MT}} \tag{21}$$

The kinetic current can be modelled by the Butler-Volmer equation described before and, in the case of a rotating disk electrode setup, the mass transport current term can be expressed through the Levich equation, which reads as follow:

$$i_{MT} = B_L \omega^{\frac{1}{2}} \tag{22}$$

Where ω is the angular rotation rate of the electrode, expressed as (rad/s), andB_L is the Levich constant, further expressed as:

$$B_L = 0.62nFAD_{O_2}^{\frac{2}{3}} v^{-\frac{1}{6}} C_{O_2} \tag{23}$$

- n = number of the electron transferred during the oxygen reduction,
- F = Faraday constant (96485 $C\ mol^{-1}$),
- D_{O_2}= diffusion coefficient of the oxygen in the electrolyte,
- v = electrolyte kinematic viscosity ($cm^2\ s^{-1}$),
- C_{O_2}= concentration of the oxygen in the electrolyte ($mol\ cm^{-1}$).

1.4. Single atom catalysts (SACs)

Going deeply into details, the SACs have emerged as a fascinating field of study in heterogeneous catalysis. Unlike traditional catalysts composed of metal nanoparticles or clusters, SACs consist of isolated metal atoms dispersed on a support material. This unique structure, with an abundance of robust active sites, gives rise to exceptional catalytic properties, such as high activity, selectivity, and stability. a scheme of their applications is reported in the following figure 6. [11]

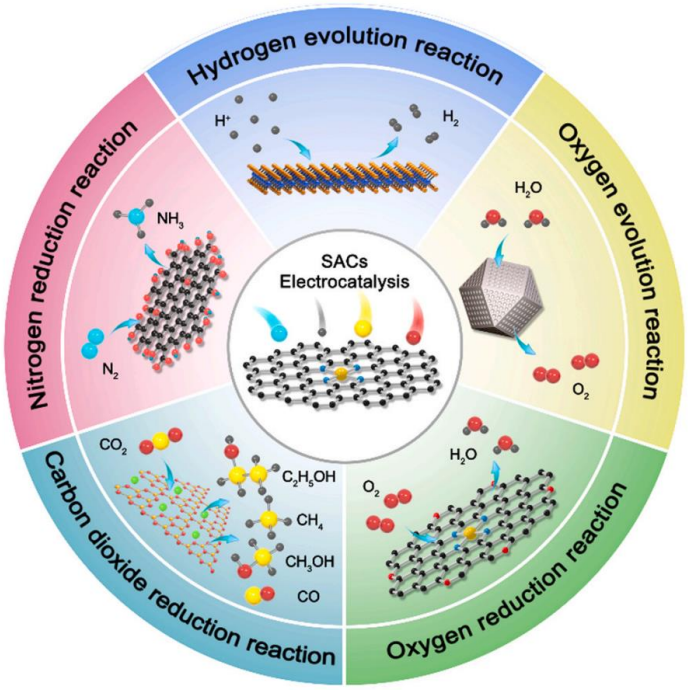

Figure 6. *Schematic illustration of the SACs for electrocatalysis.* [11]

The metal host material, and its coordination environment with adjacent atoms, play a decisive role in determining the electronic structure of SAC. Generally, there is a strong ionic or covalent bondage in order to firmly anchor the single atoms, which can induce significant charge transfer which further modifies the active sites.
Tuning the electronic structures formed by such strong atom-support interactions can improve their overall catalytic performance: the unsaturated coordination environments of those kind of catalysts let reactants adsorb and activate on catalytic sites, thus lowering the energy barrier of electrocatalytic

processes.
In catalysis, having a sufficiently high number of active centres, as well as the possibility of easily adjust the electronic structure- which provides the energy needed to activate the adsorbed molecules- are crucial for reactant and catalytic reactions. [11]
Single-atom metals are typically dispersed on the support surface by using a precursor which decomposes, leading to the generation of individual atoms, which subsequently diffuse and bind to the support surface.
The choice of the suitable host material is really important, since its defects and local environment play a decisive role in forming active sites with the metal atoms and have direct influence on the physical and electronic properties of the catalyst.
Carbon-based one are extensively used, due to their high specific surface area, high pore volume, and tunable porous structure.
The choice of mesoporous carbons, a class of engineered carbon materials with a network of interconnected pores ranging from 2-50 nanometers in diameter, is well justified for several reasons. This unique pore structure offers several advantages for PEMFC and CO_2 electrolyser applications:

- **High surface area:** The extensive network of pores provides a large platform for dispersing catalyst materials, maximising their utilisation and enhancing reaction efficiency.
- **Tunable pore size:** The size of the pores can be precisely controlled during synthesis, allowing for the optimisation of mass transport within the cathode. This ensures efficient delivery of reactants (O_2/ CO_2) and removal of products (H_2O, etc.) from the catalyst sites.
- **Chemical stability:** Mesoporous carbons exhibit excellent chemical stability in the acid/alkaline environment of PEMFCs, ensuring their long-term durability. [12]

Nevertheless, the synergy among mesoporous carbons and SACs holds immense promise for overcoming the limitations of traditional PEMFC catalysts due to the high activity and selectivity**:** the large surface area and well-defined pore structure of mesoporous carbons, coupled with the high activity and tunability of SACs, can lead to significantly enhanced ORR activity and improved selectivity towards the four-electron pathway, maximising fuel cell efficiency.
Secondly, we have an improved mass transport: the controlled pore size of mesoporous carbons facilitates efficient mass transport of reactants and products within the cathode, ensuring optimal utilisation of the SACs. [2]
Additionally, they are characterised by durability and cost benefits, since the stability of both mesoporous carbons and SACs contributes to the long-term durability of PEMFCs. Additionally, SACs offer the potential for using less expensive metals compared to Pt, reducing overall catalyst costs.
Another important aspect is that the catalytic efficiency is generally increased with nitrogen-functionalised carbon.
It has been shown the nitrogen atoms not only acts as the anchoring sites to stabilise the single metal atoms, but the coordination number x of those active sites (generally indicated with $M-N_x$) affects its catalytic function by tuning the charge distribution of the active sites themselves.
The F_e-N_x active sites of F_e-N-C could theoretically have five coordination numbers x= 2-6; the F_e-N_4 one is known to show the best ORR activity, but the relative ORR activities and PEMFC performances of other types of F_e-N_x active sites remain unclear and are still under debate.
As an example, several configurations are represented in figure 7 where the grey, red, and blue balls represent carbon, iron, and nitrogen, respectively.

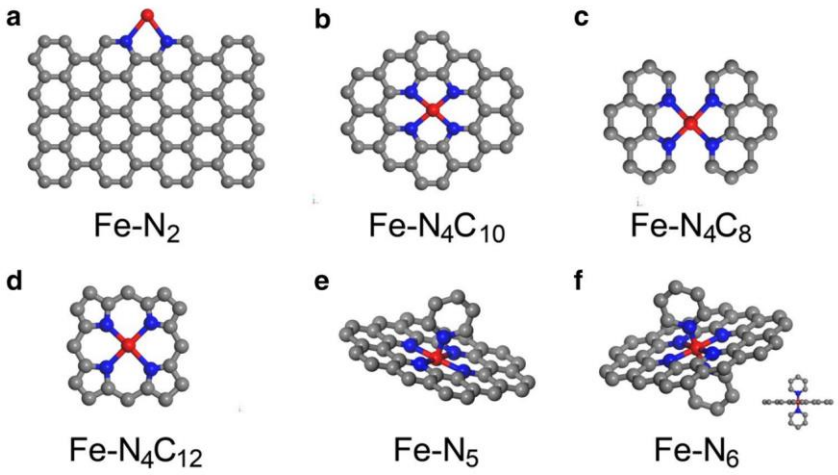

Figure 7. *Atomic structure of Fe-N-C sites with different coordination environment supported on graphene.* [2]

1.5. Mesoporous carbons SACs-based materials

There exist different pathways to synthesise single atom catalysts. Among all the synthesis methods available for their preparation -and the one chosen for this project- the hard-templating (or nanocasting) approach is one of the most attractive, since it allows a variety of achievable morphology and porosity of the materials. Through this technique it is possible to produce highly ordered non-siliceous mesoporous materials with high specific surface area and narrow pore distribution, typically starting from ordered mesoporous silica -such as SBA-15, KIT-6, etc. [13]
It consists of four main steps, and can be schematically represented as in figure 8:

1. Choice and synthesis of the original template, also called sacrificial template since it will be removed afterwards.
2. Choice of a suitable precursor salt for the final catalyst's impregnation in the template pores.
3. Thermal treatment (usually pyrolysis) which leads both to the decomposition of the precursor and its rearrangement to form the desired structure and to the silica template removal.
4. Selective removal of the remaining silica matrix by chemical etching and heat treatment.

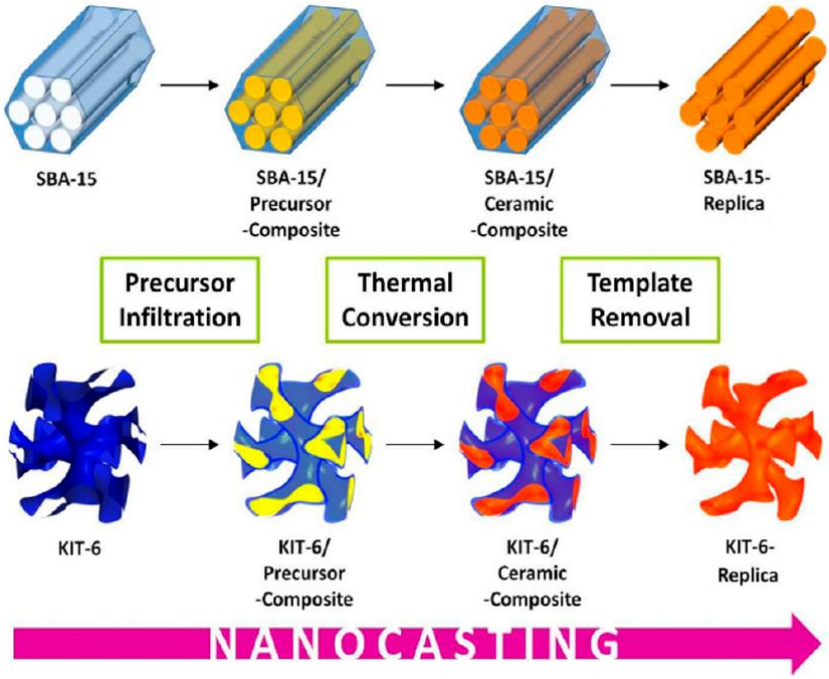

Figure 8. *Scheme of the nanocasting procedure for ordered mesoporous non-silica materials.* [14]

Thanks to this technique, it is possible to generate very ordered and porous materials, without the necessity of constantly controlling the PH, the hydrolysis-condensation processes, and other parameters difficult to manage typical of the other synthesis methods.
The sacrificial template pores are filled due to the precursors migration into the porous system via capillary motion and then, through the thermal treatment, we have its rearrangement into ordered structures.
On the other hand, a different approach is followed to create the silica templates, for instance a soft-template technique. [14]
The latter involves the usage of amphiphilic molecules, like surfactants or amphiphilic block copolymers, to create the desired pores shape, and a silica precursor to have the final mesoporous silica product.
When dissolved in the appropriate solvent, the micellar structures formation take place, but when the surfactant concentration increases more, the lyotropic liquid crystals (LLC) appear. Those crystals, like the micelles, are self-assembled structures formed by amphiphilic molecules, but they differ in terms of their structures, phase transitions, applications, and shapes -in the present case hexagonal and cubic.
The LLC phases contain long-range spatially periodic nanostructures with lattice parameters in the range of 2–15 nm. The mesostructure of the LLCs formed strongly depend on the molecular structure, concentration, and temperature. [15]
This lyotropic liquid-crystalline phase leads to the assembly of an ordered mesostructured composite during the condensation with the silica precursors. The mesoporous materials are obtained by subsequent removal of the surfactant by solvent extraction and/or calcination, as can be seen in figure 9.

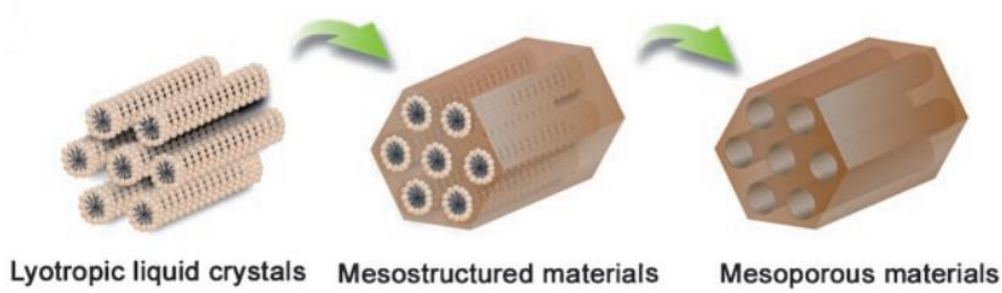

Figure 9. *Synthetic procedure for the soft-template process for the preparation of SBA-15 mesoporous silica.* [15]

SBA-16 and KIT-6 mesoporous silicas have been chosen as hard templates due to their textural properties, which will be reflected by the final electrocatalysts, like high surface area (550-750 m^2/g), pore size (7-9 nm), and pore volume (0.9-1.3 cm^3/g) [15]. All of them are essential features for the final electrocatalysts for several reasons:

1. Enhanced accessibility: high surface areas and pore volumes provide a larger space which can be filled with the carbon-metal sources. Furthermore, the higher the contact area between the catalyst and the reactant molecule, the higher the reaction possibilities. This also allows a better diffusion of reactants into the catalyst, increasing the chances of catalytic reactions and improving the overall catalytic efficiency.
2. Improved stability: thanks to their intrinsic pore arrangement - three-dimensional (3D) cubic mesostructure with pores arranged in a body-centred cubic (BCC) lattice for KIT-6, and a main two-dimensional (2D) hexagonal mesostructure with pores in a hexagonal lattice interconnected by a small fraction of micropores for SBA-15 – the final structure will not collapse, yet it will be stable. A simple representation is presented in figure 6.
3. Tunable properties: The surface area, pore volume, and mesoporosity can be controlled during synthesis, allowing for the optimisation of the final catalyst's properties. By adjusting these parameters, it is possible to tailor the size, shape, and distribution of the mesopores, which directly influence the transport of reactants and products within the catalyst, enabling the customisation of the single atom catalyst for specific reactions and promoting selectivity, efficiency, and stability.

Objectives and perspectives

This MSc project aims to develop high surface area Single Atom Catalysts (SACs) tailored for selective Oxygen Reduction Reaction (ORR). This involves designing mesoporous carbon-based SACs through a nanocasting approach. The project is structured around three main Tasks:

1. Synthesis of mesoporous carbon-based SACs involves incorporating 1,10 phenanthroline and $Fe(NO_3).9H_2O$ salt precursors, as carbon-nitrogen and metal sources, respectively, into three types of silicas: SBA-15, KIT-6, and a hybrid silica combining a 2D-hexagonal and 3D cubic arrangement of pores. This aims to investigate the influence of porosity on the catalytic activity of the materials.
2. Characterisation of the materials using techniques such as X-ray powder diffraction (PXRD), Scanning Transmission Electron Microscopy (STEM), elemental analysis, Brunauer-Emmett-Teller Analysis (BET), and thermogravimetric analysis (TGA). This aims to understand the microstructure relationship between synthesis conditions and catalytic activity.
3. Investigation of the electrochemical activity of the SACs using the Rotating Disk Electrode (RDE) with different electrolyte solutions.

Through these objectives, the aim is to contribute to the development of SACs for selective ORR. The outcomes of this study hold promise for advancing ORR technology and can potentially be extended to CO_2RR (CO_2 reduction reaction), NRR (nitrogen reduction reaction), and so on by varying the metal source. This research offers potential solutions for effective carbon dioxide mitigation. [2]

2. Materials and methods

2.1. Chemicals

Poly(ethylene glycol)-block-poly(propylene glycol)-block-(ethylene glycol) (average Mn≈5800), iron(III) nitrate nonahydrate (purity ≥ 98.0%), tetraethyl orthosilicate (purity ≥ 98.0%), 1-butanol (purity ≥ 99.4%), 1,10-Phenanthroline (purity ≥99.0%) were purchased from Sigma-Aldrich (USA). Ethyl alcohol (purity ≥ 99.8%), hydrochloric acid (37 wt. %), sodium hydroxide pellets (purity 98% up to 100.5%), and isopropanol (IPA, purity ≥ 99.9%) have been purchased from Honeywell (USA).

2.2. Material synthesis

In the present section, the synthesis procedures of both mesoporous silicas hard-templates, and electrocatalysts will be shown in detail.

2.2.1. Mesoporous silica synthesis

In this project, four types of mesoporous silica have been synthesised: KIT-6 (Korea Advanced Institute of Science and Technology-6), SBA-15 (Santa Barbara Amorphous type materials-15), a silica with hexagonal arrangement from a KIT-6 protocol, and a bimodal silica with both mesopores and nanopores.
In order to achieve this objective, three different protocols related to KIT-6 have been used to obtain 3 distinct pore organisation: 2D-hexagonal arrangement, mixed 2D-hexagonal arrangement/3-D cubic structure, and 3D-cubic structure.
On the other hand, the classic SBA-15 silica protocol was used to obtain the 2D-hexagonal arrangement of the pores.

- protocol a. KIT-6 derived 2D-hexagonal arrangement silica (KIT-6-*p6mm)*

This material synthesis has been carried out based on the classic route from Freddy Kleitz at al. following this components mole ratio [16]:

TEOS : P123 : HCl : H2O : BuOH = 1 : 0.017 : 1.83 : 195 : 1.31

The given amounts were scaled down in order to fit into a 200 mL reactor.
More precisely, 4.836 g of Pluronic P123 was completely dissolved in 175 g of distilled water and 9.516 g of concentrated HCl (37%). To this, 4.84 g of 1-butanol was added, and the mixture was left under rigorous stirring at 35 °C for 1 hour in an open beaker. Finally, 10.408 g of TEOS silica source was added dropwise and this mixture was left under stirring for 24 hours at the same temperature.
In order to obtain a material with 2D hexagonal pores, the reaction vessel was kept unsealed in order to allow the simultaneous evaporation of 1-butanol and HCl, since the decisive role to obtain a cubic mesophase is played by the butanol.
After this amount of time, it was transferred in a closed Teflon reactor and thermally treated at 100 °C for other 24 hours in an oven under static conditions, then filtered hot without washing and dried overnight at the same temperature. The Pluronic template was removed by solvent extraction in a flask and with a condenser on top to avoid evaporation losses as showed in figure 10, using 7.5 mL of HCl (37%) and 500 mL of ethanol at 80°C followed by calcination in a muffle at 550 °C for 5 hours.
The final sample is labelled as “KIT-6-*p6mm*”.

Figure 10. *Solvent extraction with a condenser on top.*

- Protocol b. KIT-6 derived mixed 2D-hexagonal arrangements/3-D cubic structure silica (KIT-6-*dual)*

The hard-templates synthesis route proceeded with a dual mesoporous silica, still following the Kleitz's protocol, keeping the same quantities and procedures -except for the reaction vessel which remained sealed. If during the first synthesis the importance of butanol was seen, in the present one the role of the acid environment was used, as can be notice from the work of Tae-Wan Kim et al. [17] The final material named KIT-6-*dual* shows some peculiar and very interesting properties, which can be classified as the midway between KIT-6 and SBA-15 textural properties.

- protocol c. KIT-6 derived 3D-cubic structure (KIT-6)

Finally, a KIT-6 silica with cubic $Ia\bar{3}d$ phase has been synthesised following the Tae-Wan Kim et al. protocol. [17]
In order to achieve this crystallinity, a range of 0.25-0.75 M HCl gives high yields of highly ordered cubic mesoporous silica, close to 100% on the basis of silica recovery.
Considering all the possible variables and their contribution, for the synthesis it was chosen the following material molar ratio:

TEOS : P123 : HCl : H2O : BuOH = 1.5 : 0.017 : 1.83 : 195 : 1.7

Scaling the quantities for a 200 mL reactor, it led to the usage of: 6 g of Pluronic P123, 144 g of H_2O, 7.47 g of HCl 37%, 5.17 g of 1-BuOH, and 12.8 g of TEOS, while the hydrothermal treatment was carried at 373 K.
With the indicated amount it was possible to synthesise a silica with cubic $Ia\bar{3}d$ phase and all the typical properties of the KIT-6.

- Protocol d. SBA-15 derived 2D-hexagonal structure (SBA-15)

Concerning the SBA-15, the synthesis was developed based on the work of Guillet-Nicolas et al. [18]
The preparation pathway of this silica is very similar to the previous one for KIT-6; however, some differences are crucial to obtain such a material.
More precisely, it was used an aqueous solution of Pluronic P123 triblock copolymer (EO20PO70EO20, MW=5800, Sigma-Aldrich) and hydrochloric acid (HCl, 37.5%), and tetraethoxysilane (TEOS, Sigma-Aldrich 98%) as the silica source.
The molar composition of the reaction mixture was:

TEOS : P123 : HCl : H2O = 1 : 0.022 : 0.7 : 130

In terms of mass weight and procedure, 8.0 g of Pluronic P123 was dissolved in 146.25 g of distilled water and 4.43 g of HCl (37%) under vigorous stirring. After complete dissolution, 13.0 g of TEOS was added at once to the homogeneous clear solution. This mixture was further left under stirring at T = 35 °C for 24 hours at almost 1000 rpm, since it was a very viscous solution. Then, the synthesis mixture was placed in an oven at 80 °C for another 24 hours under static conditions.
Afterward, the mixture was dried at 140 °C overnight. For template removal, the as-synthesised silica powders were first shortly slurred in an ethanol/HCl mixture at 80 °C- same KIT-6 described procedure- and subsequently calcined at 550 °C for 5 hours.
This synthesis method offers some advantages over other procedures reported for the preparation of SBA-15, as these conditions allow excellent reproducibility, very high structural order, mesophase purity, and easy scale-up.
The final powder, identified as SBA-15, and is a highly ordered mesoporous SBA-15.

2.2.2. Electrocatalyst synthesis

Electrocatalyst synthesis utilises various techniques that share some common principles. These principles include the initial mixing of precursor materials, followed by a high-temperature treatment (pyrolysis) and a subsequent etching steps (alkali and acidic washing). [19]
Compounds with a high nitrogen to carbon atomic ratio (N:C) are highly desirable as carbon sources. Examples include nicarbazin, 1,10-phenanthroline, etc. These precursors enable the incorporation of a high density of active sites within the final electrocatalyst structure due to the abundance of nitrogen atoms.
Pyrolysis plays an important role in shaping the final electrocatalyst structure. This process, conducted at elevated temperatures (typically 700-1100°C), provides the necessary energy needed to rearrange and form new chemical bonds within the precursor mixture through thermochemical decomposition under the presence of inert gases (Figure 11). By carefully controlling variables such as the heating rate (ramp rate), final temperature, and the gas composition used during pyrolysis, it is possible to fine-tune the final characteristics of the electrocatalyst. Studies in the literature [19] have shown that a slower ramp rate (around 5-10°C/min) can maximise the material's pore volume. Selecting the optimal final temperature is relevant to prevent the undesirable agglomeration of metal particles and excessive graphitisation.
Following pyrolysis, an acid washing step is often employed prepare SACs. This step removes electrochemically undesirable metal-containing compounds, such as weekly bonded metal or metal oxide nanoparticles, remaining primarily the coordinated metals. These unwanted components contribute mass without enhancing activity and are typically eliminated using hydrochloric acid (HCl) or sulfuric acid (H_2SO_4) solutions. [20]

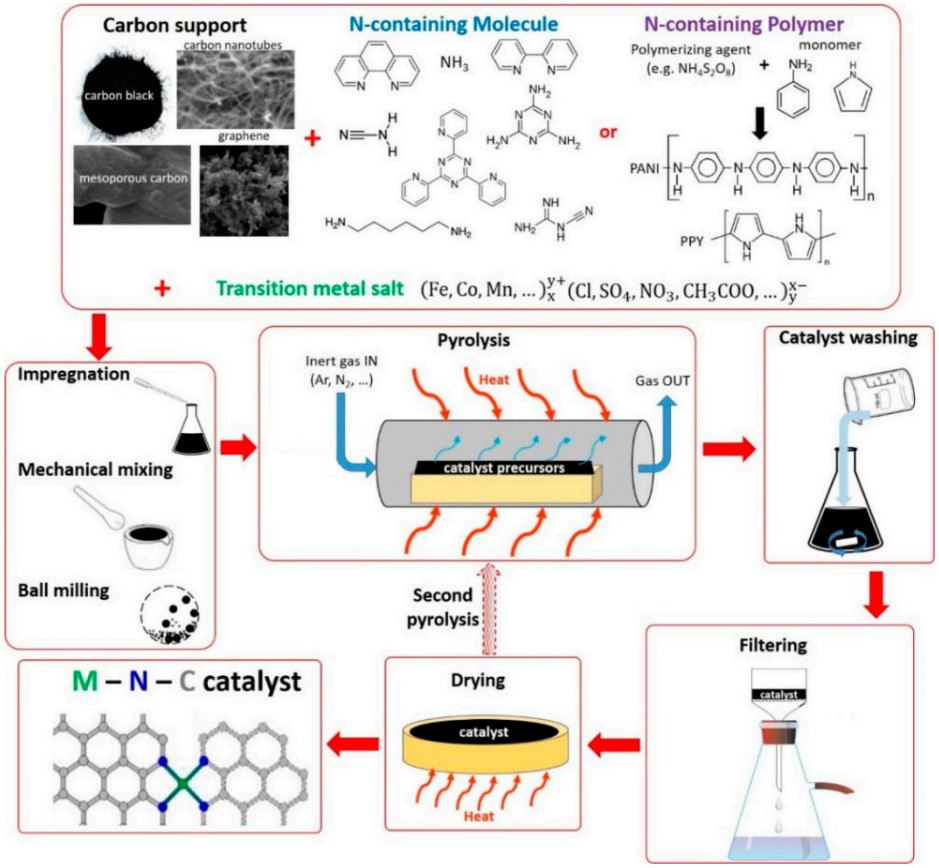

Figure 11. *Scheme representing the typical steps for M–N–C catalysts synthesis with nanocasting approach.* [19]

In the present work, the ORR catalysts syntheses were conducted following the protocol from *Yu Xiong* et al. [21], using 1,10-phenanthroline as carbon source and iron(III) nitrate nonahydrate as metal precursor.
The latter has been mainly chosen for three reasons:

1. it is highly soluble in water/ethanol mixture, which makes it easy to incorporate into the reaction mixture during catalyst synthesis,
2. the nitrate is easily removed; thus, the iron ions are effortlessly available,
3. for its commercially availability: Iron(III) nitrate nonahydrate is a relatively inexpensive, which means a readily available iron source.

❖ Protocol 1. Studying the influence of the silica support on the mesoporous carbon structure: synthesis of 1a_Fe@N-CMK-8, 1b_Fe-N@CMK-3/8, and 1d_Fe-N@CMK-3 catalysts

The first aim of the present work is to study the influence of various mesoporous silica hard-template on the structure and catalytic activity of the resulting carbon-based catalysts. Thus, several catalysts were prepared using the same protocol, but with different silica source. The sample labels are referred to the silica protocol letters from which they come from.

For the first preparation, 404 mg of $Fe(NO_3)_3 \cdot 9H_2O$ was dissolved in 10 mL of water/ethanol (v:v=1:1) using a sonicator. This clear solution was then added in 20 mL of water/ethanol (v:v=1:1) containing 500 mg of the synthesised mesoporous silica (KIT-6-*p6mm*) and 540.6 mg of 1,10-phenanthroline under vigorous stirring at 80 °C for 24 hours to allow the solvent to evaporate. The resulting orange powder was finely grounded in a mortar and then placed in a vertical quartz tube furnace, which was after carefully sealed and purged with constant flowing of N_2 for 20 minutes. The pyrolyser was then heated to 900 °C at a heating rate of 5 °C/min under continuous N_2 flow. The target temperature was kept constant for 3 hours. [21]
Figure 12 shows the resulting powder previous (left) and after (right) pyrolysis treatment.

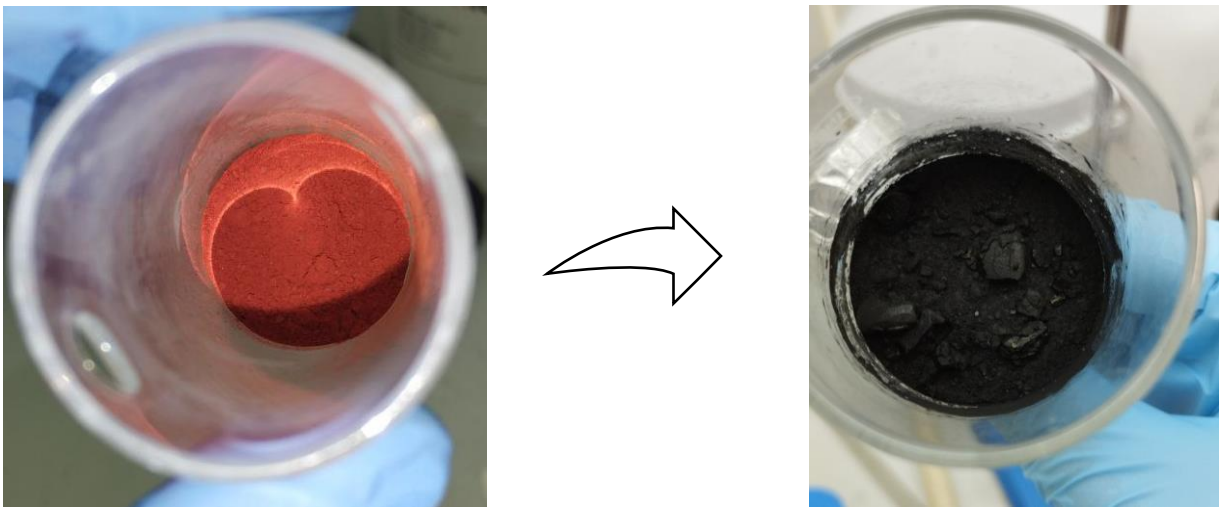

Figure 12. *Powder before and after pyrolysis at 900 °C.*

The resulting sample, labelled as 1a_Fe-N@CMK-8, was then etched under vigorous stirring in 15 mL of a 6M NaOH aqueous solution at 60 °C for 24 hours to remove the silica hard-template. This mixture was then filtered, washed until neutral pH, and dried in the oven overnight. To remove any Fe and/or oxide nanoparticles, the sample underwent acid etching in 50 mL of HCl (37%) for 3 hours at room temperature. It was then filtered and dried again. The successful Fe nanoparticles removal can be clearly seen in figure 13, which shows the filtration step after acid washing: the yellow filtrate

indicates a significant presence of Fe nanoparticles.

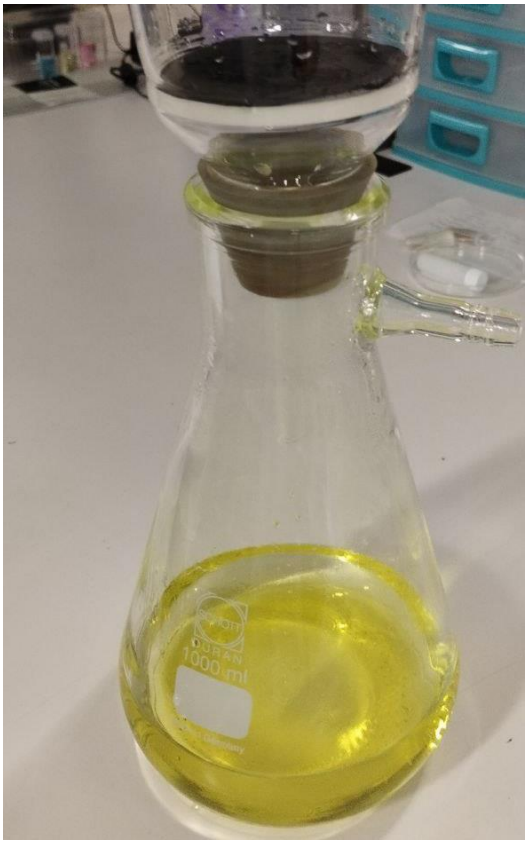

Figure 13. *Catalyst filtration after HCl etching.*

Two additional SAC samples, labelled as 1b_Fe-N@CMK-3/8 and 1d_Fe-N@CMK-3 were prepared using the same procedure. However, these samples used the KIT-6-*dual* and the SBA-15 silica hard-templates, respectively.

- ❖ Protocol 2: Studying the influence of the nanocasting approach into KIT-6 samples: synthesis of 1c_Fe@N-CMK-8

The nanocasting process was modified to enhance the diffusion of the carbon sources into the pore channels of the silica. For that, KIT-6 from protocol c) (with cubic $Ia\bar{3}d$ phase) was used as silica source. The derived carbon material, labelled as 1c_Fe-N@CMK-8, will be compared to samples 1a_Fe-N@CMK-8 and 1b_Fe-N@CMK-3/8 to observe and compare the differences in structure, the amount of coordinated iron, and catalytic activities.
This route involves a two consecutive impregnation steps and includes thermal treatments in a muffle furnace: [13]

1. The first impregnation step uses 500 mg of KIT-6 mixed with 414 mg of 1,10-phenanthroline, in a 3 mL H_2O/EtOH solution (v:v=1:1). Simultaneously, 187.5 mg of $Fe(NO_3)_3 \cdot 9H_2O$ was dissolved in a 2 mL H_2O/EtOH solution (v:v=1:1) using a sonicator. Then, the metal precursor was added to the KIT-6/carbon precursor mixture under vigorous stirring.
2. The resulting mixture was left under vigorous stirring for 1 hour at room temperature. Subsequently, the as-prepared slurry underwent a three-stage thermal treatment process in a muffle furnace under air conditions. The temperature profile consisted of an initial hold at 100 °C for 6 hours, followed by a subsequent increase to 140 °C maintained for 2 hours, and a last

step at 160 °C for 6 hours.

3. This procedure was repeated for the second impregnation step, with a reduction in the initial quantities of the employed reagents: the thermally treated powder was mixed with 250 mg of 1,10-phenanthroline in a 2 mL H_2O/EtOH solution (v:v=1:1), to which 95 mg of dissolved iron source was subsequently added, mixed for 1 hour, and put again in the muffle at 100 °C for 6 h, and at 140 °C for 2 h.

The pyrolysis conditions remained unchanged, reaching 900 °C at a heating rate of 5 °C/min and kept at this temperature for 3 hours. After cooling, the mixture was etched with NaOH and HCl under the same conditions as previously described.

- ❖ Protocol 3. Studying the influence of the nanocasting approach into SBA-15 samples: synthesis of 2d_Fe-N@CMK-3 and 3d_Fe-N@CMK-3

Two additional SAC catalysts have been synthesised starting from the SBA-15 silica of protocol d but slightly changing some conditions. [13]
As concerns the first synthesis, the amounts used in the two impregnation steps were the same as in protocol 2. However, following an initial stirring phase of 1 h at room temperature, the thermal treatment step was conducted under an inert atmosphere (in the pyrolysis reactor under constant N_2 flux). The temperature ramps and durations were as follows: 6 hours at 100 °C, 2 hours at 140 °C, and 6 hours at 160 °C. After cooling to room temperature, the sample was pyrolysed at 900 °C for 3 hours. This approach aimed to minimise potential carbon oxidation during the thermal impregnation processes. Subsequently, after etching to remove the silica template and the Fe/oxide nanoparticles, the sample labelled as “2d_Fe-N@CMK-3” was obtained.

The other sample was prepared in a similar way, using the same amounts and precursors described earlier, with the objective of studying whether the carbon/iron sources diffusion and impregnation in the silica pores were facilitated. In this procedure, the reagents were stirred at room temperature inside a closed Teflon reactor. Then, the Teflon reactor was placed into the muffle furnace for the thermal treatment process and heated up at 100 °C for 6 hours, and subsequently at 160 °C for another 6 hours. This approach aimed to utilise the increase internal pressure within the Teflon reactor to enhance the infiltration of the desired carbon/metal into the silica network. This was evidenced by the higher weight of the remained catalysts after the pyrolysis and etching steps. This method potentially resulted in a lower amount of Fe/C coordinated outside the silica pores network, thereby reducing material loss during subsequent pyrolysis and cleaning steps.
The produced catalyst is labelled as “3d_Fe-N@CMK-3”.

3. Sample characterisation

This chapter delves into the physicochemical characterisation techniques employed throughout this study. A thorough understanding of these techniques is crucial for analysing and describing both the silica hard-templates and the resulting catalysts. These techniques provide valuable insights into the materials' properties.
The following section will provide a detailed theoretical overview of each equipment used, with parameters and obtainable results, followed by chapter 3 which shows the results of the present work.

3.1. Powder x-ray diffraction (PXRD)

X-ray diffraction is a widely, non-destructive, and versatile technique used for the study of crystal structures and their atomic/interatomic spacing. The main principle behind this is the constructive interference of monochromatic X-rays. The latter are generated using a cathode ray tube, filtered to generate a monochromatic radiation, and then directed towards the crystalline sample to be analysed. [22]
As these X-rays interact with the orderly array of atoms within the crystal lattice, constructive interference occurs under specific conditions defined by Bragg's Law. This law dictates the precise relationship between the incident X-ray wavelength, the atomic spacing within the crystal, and the angles at which diffracted beams emerge from the sample:

$$n\lambda = 2dsin(\theta) \qquad (24)$$

Where n is an integer number, λ is the X-rays wavelength, d is the interplanar spacing generating the diffraction, and θ is the diffraction angle.
The diffracted rays are then detected, counted and thus, by scanning the sample through a 2θ angles range, it is possible to understand all the possible diffraction directions of the lattice.
Nevertheless, by converting the measured diffraction peaks into d-spacings, one can identify the compound present in the sample. This identification relies on the unique fingerprint of d-spacings associated with each crystalline material. Typically, the obtained d-spacings are compared against established reference databases containing patterns for known compounds.
The equipment consists of an X-ray tube which produces the beams, a sample holder, and a X-ray detector as illustrated in figure 14. [22]
The X-rays are generated by heating up a metal filament to produce electrons and subsequently accelerating them to bombard a target material. When electrons have sufficient energy to dislodge inner shell electrons of the target material, characteristic X-ray spectra are produced, with specific wavelengths typical of the target material (Cu, Fe, Cr, etc.).
The experiment involves rotating both the sample and the detector to record the intensity of the reflected X-rays. This process allows for the identification of specific crystallographic planes within the sample. When the geometry between the incident X-rays and the crystal lattice satisfies Bragg's Law, constructive interference occurs, resulting in a sharp peak in the recorded intensity.
As it can be seen in the image, the sample rotates in the path of the collimated beam at an angle equal to θ, while the detector is placed on an arm to collect the diffracted X-rays and rotates at an angle of 2θ.

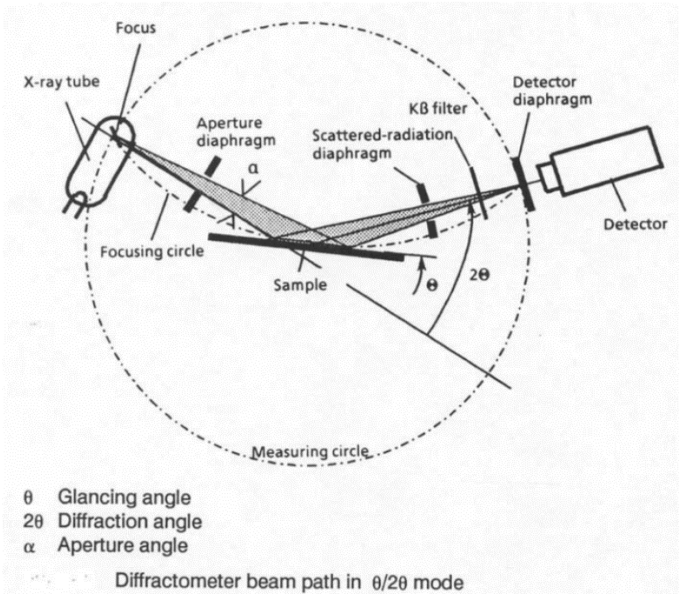

Figure 14. *Schematic diagram of a diffractometer system.* [22]

3.2. Thermogravimetric analysis

The thermogravimetric analysis (TGA) is a characterisation technique which belongs to the thermal analysis branch and investigates the change in weight of a given sample as a function of time or temperature. [23]
During the measurements, the weight change profile is recorded while subjected to constant heating/cooling environment.
It assumes two different names, isothermal mode and scanning mode, when the weight changes are recorded as a function of time or as a function of temperature, respectively.
This versatile technique allows to elucidate various thermal events occurring within a material, such as absorption, adsorption, desorption, vaporisation, and sublimation, alongside chemical transformations like decomposition, oxidation, and reduction.
Beyond simply identifying these processes, TGA is also used to quantify the volatile or gaseous products released during such reactions. Thus, it is particularly useful for analysing materials like nanomaterials, polymers and their composites, fibers, and coatings – materials often incorporating volatile components.
Additionally, TGA offers the ability to predict the thermal stability of a sample, indicating its resistance to degradation at elevated temperatures. This technique can even be employed to study the kinetics, or reaction rates, of chemical processes under various experimental conditions.
In figure 15 a schematic representation of the thermobalance- the heart of the TGA- is illustrated.
It consists of several sub-units such as (i) electronic microbalance, (ii) Sample holder, (iii) furnace, (iv) temperature programmer and (v) recorder.
The electronic microbalance has the purpose of recording all the changes associated with sample mass. Certainly, changes for a sample should be recorded accurately and in a reproducible manner under various atmospheric conditions as well as temperatures.
A typical TG curve depicts the change in sample weight (often expressed as a percentage of the initial mass) plotted against either temperature or time.
As a showing example, a generic plot is reported in figure 16. The latter shows a material undergoing a single-step decomposition process. Within the curve, "T_i" denotes the initial decomposition

temperature, marking the point at which mass loss begins. Conversely, "T_f" indicates the final decomposition temperature, i.e. the point where the decomposition reaction reaches completion. It's crucial to recognise that the specific values of T_i and T_f are directly influenced by the inherent thermal stability of the analysed sample. Materials with lower thermal stability will exhibit earlier onset (T_i) and completion (T_f) temperatures compared to those with higher stability.

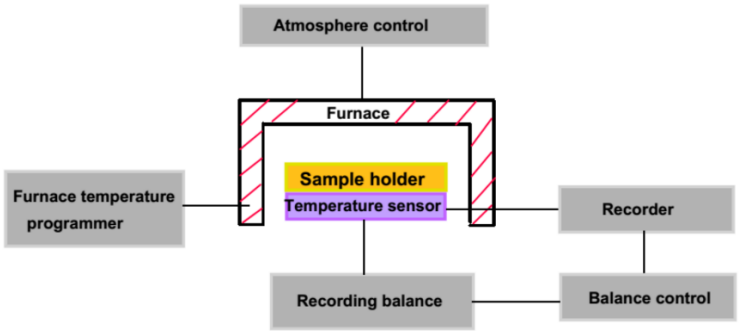

Figure 15. *Schematic illustration of a thermobalance.* [23]

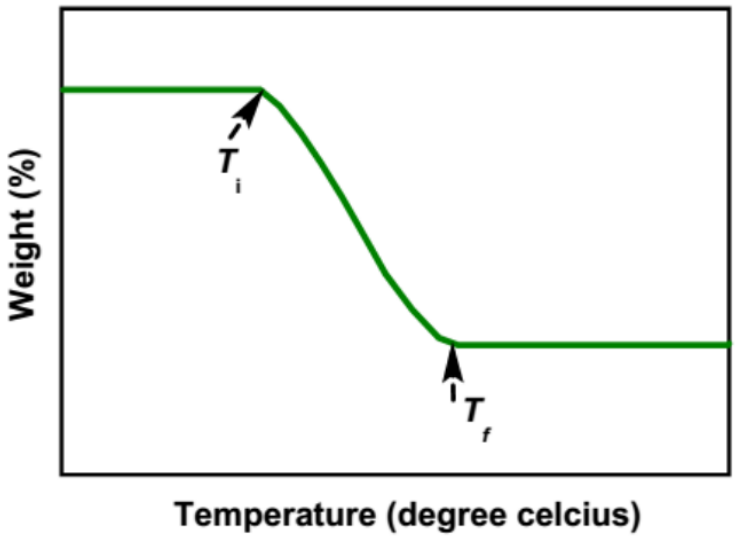

Figure 16. *A typical TG curve.* [23]

3.3. Nitrogen adsorption-desorption at 77 K

The standard procedure for the determination of surface area and pore size distribution of a wide range of porous materials relies on Brunauer and Emmett work from sixty years ago, in which the systematic measurements of the nitrogen physical adsorption at 77 K were undertaken. [24]
Physisorption is a general phenomenon that occurs when an adsorbable gas (named adsorptive) is brought in contact with a solid surface (called adsorbent).
This phenomenon arises due to weak van der Waals forces (VDW forces), leading to a localised increase in gas molecule density near the solid surface.
The reason why these measurements are done using noble gases is due to their full valence electron shells, providing their famous chemical inertness. Thus, they experience minimal interaction (weak van der Waals forces) with the surface being studied compared to other gases. This minimal chemical interaction ensures that the measurement primarily reflects the physical properties of the surface- like surface area and pore size distribution- rather than any specific chemical bonding between the gas

and the surface
To quantify this adsorption process, researchers typically employ constant-temperature experiments, which measure the amount of gas adsorbed as a function of the pressure or concentration of the adsorbate. The resulting relationship at constant temperature, known as the adsorption isotherm, reflects the interaction between the adsorbate and adsorbent, along with the influence of the adsorbent's surface structure and pore geometry.

The pore filling process typically occurs gradually, with smaller pores filling first at lower relative pressures. Relative pressure is denoted by p/p_0, where p_0 represents the saturation pressure of the adsorbate. Conversely, larger pores tend to fill at higher relative pressures. This relationship between pore size and the pressure required for filling is reflected in the distinctive shapes observed in adsorption isotherms. [25]
A classification of physisorption isotherms has been published by the IUPAC and is reported in figure 17, in which is clear the progression in the isotherm shape for nanoporous, mesoporous, and then microporous material.

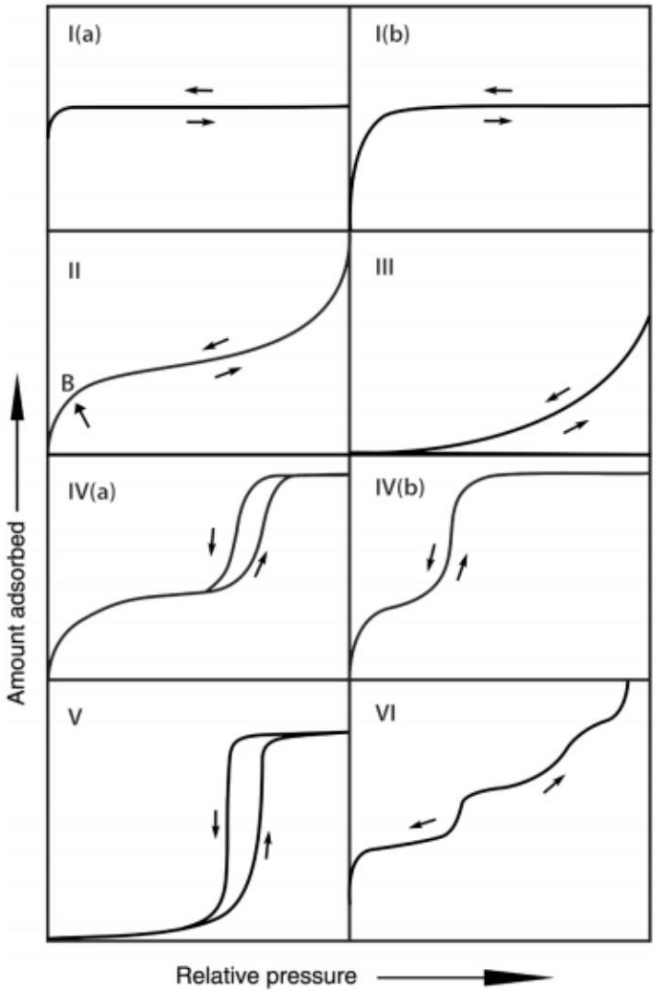

Figure 17. *IUPAC isotherms classification.* [25]

Type I isotherms can be categorised into two subtypes based on the size distribution of micropores within the material. Type I(a) isotherms are characteristic of microporous materials dominated by extremely narrow micropores, often referred to as ultramicropores with diameters smaller than 0.7 nm.
Conversely, Type I(b) isotherms are typically observed in materials containing wider micropores, including supermicropores ranging from 0.7 to 2 nm. The sharp increase in adsorption observed at

very low relative pressures (P/P^0) for both Type I isotherms is attributed to strong interactions between the adsorbent and adsorbate within these confined micropores, which are comparable in size to the adsorbate molecules themselves. This phenomenon leads to rapid pore filling at very low p/p_0 values. Afterwards the isotherm proceeds in a horisontal plateau because the surface is entirely covered with the adsorbate.
Isotherms of Type II are primarily associated with macroporous materials and related to a system showing multilayer adsorption (which starts from the first inflection point) after adsorbing the first monomolecular layer, while the Type III is still typical of macroporous materials, but exhibits a continuous rise in adsorption throughout the pressure range with a concave shape- indicating a relatively weak adsorbent-adsorbate interaction.
Type V presents, at higher relative pressure, an increase in the isotherm typically related to weak adsorbate-adsorbent interactions.
Type VI isotherm, instead, has several inflection points related to gradual formation of individual adsorbate layers, which result from a multimodal pore distribution, while for materials containing mesopores (pores with diameters between 2 and 50 nm), the isotherm shape transitions to the characteristic patterns observed for Type IV(b) and IV(a) isotherms. [25]
In mesopores, the adsorption process involves two key steps: multilayer adsorption followed by pore condensation.
For mesopores with narrow diameters (particularly cylindrical pores less than approximately 4 nm), the adsorption isotherm exhibits complete reversibility, categorised as Type IV(b). However, when the pore width surpasses a critical value dependent on the specific adsorbent-adsorbate system and temperature (typically greater than 4 nm), pore condensation becomes accompanied by hysteresis, resulting in a Type IV(a) isotherm.
The arise of hysteresis and the specific shape of the hysteresis loop are attributed to the concept of adsorption metastability. This phenomenon involves a delay in condensation due to the metastable state of the adsorbed multilayer film. In some cases, pore network effects can also influence the desorption branch of the isotherm. The presence or absence of hysteresis, where the adsorption and desorption curves do not overlap, provides valuable insights into the overall quality of the isotherm data and the pore structure of the material. For mesoporous materials exhibiting hysteresis, further classification of the isotherm type can be performed based on the specific hysteresis loop shape, indeed there exists a specific IUPAC classification, containing four different hysteresis loops reported in figure 18.
More precisely, Type H1 hysteresis is frequently observed in materials containing well-defined, cylindrical pore channels or aggregates of spheres with a relatively uniform size distribution. In contrast, Type H2 hysteresis is associated with disordered porous materials where the pore size and shape distribution is more heterogeneous, potentially including bottleneck constrictions. Type H3 hysteresis is indicative of slit-shaped pores. Notably, isotherms exhibiting this hysteresis loop do not display a limiting adsorption plateau at high relative pressures (p/p_0), which is a characteristic feature observed in non-rigid aggregates of plate-like particles. The desorption branch of the H3 hysteresis loop often exhibits a distinct slope associated with a force acting on the loop. This phenomenon, possibly related to the tensile strength effect, is observed for specific adsorbate-adsorbent systems, such as nitrogen at 77 K within a relative pressure range of 0.4 to 0.45.
Finally, Type H4 hysteresis is also commonly associated with narrow slit-shaped pores.

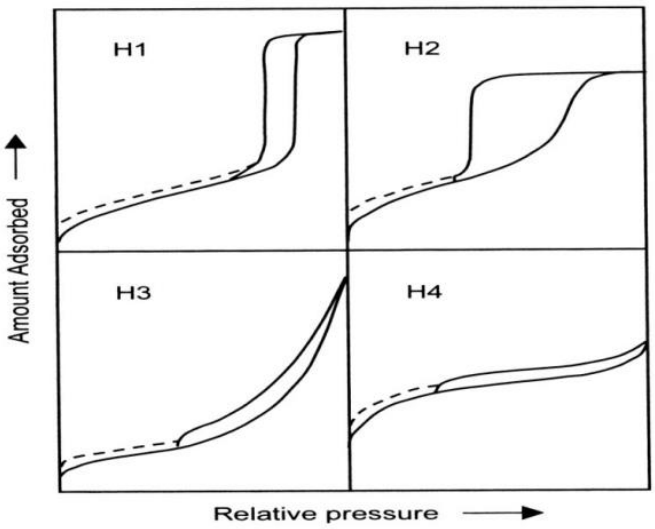

Figure 18. *IUPAC Classification of Hysteresis Loops.* [25]

The surface area and the distribution of the pore dimensions were calculated using the BET and the BJH method, respectively:

- **Brunauer-Emmett-Teller (BET) method:** This method determines the specific surface area (surface area per gram of material) by analysing the adsorption isotherm (a plot of adsorbed amount vs. relative pressure) in the low-pressure region (typically up to ~0.3 relative pressure). It assumes the formation of a monolayer (single layer) of nitrogen molecules on the material's surface.
- **Barrett-Joyner-Halenda (BJH) method:** This method utilises the desorption isotherm (desorption of previously adsorbed gas) to calculate the pore size distribution and pore volume of the material. It relies on the principle of capillary condensation, where nitrogen condenses within pores at lower relative pressures than on flat surfaces. By analysing the hysteresis loop in the isotherm (difference between adsorption and desorption), BJH estimates the pore size distribution.

3.4. Scanning transmission electron microscopy

A Scanning Transmission Electron Microscope (STEM) is used to image and analyse materials at the atomic level. [26]

- The process starts with an electron gun that emits a beam of high-energy electrons. This beam is then focused by a series of condenser lenses to create a very fine spot, typically with a diameter of 0.05 – 0.2 nm. This tiny spot is called the probe. As the electrons pass through the sample, they interact with the atoms and can be either transmitted- continue through the sample and carry information about the material's internal structure- or scattered – deflected from their original path by collisions with atoms.

Detectors are placed all around the sample to collect these transmitted and scattered electrons.

The collected signals from transmitted and scattered electrons are used to form an image.

- Bright-field (BF) images: Similar to a conventional transmission electron microscope (TEM), these images show darker areas corresponding to regions where more electrons are transmitted (thinner or less dense parts of the sample).

- Annular Dark-Field (ADF) and High-Angle Annular Dark-Field (HAADF) images: These techniques focus on scattered electrons, with HAADF being particularly sensitive to the atomic number (Z) of the elements. Heavier elements scatter electrons more strongly and appear brighter in the image. This allows for visualisation of atomic arrangements and differentiation between elements with high spatial resolution.

Additionally, Energy-Dispersive X-ray Spectroscopy (EDS) is a powerful technique used in conjunction with the STEM imaging, providing crucial information about its elemental composition. During STEM operation, the high-energy electron beam interacts with the atoms in the sample. This interaction can cause the ejection of inner-shell electrons from the atoms. As outer-shell electrons jump down to fill the vacancies in the inner shell, they release energy in the form of X-rays, and the EDS detector positioned within the STEM captures these emitted X-rays.
Each element has a unique characteristic X-ray energy spectrum, thus by analysing the energy and intensity of the detected X-rays, EDS identifies the elements present in the sample. The intensity of the X-rays is proportional to the concentration of the element, allowing for semi-quantitative analysis of the elemental composition.

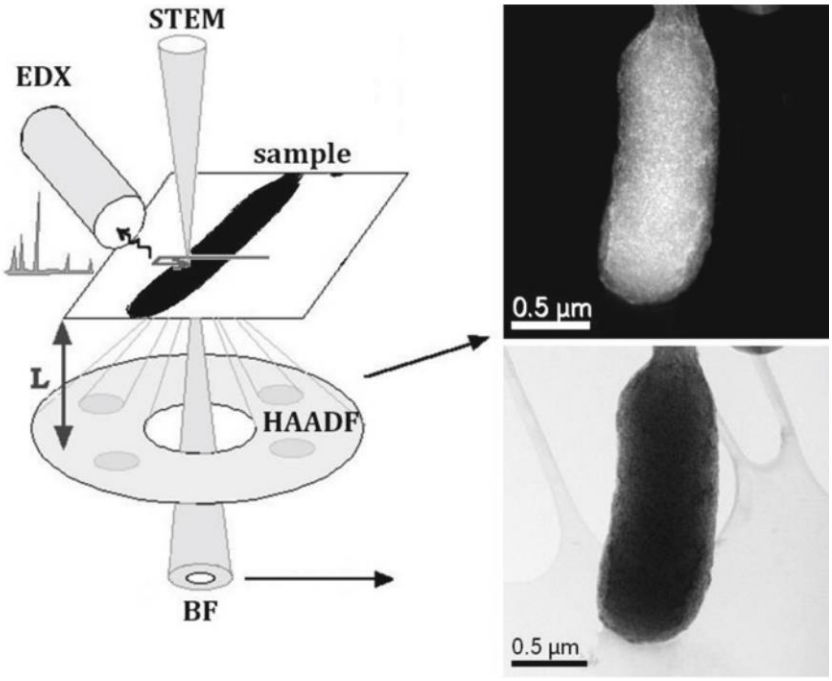

Figure 19. *STEM setup, EDS spectrum detector, and HAADF/BF related images.* [26]

3.5. Characterisation conditions

Powder X-ray diffraction (PXRD) data were acquired with a Rigaku Geigerflex D Max-C Series diffractometer using Cu-Kα radiation in transmission mode (using focusing mirror geometry) using a Cu-Kα radiation, at an operating voltage of 45.0 kV and a tube current of 40.0 mA. Samples were step-scanned in 2θ steps = 0.026º.

Thermogravimetric analysis (TGA) were made on a Shimadzu TGA-50 instrument, with a program rate of 5 ºC/min in air. Temperature range 25-800 °C

Scanning transmission electron microscopy (STEM) images were taken using a Hitachi® model HD2700 type B microscope, operating at 200 kV acceleration potential.
Samples were dispersed in ethanol via gentle sonication, and a droplet of the suspension was applied onto a lacey carbon-coated copper grid from Agar Scientific®. The grid was then allowed to dry at room temperature.

Nitrogen adsorption-desorption isotherms were collected at 77 K (-196 ºC) using a Gemini V 2.00 instrument model 2380. The surface area and the distribution of the pore dimensions were calculated using the Brunauer-Emmett-Teller (BET) method and Barrett-Joyner-Halenda (BJH) method, respectively.

Electrochemical characterisations were performed at room temperature with a CHI760E electrochemical workstation and ALS RRDE-3A rotating ring disk electrode apparatus. The catalyst samples were deposited onto a glassy carbon disk/Pt ring working electrode (electrode area 0.1256 cm^2). Graphitic carbon was used as counter electrode, while Ag/AgCl was used as reference electrode. Rotating disk electrode (RDE) tests were carried out through linear sweep voltammetry (LSV) in the potential range 0.18 V–1.18 V with a scan rate of 5 mV/s and variable rotation speed in the range 400–2500 rpm. Rotating ring-disk electrode (RRDE) measurements were carried out through LSV in 4-electrodes configuration (disk/ring/reference/ counter electrodes) by scanning the disk electrode from 0.18 V to 1.18 V (scan rate 5 mV/s) and fixing the ring potential at 1.18 V.

4. Results and discussion

4.1. Silica structures and morphologies

To understand the properties of the catalysts under investigation, this sub-section will examine the characterisation data of the sacrificial hard templates from which SAC samples are derived.
Figure 20 displays the powder X-ray diffraction patterns of all the KIT-6 and SBA-15 samples.
As indicated by its name (*KIT-6-p6mm*), the sample from protocol a shows a diffraction pattern closely resembled that of SBA-15 material. This similarity arises because, following Freddy Kleitz protocol, during the initial stirring phase, the reaction vessel remained unsealed for 24 hours, allowing simultaneous evaporation of butanol and hydrochloric acid. This process is crucial for achieving a 2D-hexagonal pores arrangement.
Despite originating from a KIT-6 protocol and lacking a 3D pore structure, the final material exhibits a well-organised 2D pore arrangement with *p6mm* symmetry. The main peaks observed at $2\theta \approx 0.96°$,1.60° and 1.90° are typical for mesoporous silica with 2D-hexagonal pore network, corresponding to the [100], [110], and [200] planes, respectively. [10]

On the other hand, it is evident that only the green plot from the KIT-6 sample exhibits the two main characteristic peaks around $2\theta \approx 1.00°$, 1.15° related to the [211], and [220] planes, consistent with the expected pattern for KIT-6 mesoporous silica with a cubic $Ia\bar{3}d$ structure. [16]

Moreover, the intermediate diffractogram from KIT-6-*dual* shows similarities with both 3-D structured and 2-D structured materials, reflecting its dual structure as further confirmed by STEM images. This dual structure was achieved by employing a more acidic condition during the synthesis. Specifically, an additional 0,2 g (or 0,17 mL) of HCl was added compared to the standard procedure, as a more acidic environment promotes the formation of 2D-hexagonal pores. [17]

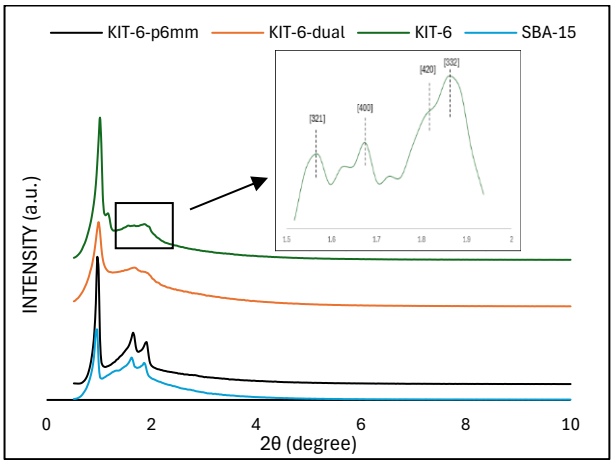

Figure 20. *PXRD graphs of the silica hard templates.*

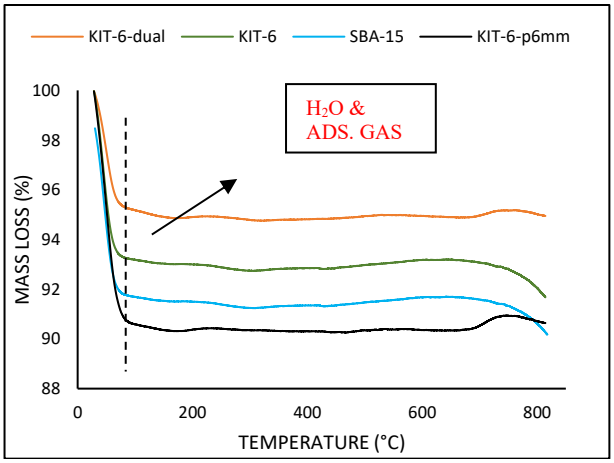

Figure 21. *Silica templates thermogravimetric plots.*

Figure 21 shows the thermal stability of the silica-derived samples.
TGA of all samples show one weigh loss peak below 100 ºC, that can be related to the desorption of adsorbed water and gases.
The absence of other weight losses indicates that the surfactant was efficiently removed through the combination of the solvent-extraction method and calcination at 550 ºC.

N_2 adsorption-desorption isotherms at 77 K were collected to obtain the textural properties for the silica samples and the results are summarised in figure 22 and Table 1.
Figure 22 (a) reveals that the synthesised silicas exhibit a type IV isotherm with a H1 hysteresis loop, classified according to IUPAC standards, which is characteristic of mesoporous materials as discussed earlier (Chapter 2).
However, KIT-6 with cubic $Ia\bar{3}d$ structure, also resembles a type II isotherm due to the increase in adsorption without limit when $p/p^0 = 1$. This can be related to the presence of some nonporous or macroporous phases. [27]

Table 1. *Textural properties of mesoporous silicas.*

	KIT-6-*p6mm*	KIT-6-dual	KIT-6	SBA-15
PORE STRUCTURE	HEXAGONAL (*p6mm*)	HEXAGONAL /CUBIC	CUBIC (*Ia$\bar{3}$d*)	HEXAGONAL (*p6mm*)
S_{BET} (m^2/g)	554	556	833	734
V_p (cc/g)	0.68	0.43	2.84	0.79
D_p (nm)	5.47	5.95	3.55	6.53

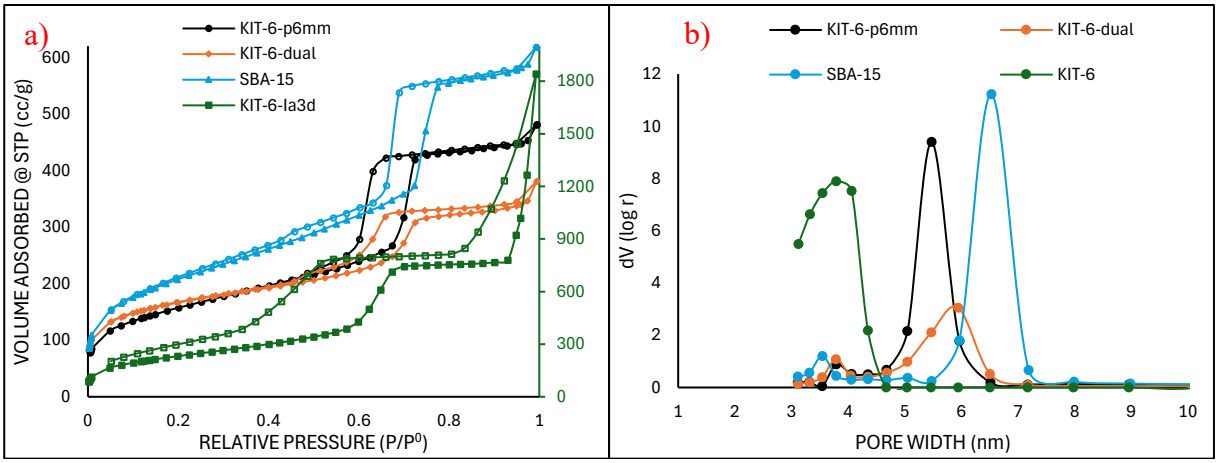

Figure 22. *(a) N_2 adsorption desorption isotherms of the mesoporous silica templates. Fully symbols reflect adsorption branches, empty symbols correspond to desorption ones. (b) Pore size distribution of the mesoporous silicas.*

By applying the BET and BJH theories to the N_2 adsorption/desorption isotherms specific surface area (S_{BET}), the pore volume (V_p) (Table 1) and the pore size distribution curves (figure 22 (b)) can be determined.

Figure 22 (b) indicates that most of the synthesised silicas have a narrow distribution of pore sizes, except for the KIT-6 sample. The pore diameters are within the mesoporous range, between 5.8 and 8.1 nm. However, despite these favourable characteristics, the first two KIT-6 samples possess a relatively low surface area of approximately 555 m²/g compared to mesoporous materials in general. [28]

Conversely, the KIT-6 sample exhibits the highest surface area, even exceeding that of the SBA-15 sample. Notably, this sample displays a remarkably high pore volume, nearly double that of values reported in the literature. However, this value requires double confirmation.

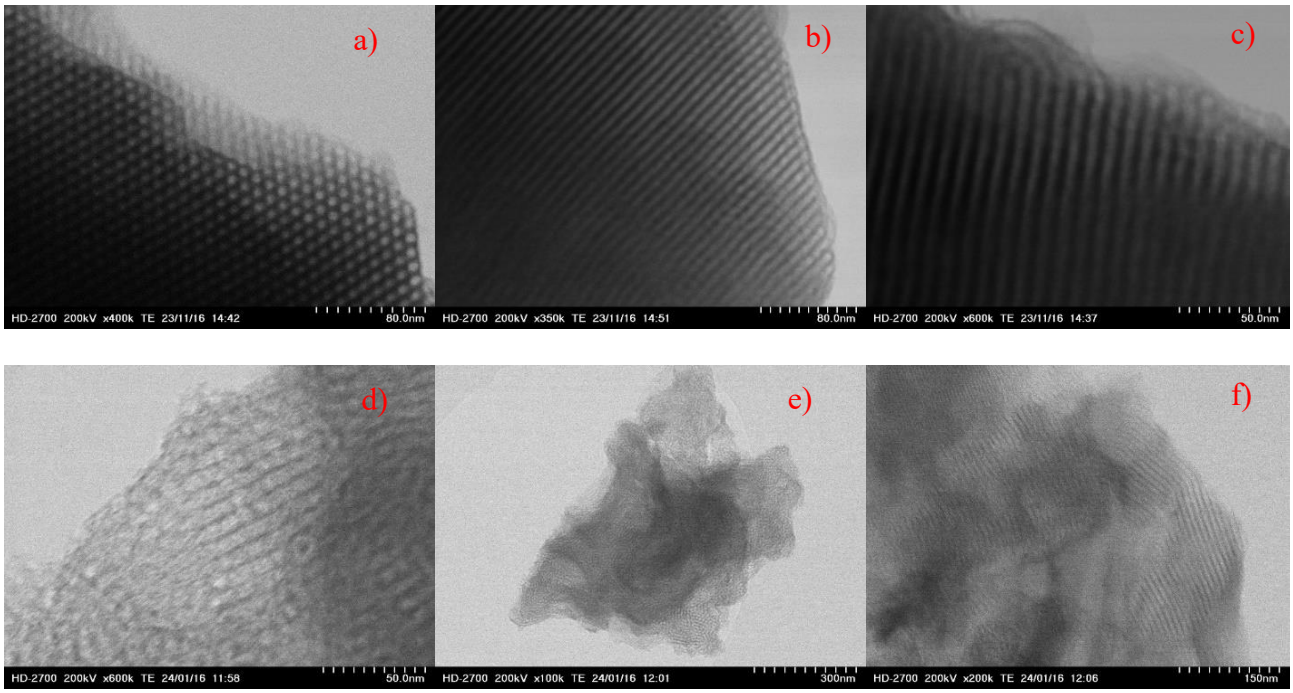

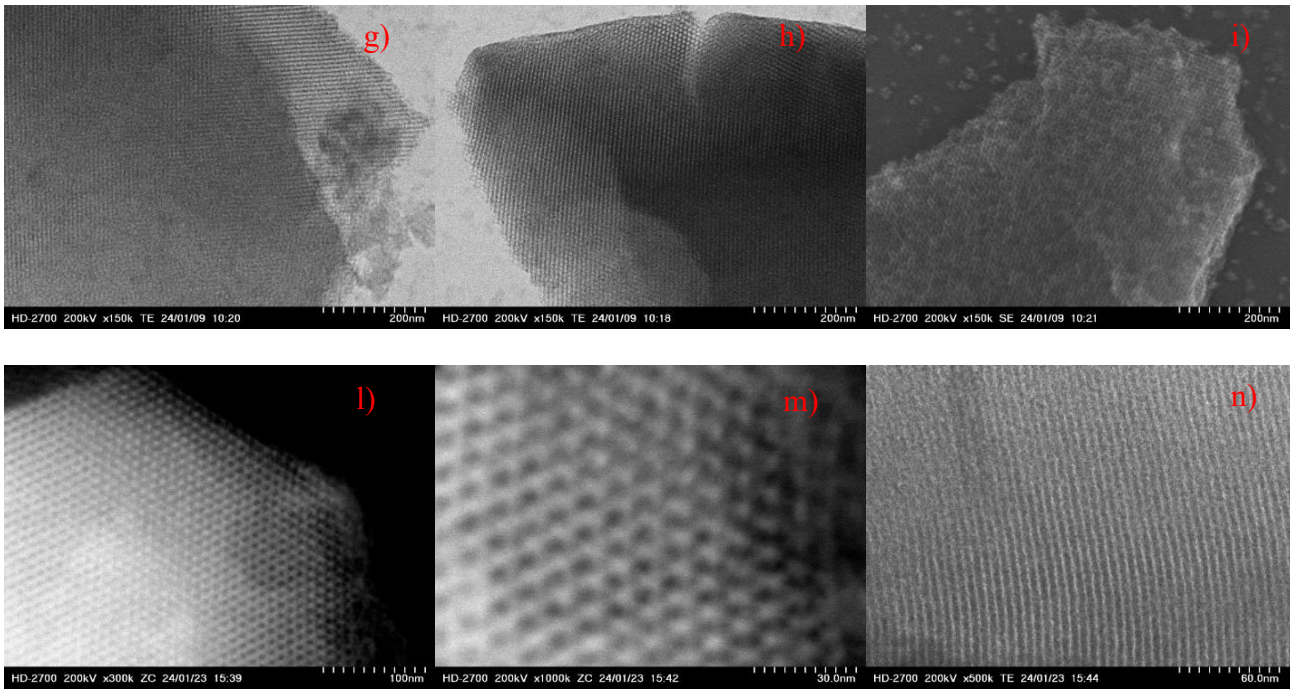

Figure 23. *(a), (b), (c) TEM images of KIT-6-p6mm mesoporous silica. (d), (e), (f) TEM images of* KIT-6-*dual mesoporous silica. (g), (h), (i) TEM and SEM images of KIT-6 mesoporous silica. (l), (m), (n) TEM and ZC images of SBA-15 mesoporous silica.*

Transmission electron microscopy (TEM) images of the materials are presented in Figure 23. Firstly, figures 23 (a), (b) and (c) offer additional evidence supporting the formation of a hexagonal pore network in the KIT-6-*p6mm* silica, and the same pore organisation is visible for SBA-15 sample presented in figure 23 (l) (m) and (n) yet showing differences in the textural properties indicating that are different from SBA-15 material.
Figures 23 (g) and (h) reveal the perfect cubic structure with $Ia\bar{3}d$ symmetry of the KIT-6 sample.

4.2. Catalysts structures and morphology

In the following paragraphs a comprehensive overview of the morphological and textural properties of the catalysts, highlighting how variations in silica sources and nanocasting procedures influences the resulting samples.

4.2.1. Studying the influence of the silica source morphology

The powder XRD diffractogram for the catalysts 1a_Fe-N@CMK-8, 1b_Fe-N@CMK-3/8, and 1d_Fe-N@CMK-3 derived from KIT-6-*p6mm*, KIT-6-*dual*, and SBA-15 silica hard-templates, respectively, were recorded. The catalysts were obtained by using the same impregnation and pyrolysis methods, following protocol 1 (for more details see Chapter 2).

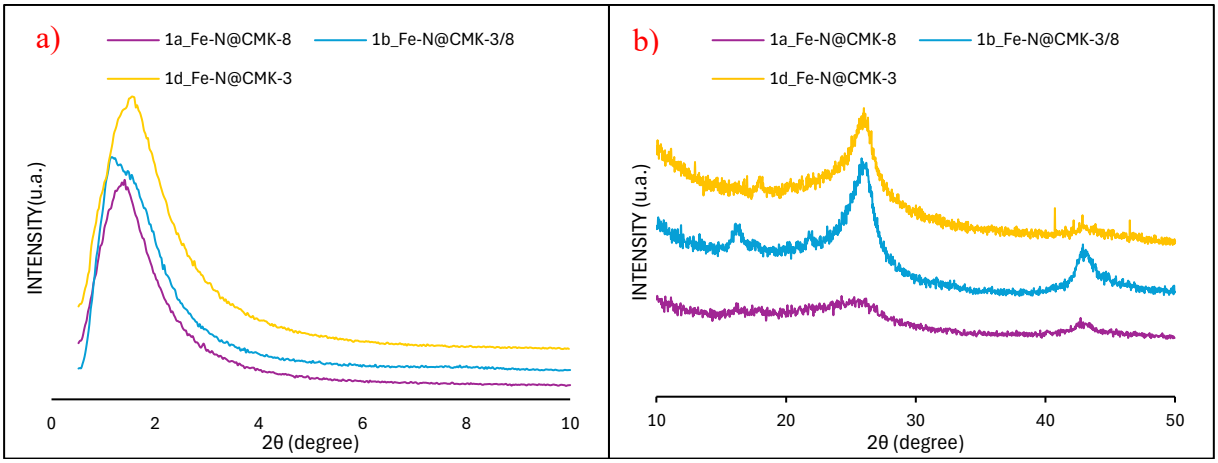

Figure 24. *(a) Low angle XRD of 1a_Fe-CMK-8, 1b_Fe-N@CMK-3/8, and 1d_Fe-CMK-3 samples. (b) High angle XRD of 1a_Fe-CMK-8, 1b_Fe-N@CMK-3/8, and 1d_Fe-CMK-3 samples.*

Low-angle XRD diffraction patterns (figure 24 a) from all the KIT-6s and SBA-15/carbon composites exhibited much lower overall intensity in comparison to the corresponding silica templates.
A first broad peak is exhibited in all synthesised samples, at around $2\theta \approx 1.5$ °, which is likely originated from the scattering of X-rays by some degree of periodicity of the mesopores channels, related to the [100] diffraction planes. The absence of the two additional diffraction patterns corresponding to the [110] and [200] planes may be attributed to potential pore disorder, likely due to the lack of formation of cubic and hexagonal arrangements of the pores during the nanocasting process.
At higher diffraction angles (in figure 24 b) two sharp peaks at approx. $2\theta \approx 25$ ° and 43 ° can be observed and attributed to graphitic carbon, corresponding to its [002] and [101] diffraction planes, respectively [29]. The latter carbon rearrangement is more noticeable within sample 1b_Fe-N@CMK-3/8, confirmed by the TEM images in figure 30 (a) and (b). On the other hand, it is evident that the 1a_Fe-N@CMK-8 synthesised from KIT-6-*p6mm* shows the least graphitised structure, as its peaks are barely observable.

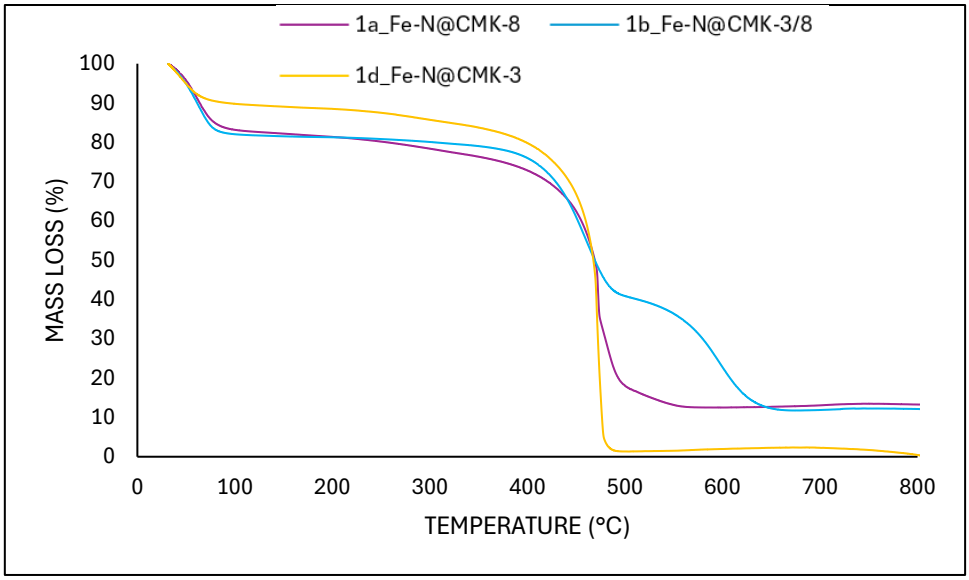

Figure 25. *TG plots of the CMK-3 and CMK-8 derived catalysts.*

The catalysts thermal stability and their approximated composition was analysed be TG and the results are presented in Figure 27. [30] An initial analysis of the TGA results reveals a consistent trend for all the materials, suggesting a shared degradation mechanism despite the different hard templates. This implies similar chemical structures and components that decompose at comparable temperatures.

Following an initial mass loss between 10 wt.% and 20 wt.% attributed to the evaporation of moisture and adsorbed gases below 100 °C, within the temperature range of 400-650 °C -where is typically observed the degradation of carbon and nitrogen species [30] - the sample 1a_Fe-N@CMK-8 shows a mass loss of around 65 wt.%, leaving almost 13 wt.% of undegraded material until 800 °C. This suggests that a considerable amount of Fe clusters and silica source persists despite undergoing two acid and alkaline etching steps. On the other hand, sample 1d_Fe-N@CMK-3 showed the biggest mass loss within this temperature range, nearly 83 wt.%, leaving less than 2 wt.% of residual mass that can be attributed to Fe nanoparticles or residual silica. This suggests that the SBA-15 silica facilitate better precursors diffusion, likely due to its larger pore diameter and a more open framework compared to the other KIT-6s samples. (14) This can also enable easier penetration of the NaOH and HCl during the etching processes, resulting in more efficient Si and Fe removal.

Sample 1b_Fe-N@CMK-3/8 presents three distinct degradation steps: after the initial mass 18 % loss related to the moisture/adsorbed gases, it shows a loss of 38% between 400 °C and 500 °C followed by the last 27% in the range 550-650 °C, leaving behind 12% of undegraded material. Further analysis, such as *operando* TGA-IR to study the gas evolution during the degradation process, is needed to fully understand the reasons behind these observations. [31]

Regarding catalysts textural properties, in the following table 2 and figure 26 (a) and (b) are shown respectively numerical values, the adsorption/desorption isotherms at 77 K, and the pore size distribution curves- calculated by the Barrett-Joyner–Halenda (BJH) methods.

Compared to their respective hard templates, these composites exhibited slightly lower adsorption volume. However, porosity analysis revealed the presence of pores within the composites. Notably, the pore size remained consistent across all samples ranging from 3.1 up to 7 nm with a sharper peak common to every sample appearing at 3.8 nm, indicating a dominant population of uniform mesopores around this size. Moreover, there is another set of pores that vary more in size, ranging from 8 nm on, indicating a non-hierarchical pore arrangement.

Despite the KIT-6 silica has the highest surface area, the catalysts 1b_Fe-N@CMK-3/8 and 1d_Fe-N@CMK-3 have a notable higher surface area (695 m^2/g and 625 m^2/g, respectively) compared to

1c_Fe-N@CMK-8 from KIT-6, demonstrating that a well-structured silica template does not automatically mean a carbon negative replica with perfect textural properties.

Table 2. *Textural properties of CMK-3 and CMK-8 derived catalysts.*

	1b_Fe-CMK-3/8	1c_Fe-N@CMK-8	1d_Fe-N@CMK-3
S_{BET} (m^2/g)	695	488	625
V_p (cc/g)	0.45	0.20	0.36
D_p (nm)	3.78	3.79	3.77

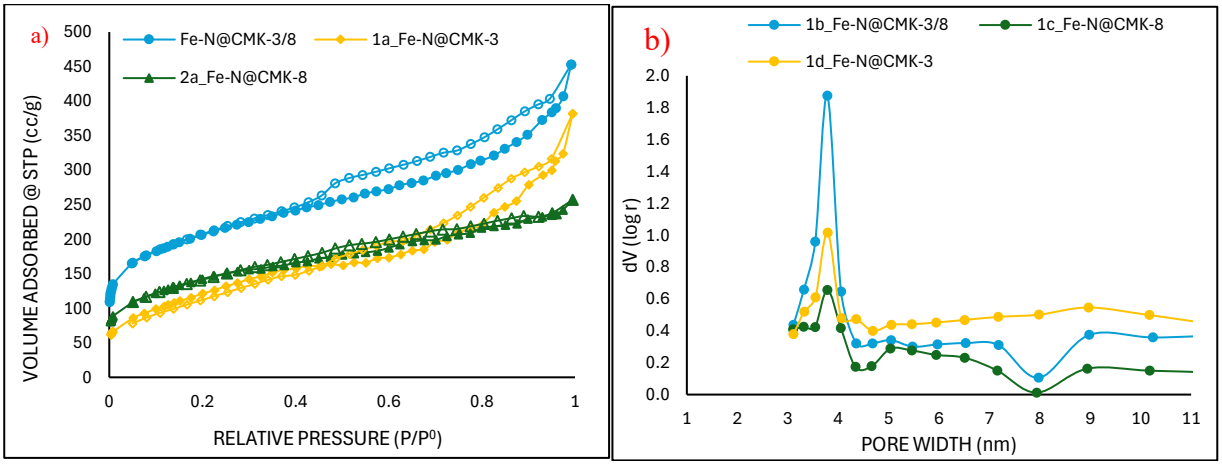

Figure 26. *(a) 77 K Nitrogen adsorption/desorption isotherms of Fe-CMK catalysts. Fully symbols denotes adsorption process and empty symbols correspond to the desorption process. (b) Pore size distribution curve calculated from desorption branch of the isotherm by the BJH method.*

From N2 adsorption/desorption isotherms in figure 26 (a) it can be seen that, differently from the silicas type IV, the isotherms obtained for the carbon replicas coming from the three distinct silica templates are between type I(b) -at lower partial pressure values- and type II, indicating the presence of mainly narrow mesopores with ink-bottle shaped pores. [27]
Additionally, the catalysts show the presence of a H4 hysteresis loop, given when the initial region of reversible pore filling is followed by multilayer physisorption and capillary condensation. [32]
This description is consistent with what visible from the pore size distribution since Type I(b) isotherms are found with materials having pore size distributions over a broader range of dimensions, while Type II isotherm, from the IUPAC classification [27], is directly related to the adsorption of nonporous materials -confirmed by the STEM images reported before that show high degree of graphitisation and amorphousness- where this shape is the result of unrestricted monolayer-multilayer adsorption up to high p/p^0.
It is also possible to state that in the present cases the point B, appearing in the theoretical description in figure 17 from section 2.3.3, is less distinctive (meaning a more gradual curvature), thus an indication of a significant amount of overlap of monolayer coverage and the onset of multilayer adsorption. [33]

4.2.2. Studying the influence of the nanocasting approach from KIT-6 samples

After a general overview of the different silicas, in this section the influence of the nanocasting approach from the KIT-6 derived samples is studied. Thus, catalysts from protocol 1 and 2.

In figure 27 (a), (b) and 30 the low and high angle XRD and TG plots are presented, respectively.

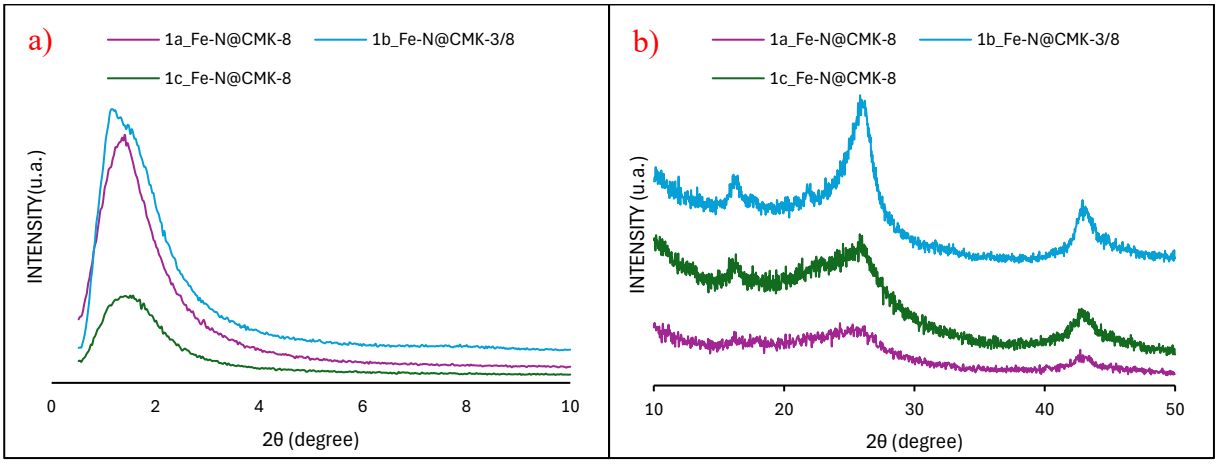

Figure 27. *(a) Low angle XRD of 1a_Fe-CMK-8, 1b_Fe-N@CMK-3/8, and 1c_Fe-CMK-8 samples. (b) High angle XRD of 1a_Fe-CMK-8, 1b_Fe-N@CMK-3/8, and 1c_Fe-CMK-8 samples.*

All the samples show two broad peaks at 2θ values around 26° and 43°, corresponding to the [002] and [101] diffractions (figure b), suggesting that they are mostly amorphous with a low degree of graphitisation, as already discussed in the previous paragraph.(29) [34]
However, the carbon nanotubes (CNTs) visible in STEM figure 32 (c) are not easily detected from XRD, since CNTs patterns show similarities to one from graphite because of their similar intrinsic graphene properties. [35]
Additionally, it can be noticed that the peak appearing at 16° is common to all those samples and a small one for $2\theta \approx 21°$ which are related to SiO_2 diffraction peak [36], additional confirmation that even if the impregnation processes have changed, the final materials show similarities in the final products related to the intrinsic smaller pore diameter and complex pore network of KIT-6 derived materials, which might have led to a more difficult etching solution reaching all the interior silica regions.

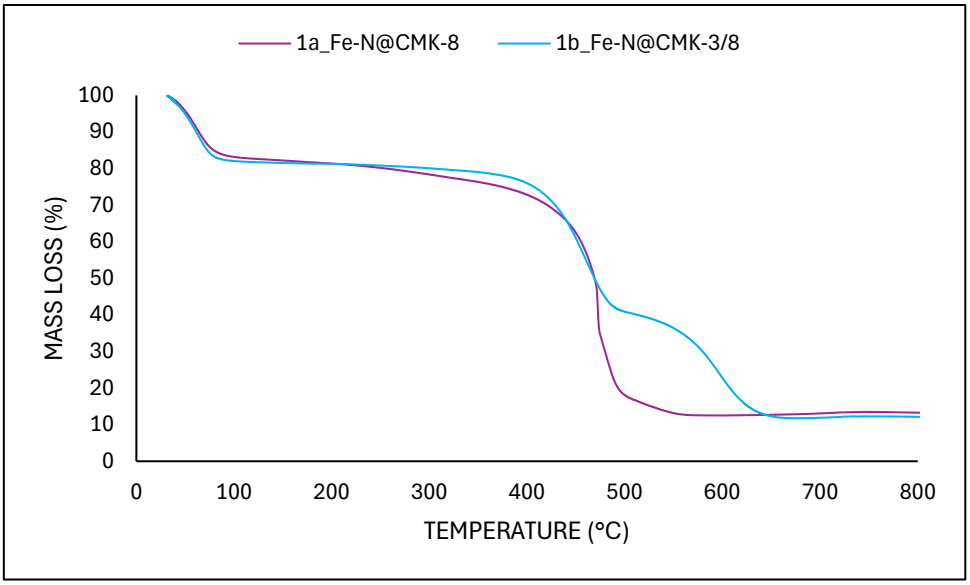

Figure 28. *TG plot from 1a_Fe-N@CMK-8 and 1b_Fe-N@CMK-3/8 samples.*

From TG plot in figure 28, the materials show the same degradation process, as well as almost the same residual amount beyond 800 °C of 11.7 wt.%, showing the more tedious pore networks intrinsic of KIT-6 derived materials.

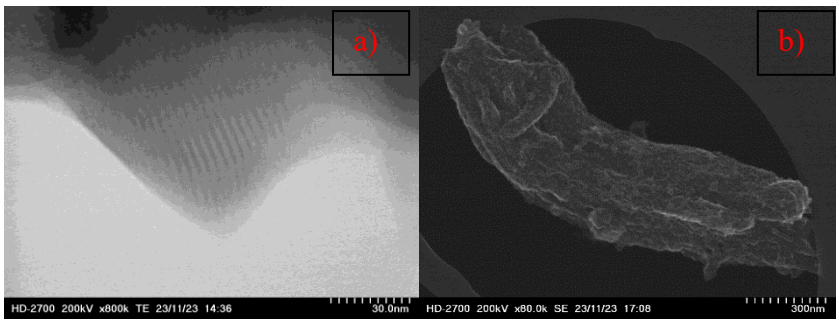

Figure 29. *(a),(b) STEM images of the 1a_Fe-N@CMK-8 from KIT-6-p6mm.*

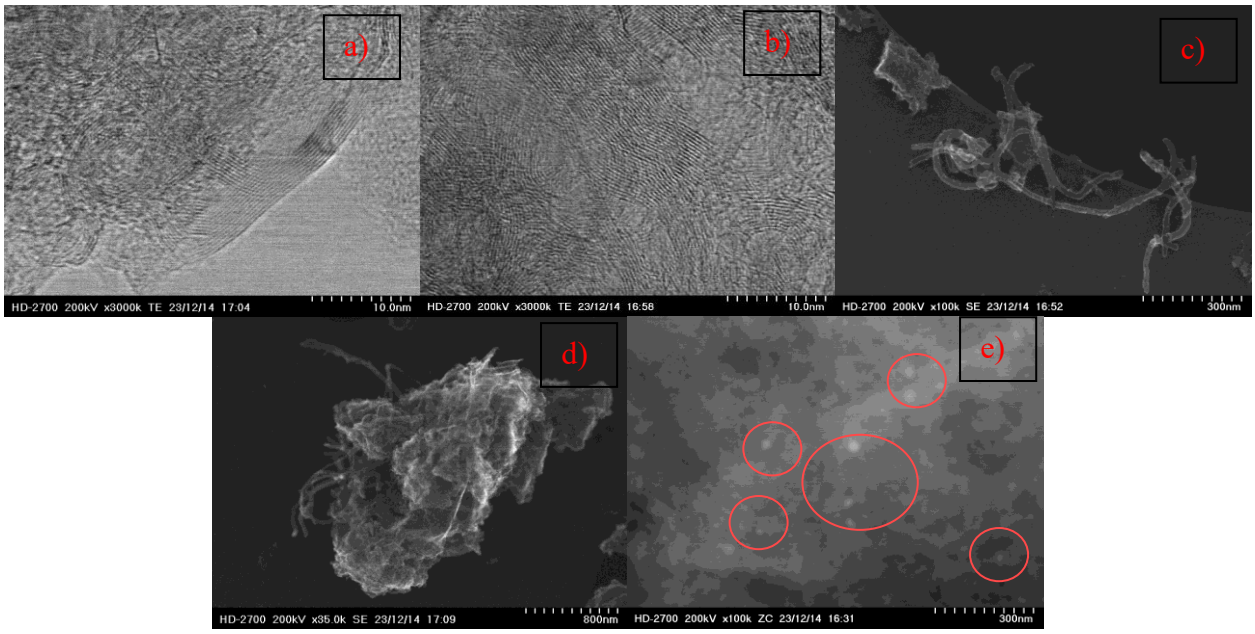

Figure 30. *(a),(b),(c),(d),(e) STEM and ZC images of the 1b_Fe-N@CMK-3/8 from kit-6-dual.*

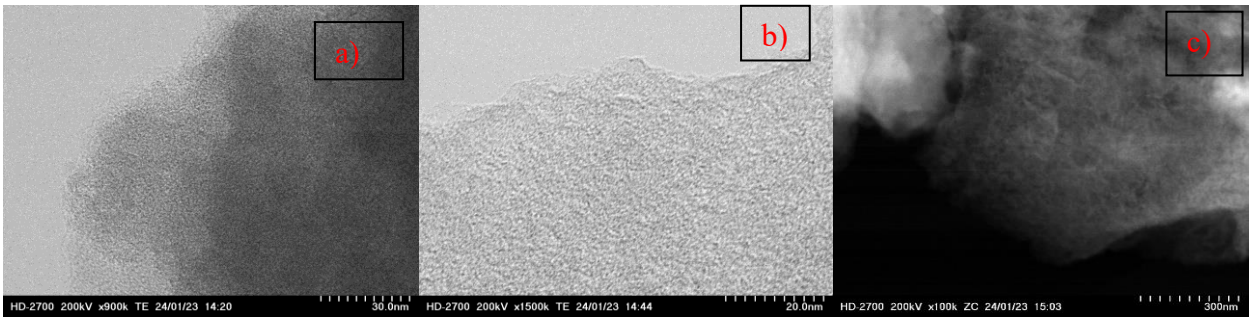

Figure 31. *(a),(b),(c) TEM and ZC images of the 1c_Fe-N@CMK-8 from KIT-6.*

STEM images reveal that sample 1a_Fe-N@CMK-8 (figure 29 (b)) was the only one which kept the rod-like macro shape of the original hard template while in figure 29 (a) it is also visible the hexagonal mesopore structure, thus indicating that this catalyst maintained very well both the macro and meso structures.

Sample 1b_Fe-N@CMK-3/8 shows no rod-like particles (figure 30 (d)). However, it is the most interesting sample -from a morphological point of view- showing more than a single structure: we also have a visualisation of some carbon nanotubes in the macrostructure (figure 30 (c)), along with some graphite (figure 30 (b)). Notwithstanding the carbon organisation, some iron nanoparticles are still present even after the acid etching step as elucidated in figure 30 (e) from the brighter spots, as well as some residual silica from EDS analysis (figure 32 (f)).

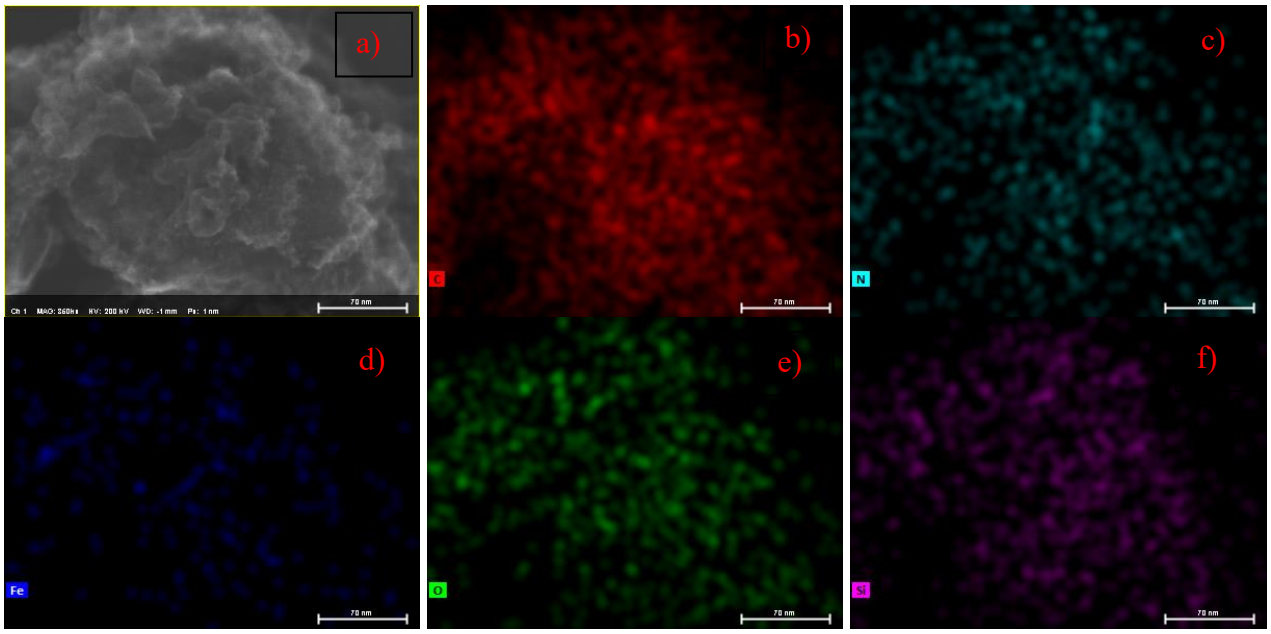

Figure 32. *(a),(b),(c),(d),(e),(f) EDS analysis of 1b_Fe-N@CMK-3/8.*

Sample 1c_Fe-N@CMK-8 TEM images in figure 31 (a) and (b) underline the presence of a porous structure even though it does not show any crystalline arrangement, situation that can be attributed to the too short stirring step which did not allow the carbon source to properly diffuse within the pores. This situation was further confirmed by the evaporation and recrystallisation of 1,10-phenanthroline all around the pyrolysis reactor walls at around 400 °C, visible from figure 33.

On the other hand, this protocol allowed the synthesis of a truly atomically dispersed catalyst, since ZC image in figure 31 (c) do not show any bright spot (Fe cluster).

Figure 33. *1,10-phenanthroline crystalised at the bottom of the pyrolysis reactor.*

4.2.3. Studying the influence of the nanocasting approach from SBA-15 samples

As already done for the KIT-6 samples, in the following section the difference in the hard-template approaches will be studied. As a first result, in figures 34 the XRD plots are shown and in figure 35 the TG ones.

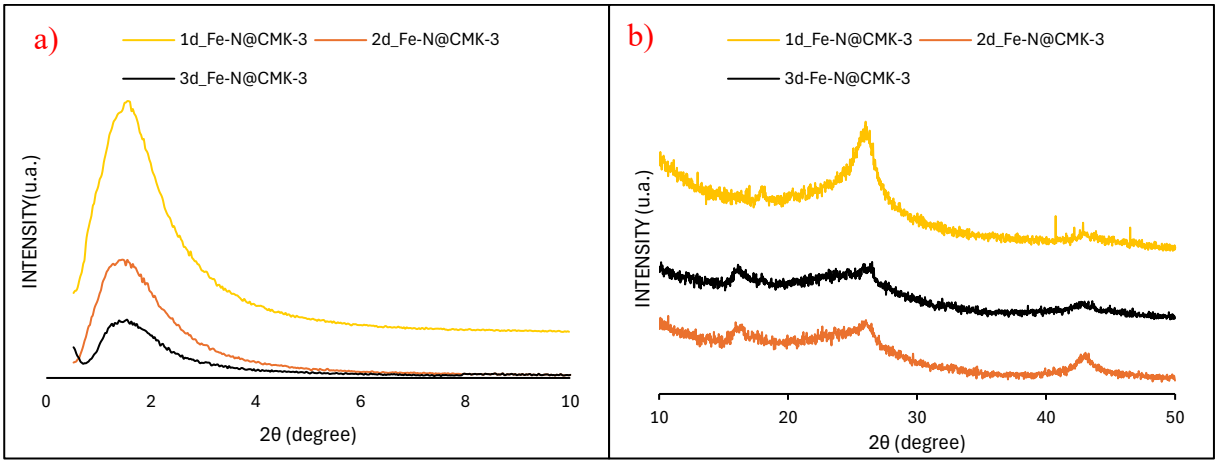

Figure 34. *(a) Low angle XRD of 1d_Fe-CMK-3, 2d_Fe-CMK-3, and 3d_Fe-CMK-3 samples. (b) High angle XRD of 1d_Fe-CMK-3, 2d_Fe-CMK-3, and 3d_Fe-CMK-3 samples.*

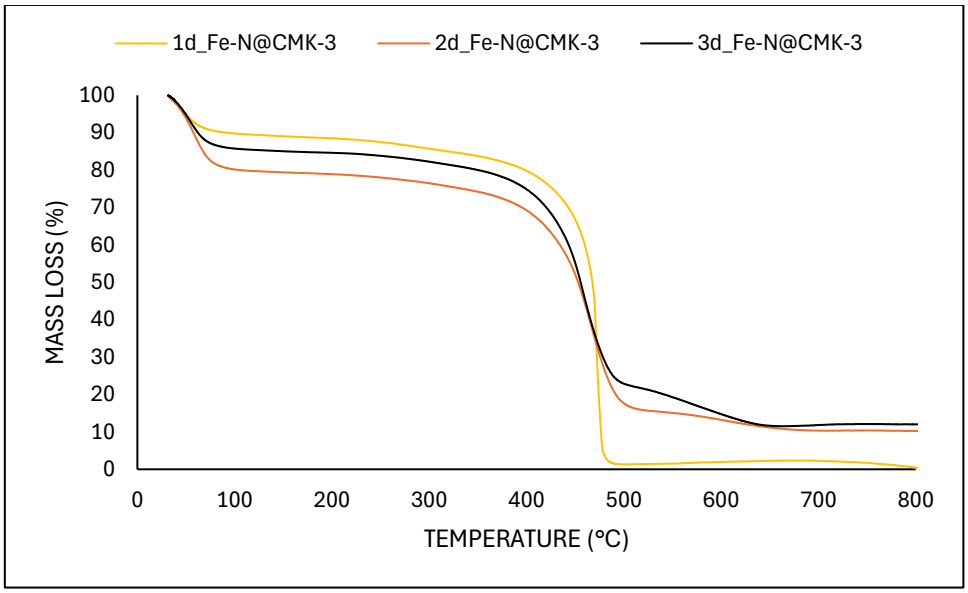

Figure 35. *1d_Fe-CMK-3, 2d_Fe-CMK-3, and 3d_Fe-CMK-3 catalysts TG plots.*

From figure 34, 2d_Fe-N@CMK-3 and 3d_Fe-N@CMK-3 catalysts show the same diffraction peaks at $2\theta \approx 16°$ (related to the presence of SiO_2 also showed in sample from protocol 2), 26° and 43°, while sample 1d_Fe-N@CMK-3 shows only the two latter peaks related to graphitic carbon.

TG plots show the same trend for samples 2d and 3d Fe-N@CMK-3 , with the same degradation process for each temperature window as well as the same residual mass of 12 wt.%, further confirmation of the presence of residual silica assumed from diffraction peak at 16° and, eventually,

some iron clusters.
1d_Fe-N@CMK-3 as already discussed shows an almost complete degradation, presenting less than 2 wt.% of the total mass as silica and Fe clusters.

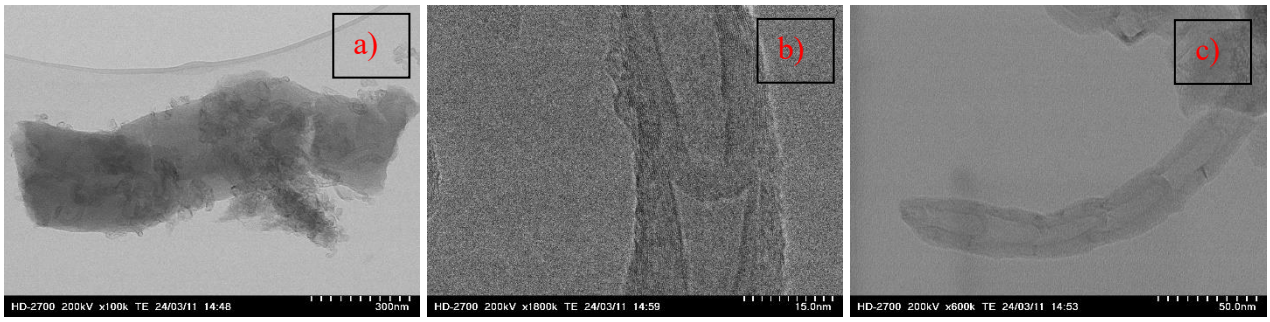

Figure 36. *(a),(b),(c). TEM images of 1d_Fe-N@CMK-3 sample from SBA-15 template.*

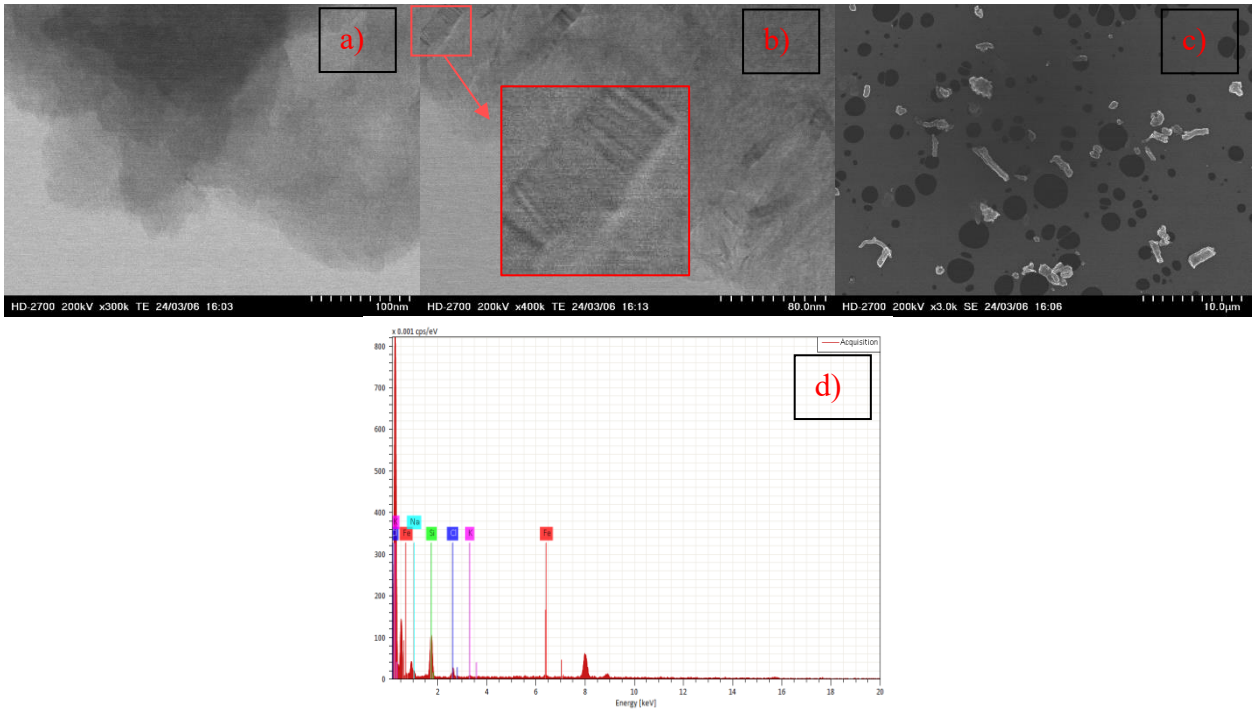

Figure 37. *(a),(b),(c),(d) STEM and EDS plot of the 2d_*Fe-N@CMK-3 *sample.*

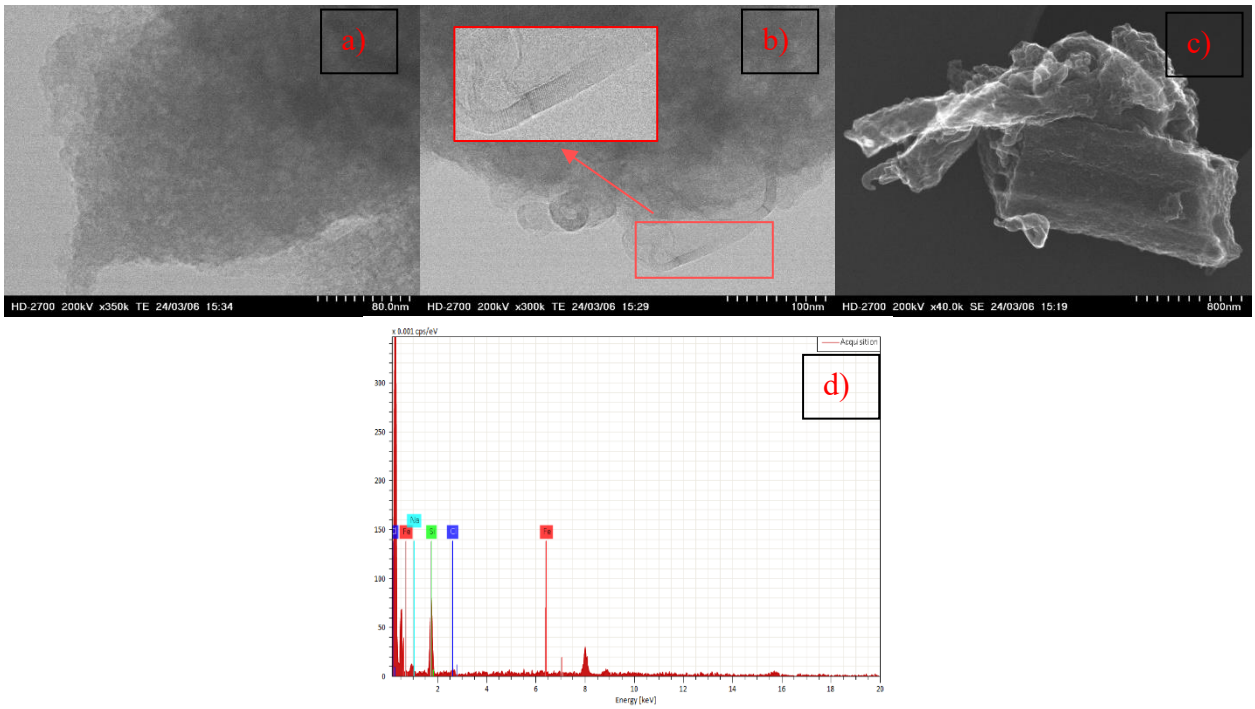

Figure 38. *(a),(b),(c),(d) STEM and EDS plot of the 3d_*Fe-N@CMK-3 *sample.*

Going further in the results, TEM images in figure 36 from 1d_Fe-N@CMK-3 revealed an extremely high amount of carbon nanotubes (figure (a)) as well as the presence of graphitic carbon (figure (b)) in agreement with the sharper peak at 26° discussed previously.

Samples 2d_Fe-N@CMK-3 and 3d_Fe-N@CMK-3 -synthesised following respectively the two impregnation steps in the pyrolyser under nitrogen flux and within the closed Teflon reactor- present a porous structure but, despite the theoretically enhanced impregnation, like the 1c_Fe-N@CMK-8 sample do not show any porous network arrangement as visible in figures 37 (a) and 38 (a).

Despite the lack of a well organised structure with respect to the silica template, from figures 36 (a), 37 (c), and 38 (c) it is evident that they mostly retained the rod-type macrostructure typical of the template. Additionally, all of them show the presence of carbon nanotubes (figures 36 (c), 37 (b), 38 (b)). More in details, in the magnifications highlighted in red, there also is the presence of bamboo-structured carbon nanotubes (BCNTs). Those consist of separated hollow compartments and "bamboo knots" which create a segmented structure, resembling bamboo stalks.
The open compartments in BCNTs facilitate mass transport of reactants and products to and from the iron atoms. This improves the reaction efficiency by ensuring a smoother flow of materials throughout the catalyst. [27]

However, from the EDS spectra (figures 37 (d), 38 (d)) it can be noticed that exactly like in the previous samples there is a relatively high amount of residual silica, as well as some chlorine and sodium from the etching processes.

4.2.4. Studying the effect of a second pyrolysis step – increasing the graphitisation degree

From the obtained results, it is evident that two problems humper the optimal structure and activity of the as-synthesised catalysts:

1. The presence of residual silica hard-template after pyrolysis and several etching steps;
2. The lack of ordered crystalline structure.

Moving forward, while trying to increase the degree of graphitisation and the crystallinity of the catalysts, a second pyrolysis step of 1 hour under nitrogen flow was performed to three of the samples. [37]
Nevertheless, in contrast to what expected from both PXRD plots in figure 39 , not only they did not get more ordered but, on the contrary, they lost their initial structure becoming just porous.

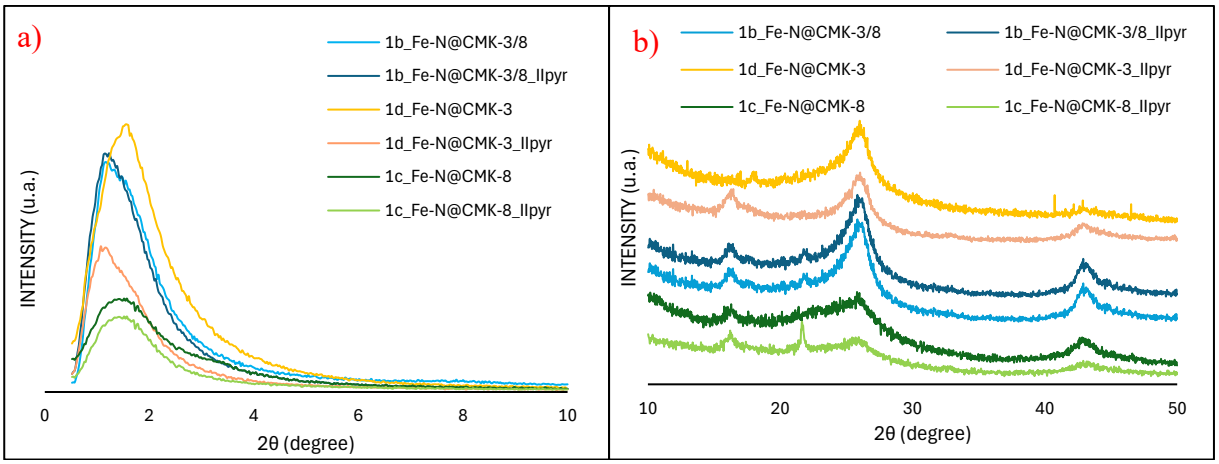

Figure 39. *(a),(b). Low and high angle XRD of II pyrolysed catalysts.*

Through a comparison between the samples pyrolysed once and twice, it can be noticed that on overall there is a decrease in the peak intensity, showing an increase in the amorphousness of all the samples, condition further proved by the STEM images of the Fe-N@CMK-3/8 in figure 40 where only few graphitic carbon agglomerations are present.
From 2a_Fe-N@CMK-8_IIpyr plot another sharp peak appears at 22°, relatable to SiO_2 still present into the material. [36]
For conciseness, only this material photos are reported, since all of them shows the same trend.

However, the main peaks appear to be in the same position (26° and 44°), both attributed to a certain degree of carbon graphitisation always related to the [002] and [100] planes.

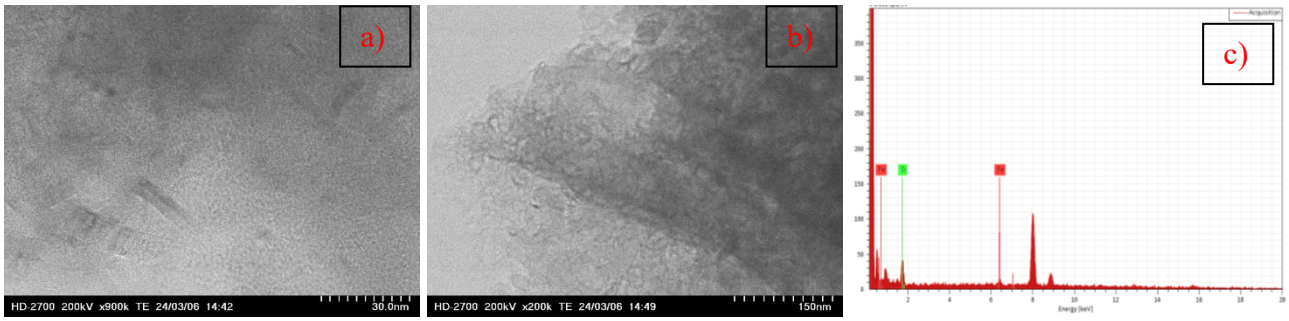

Figure 40. *(a),(b),(c). EDS and TEM images of the double pyrolysed Fe-CMK-3/8.*

4.3. Electrocatalytic performance in the Oxygen reduction reaction

The electrochemical tests of the as-synthesised catalysts were conducted in a three-electrode system with a rotating disk electrode (RDE), and with a rotating ring-disk electrode (RRDE) with a platinum ring as second working electrode.
The catalysts were deposited on the glassy carbon disk, with a surface area of 0.1256 cm^2.
The tests setup includes, as already discussed in the paragraph 1.3, the catalyst-coated disk and the platinum working electrodes, the counter electrode consisting of a graphitic carbon rod, and a reference electrode.
The first experimental part was performed in the US where the reference electrode was a reversible hydrogen electrode (RHE), while the second part was performed in Italy where the reference electrode was an Ag/AgCl one.
In the latter case, in order to make comparisons, the measured potential was rescaled to the RHE based on the Nernst equation.

The catalysts were firstly dispersed in a nafion/isopropanol solution, where the nafion works as a binder, and then drop-casted on the disk electrode.
For each catalyst the ink was prepared by mixing 2 mg of catalyst powder with 400 μl of isopropanol and 10 μl of Nafion perfluorinated resin solution (5 wt.%). The suspension was later sonicated for 10 minutes and then 10.3 μl of the ink were deposited on the glassy carbon disk to obtain the desired catalyst loading of 0.4 mg/cm^2. The coated electrode after deposition was then left in air to dry. [35]

The performed measurements are as listed, both in acid (0.1 M $HClO_4$) and alkaline environment (0.1 M KOH solution) :

1) cyclic voltammetry (CV) in both N_2 and O_2 at 100 mV/s after an initial fast one performed at 500 mV/s for 100 cycles in order to activate and clean the electrode surface from contaminants and/or oxides.
2) Linear sweep voltammetry (LSV) at 400, 900, 1600, and 2500 rounds per minute (rpm).
3) LSV at 1600 rpm in RRDE setup to evaluate the amount of H_2O_2 or $H_2O_2^-$ formed and the electrons involved in the ORR in acid or basic environment, respectively.

In addition, the disk currents were always normalised by the geometrical area of the disk (0.1256 cm^2).
It is worth mentioning that typically hydrogen-powered fuel cells operate at an average single-cell voltage within the range 0.8 – 0.6 V.

For ORR, the activity of the electrocatalysts was investigated in 0.1 M KOH (pH=13), and in 0.1 M HClO4 (pH=1) aqueous solutions saturated by bubbling O_2 or N_2.
The ORR activity of the electrocatalysts using RRDE experiments. The anodic polarisation curves were analysed to extract key descriptors of ORR performance: the onset potential (E_{onset}) at a current density of 0.1 mA/cm^2 and the half-wave potential ($E_{1/2}$) determined by the first-derivative method, while the number of electrons which take part to the ORR and the amount of hydrogen peroxide were evaluated through those two formulas: [38]

$$n = \frac{4\, I_d\, N}{I_d\, N + I_r} \qquad (25)$$

$$\%H_2O_2 = 100\frac{2\,I_r}{I_d\,N + I_r} \qquad (26)$$

Where I_d is the disk current, I_r is the ring current, and N is the collection efficiency function of the RRDE geometry and the diffusion properties of the reaction products.
More in detail, the N value for the Italy setup is equal to 0.4, while for the US setup is equal to 0.37.
As already said in the previous description, a value of n equal to 4 means that the 4e- pathway is realised and this correspond to the absence of hydrogen peroxide generation which is beneficial for performance. [38]
Higher values of E_{on} and $E_{1/2}$ are indicators of enhanced electrocatalytic activity, since a lower overpotential to achieve a determined value of current density is necessary.

4.3.1. Influence of the silica source on the catalytic activity

In the following figures (41 and 42), a first activity comparison between catalysts synthesised through the same impregnation protocol coming from the KIT-6-*p6mm,* KIT-6-*dual*, and SBA-15 silicas is presented.

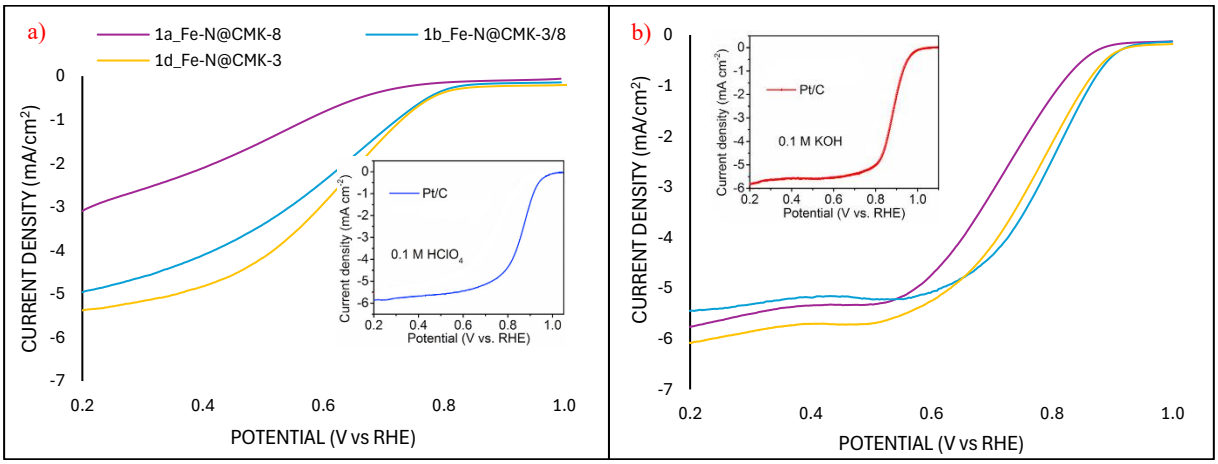

Figure 41. *Electrochemical performance measurements done in the US on RRDE and commercial Pt/C catalyst* [39]*: ORR polarisation curves at 1600 rpm. (a) in 0.1 M $HClO_4$ solution. (b) in 0.1 M KOH solution.*

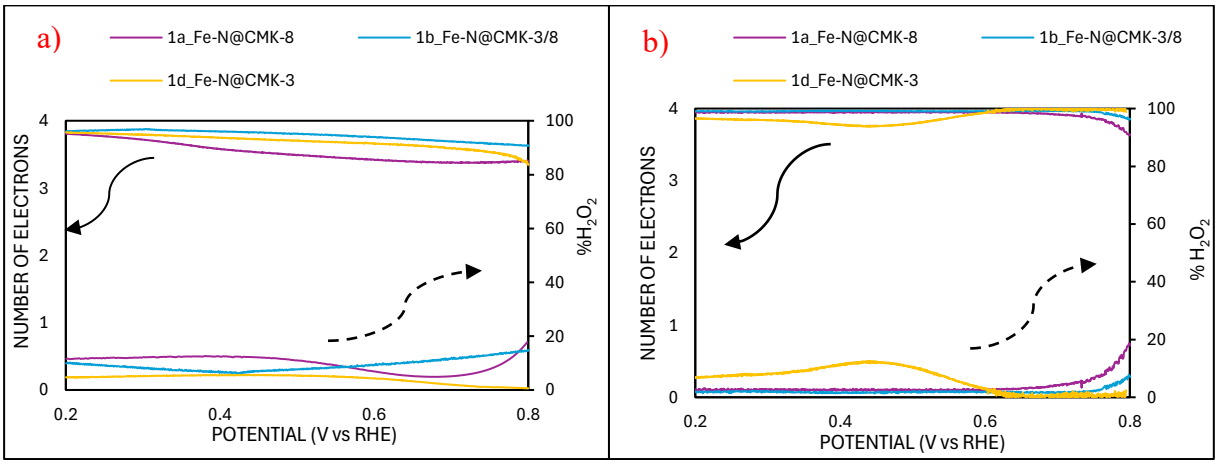

Figure 42. *Number of electrons and $\%H_2O_2$ from RRDE at 1600 rpm measurements. (a) in 0.1 M $HClO_4$ solution. (b) in 0.1 M KOH solution.*

Table 3. *ORR performance comparison of Fe-N-C catalysts tested in US and Pt/C 20% wt. in 0.1 M KOH and 0.1 M $HClO_4$ at 1600 rpm.* [39]

	E_{onset} (V vs. RHE)		$E_{1/2}$ (V vs. RHE)		$n_{average}$ (-)		$\%H_2O_{2,average}$ (-)	
	0.1 M KOH	0.1 M $HClO_4$	0.1 M KOH	0.1 M $HClO_4$	0.1 M KOH	0.1 M $HClO_4$	0.1 M KOH	0.1 M $HClO_4$
1a_Fe-N@CMK-8	0.87	0.69	0.75	0.6	3.93	3.49	3.60	10.91
1b_Fe-N@CMK-3/8	0.91	0.80	0.82	0.69	3.95	3.81	2.02	9.21
1d_Fe-N@CMK-3	0.91	0.89	0.8	0.64	3.87	3.74	3.61	4.17
Pt/C	0.90	0.96	0.82	0.88	3.99	3.99	0.35	0.49

The LSV curves from 1b_Fe-N@CMK-3/8 and 1d_Fe-N@CMK-3 show similar trend and values to that of commercial platinum catalyst in both acid and basic conditions.
Sample 1a_Fe-N@CMK-8 synthesised from KIT-6-*p6mm* show good results in basic condition, while in acid is less performant, result further confirmed by the values in table 3 where it shows the highest amount of hydrogen peroxide species and a number of electrons lower than the average.
On overall, the best Fe-N-C catalyst is 1d_Fe-N@CMK-3, whose E_{on} and $E_{1/2}$ in KOH are similar to those of the Pt/C one, while in $HClO_4$ the values are only 16 mV and 22 mV lower, respectively.
Considering the uniform synthesis method across all catalysts, the observed differences in ORR activity can be attributed to the influence of the C-support. It is hypothesised that using silica source with high specific surface area and more ordered porous structure promote the formation and accessibility of active sites for the reaction. [37]

4.3.2. Influence of the nanocasting approaches in KIT-6 derived samples on the catalytic activity

In this section the effect of the different nanocasting approaches described in protocol 1 and 2 in the section 2.2.2 on the catalytic activity is studied.
For a brief recap, sample 1a_Fe-N@CMK-8 and 1b_Fe-N@CMK-3/8 were synthesised respectively from KIT-6-*p6mm* and KIT-6-*dual* following the classic impregnation steps cited in protocol 1 of section 2.2.2, while 1c_Fe-N@CMK-8 derives from KIT-6 silica, and it was impregnated within the muffle furnace as described in protocol 2 of the same section.

Figure 43 provides the LSV curves of the cited samples, while figure 44 shows the number of electrons that participate at the reaction and the amount of H_2O_2 generated within the working potential range. Finally, in table 4 a summary of the performances respect to the commercial Pt/C is shown. [39]
Catalysts from protocol 1 show good results -especially 1b_Fe-N@CMK-3/8 as already discussed in section 3.4.1- and their average number of electrons participating to the ORR and the amount of H_2O_2 suggest the $4e^-$ pathway is mainly followed, demonstrating their good performance.
The catalytic performance of the sample 1c_Fe-N@CMK-8 reflects its worse morphological properties discussed in section 3.2.2 compared to the others: the better iron dispersion along the

carbon matrix (appearing from the absence of Fe clusters in the ZC image 31 (c)) is not enough to overcome the lack of a good porous network arrangement, confirming the mass transport limitations occurring in highly amorphous carbons. [37]
The E_{on} and $E_{1/2}$ values are between 20-30 mV lower compared to the other Fe-N-C catalysts, and figure 44 suggests that with this sample a 2+2 e^- pathway is mainly followed, also confirmed by the really high amount of hydrogen peroxide produced.

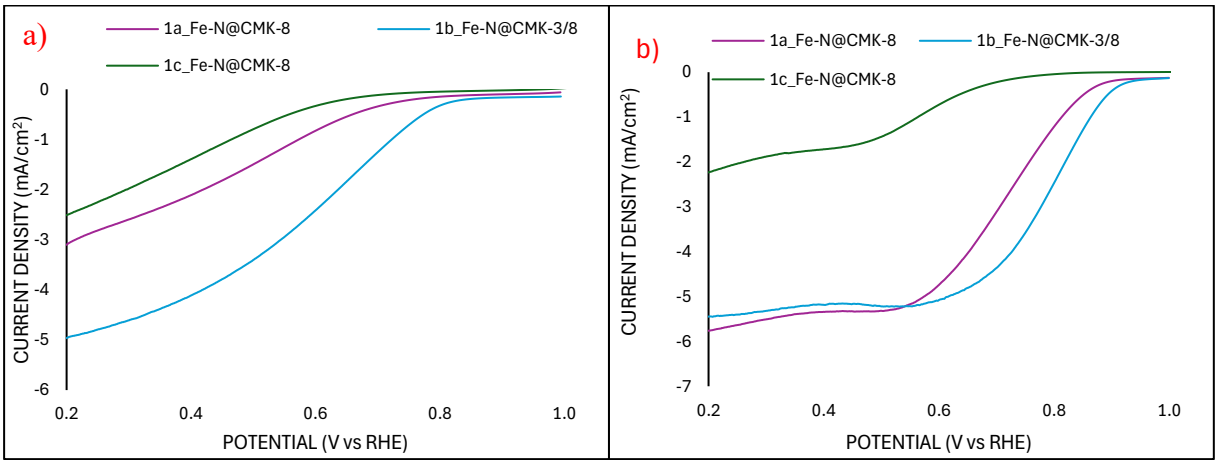

Figure 43. *Electrochemical performance measurements of the samples derived from KIT-6 templates. (a) in 0.1 M $HClO_4$ solution. (b) in 0.1 M KOH solution.*

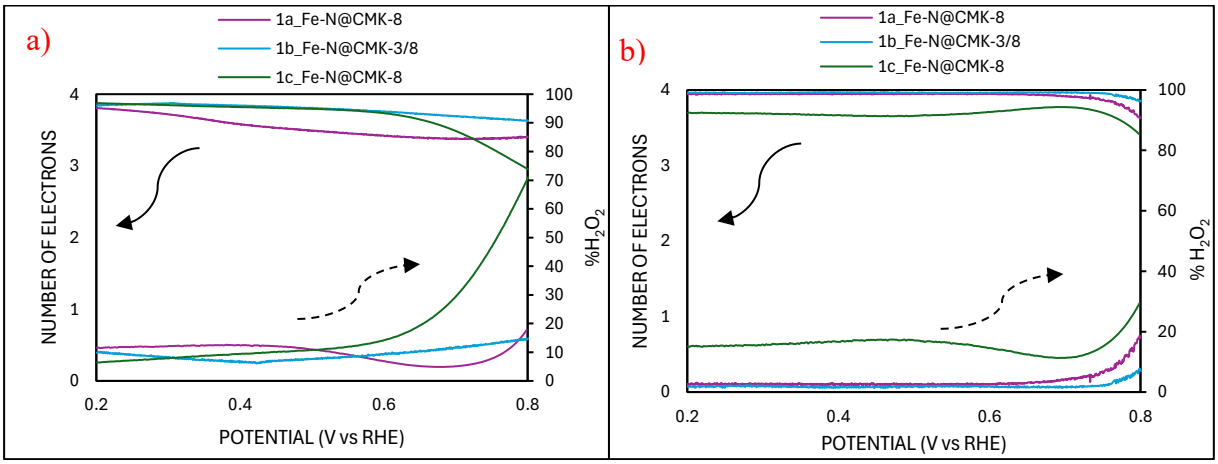

Figure 44. *Number of electrons and $\%H_2O_2$ from RRDE at 1600 rpm measurements. (a) in 0.1 M $HClO_4$ solution. (b) in 0.1 M KOH solution.*

Table 4. *ORR performance comparison of Fe-N-C catalysts from KIT-6 templates and Pt/C 20% wt. in 0.1 M KOH and 0.1 M $HClO_4$ at 1600 rpm.* [36]

	E_{on} (V vs. RHE)		$E_{1/2}$ (V vs. RHE)		$n_{average}$ (-)		$\%H_2O_{2,average}$ (-)	
	0.1 M KOH	0.1 M $HClO_4$	0.1 M KOH	0.1 M $HClO_4$	0.1 M KOH	0.1 M $HClO_4$	0.1 M KOH	0.1 M $HClO_4$
1a_Fe-N@CMK-8	0.87	0.69	0.75	0.6	3.93	3.49	3.60	10.91
1b_Fe-N@CMK-3/8	0.91	0.80	0.82	0.69	3.95	3.81	2.02	9.21
1c_Fe-N@CMK-8	0.68	0.61	0.56	0.43	3.68	3.70	15.68	17.80
Pt/C	0.90	0.96	0.82	0.88	3.99	3.99	0.35	0.49

4.3.3. Influence of the nanocasting approaches in SBA-15 derived samples on the catalytic activity

In figures 45 and 46 a comparison in the catalytic activity among samples synthesised from the same SBA-15 template with different impregnation processes is given, while table 5 gives a summary of the cited results.
Better activities are visible for 2d_Fe-N@CMK-3 and 3d_Fe-N@CMK-3 catalysts synthesised from SBA-15 template impregnated respectively under nitrogen flux and in the closed Teflon reactor compared to the KIT-6-derived discussed in section 3.4.2. More specifically, sample 3d_Fe-N@CMK-3 shows the best activity among the catalysts coming from protocols 2 and 3, thus the increased pressure within the closed reactor during thermal treatment actually allowed a better precursors diffusion.
However, the best catalyst appears to be 1d_Fe-N@CMK-3 from the classic synthesis route in protocol 1. This sample has nearly the same E_{on} and $E_{1/2}$ from Pt/C catalyst in alkaline electrolyte while in acid differ of only 16 mV and 24 mV, respectively.

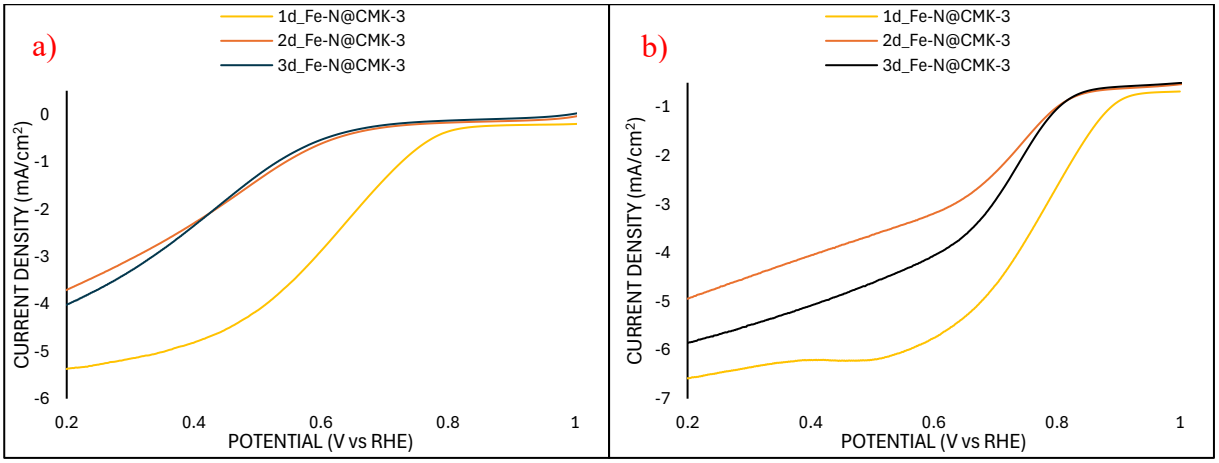

Figure 45. *Electrochemical performance measurements of the samples derived from SBA-15 templates. (a) in 0.1 M $HClO_4$ solution. (b) in 0.1 M KOH solution.*

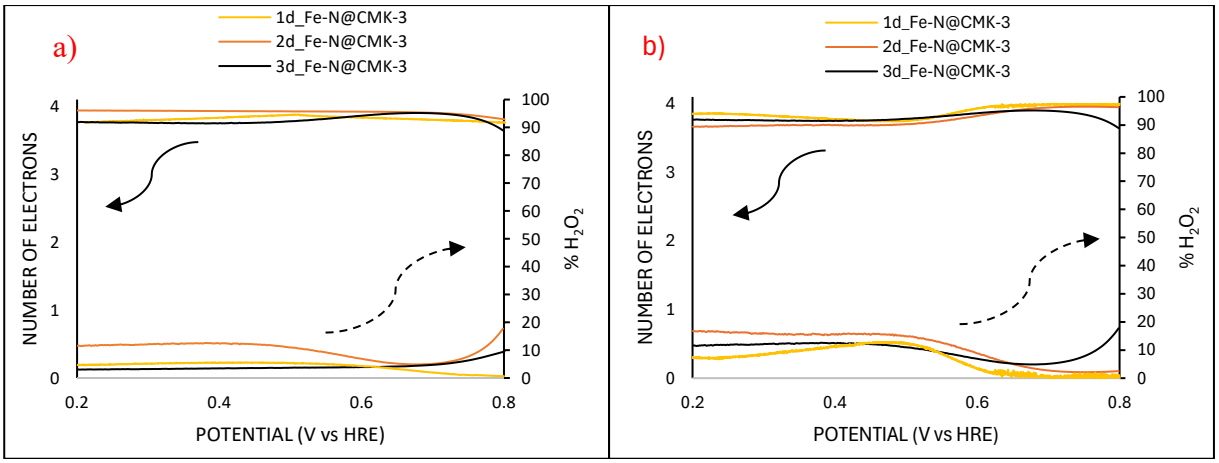

Figure 46. *Number of electrons and %H_2O_2 from RRDE at 1600 rpm measurements. (a) in 0.1 M $HClO_4$ solution. (b) in 0.1 M KOH solution.*

Table 5. *ORR performance comparison of Fe-N-C catalysts from SBA-15 templates and Pt/C 20% wt. in 0.1 M KOH and 0.1 M $HClO_4$ at 1600 rpm.* [39]

	E_{on} (V vs. RHE)		$E_{1/2}$ (V vs. RHE)		$n_{average}$ (-)		$\%H_2O_{2,average}$ (-)	
	0.1 M KOH	0.1 M $HClO_4$	0.1 M KOH	0.1 M $HClO_4$	0.1 M KOH	0.1 M $HClO_4$	0.1 M KOH	0.1 M $HClO_4$
1d_Fe-N@CMK-3	0.91	0.89	0.8	0.64	3.87	3.74	3.61	4.17
2d_Fe-N@CMK-3	0.81	0.62	0.75	0.42	3.77	3.91	11.26	4.12
3d_Fe-N@CMK-3	0.68	0.61	0.56	0.43	3.8	3.78	9.93	9.21
Pt/C	0.90	0.96	0.82	0.88	3.99	3.99	0.35	0.49

4.3.4. Studying the effect of a second pyrolysis step – increasing the graphitisation degree

In this last section, it has been compared the catalytic activity of the synthesised samples with the respective version pyrolysed twice in the attempt of enhance the crystallinity rate and better distribute the iron within the structure.

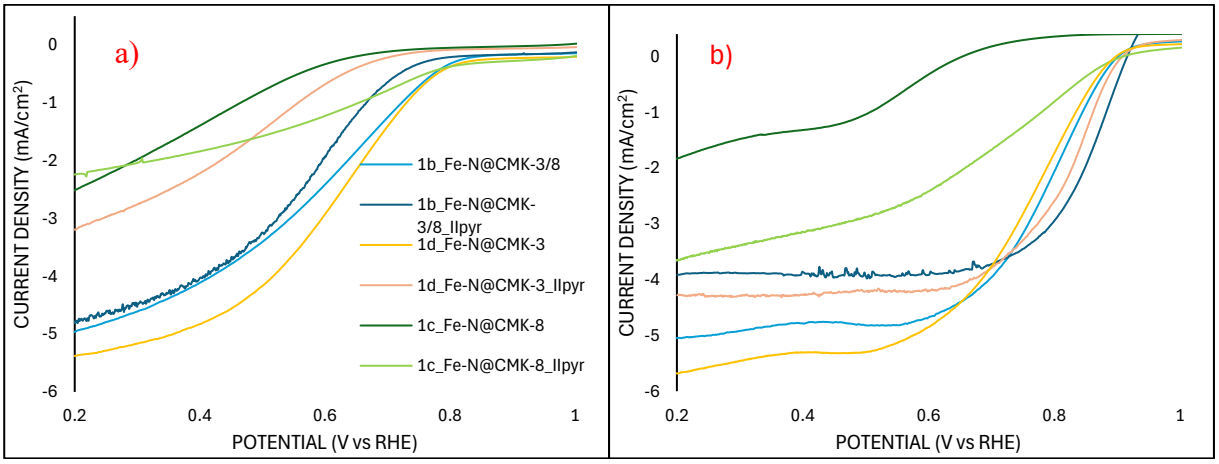

Figure 47. *Electrochemical performance measurements of the samples pyrolysed twice. (a) in 0.1 M $HClO_4$ solution. (b) in 0.1 M KOH solution.*

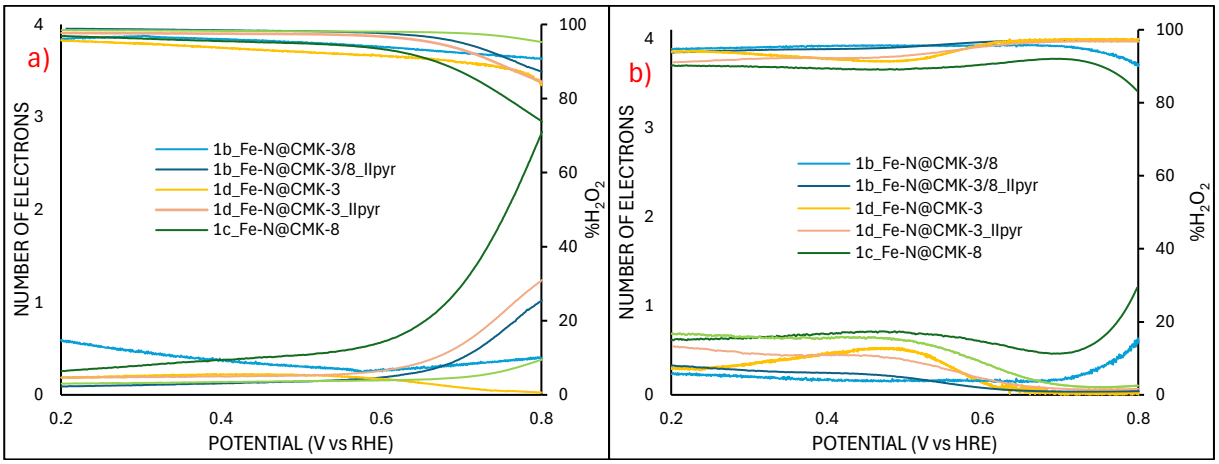

Figure 48. *Number of electrons and $\%H_2O_2$ from RRDE at 1600 rpm measurements. (a) in 0.1 M $HClO_4$ solution. (b) in 0.1 M KOH solution.*

Table 6. *ORR performance comparison of Fe-N-C catalysts pyrolysed once and twice and Pt/C 20% wt. in 0.1 M KOH and 0.1 M $HClO_4$ at 1600 rpm.* [39]

	E_{on} (V vs. RHE)		$E_{1/2}$ (V vs. RHE)		$n_{average}$ (-)		$\%H_2O_{2,average}$ (-)	
	0.1 M KOH	0.1 M $HClO_4$	0.1 M KOH	0.1 M $HClO_4$	0.1 M KOH	0.1 M $HClO_4$	0.1 M KOH	0.1 M $HClO_4$
1b_Fe-N@CMK-3/8	0.91	0.80	0.82	0.69	3.95	3.81	2.02	9.21
1b_Fe-N@CMK-3/8_IIpyr	0.93	0.71	0.81	0.49	3.91	3.88	4.11	6.14
1c_Fe-N@CMK-8	0.68	0.61	0.56	0.43	3.68	3.69	15.68	17.80
1c_Fe-N@CMK-8_IIpyr	0.88	0.8	0.25	0.22	3.77	3.91	11.24	4.11
1d_Fe-N@CMK-3	0.91	0.89	0.8	0.64	3.87	3.74	3.61	4.17
1d_Fe-N@CMK-3_IIpyr	0.68	0.61	0.56	0.43	3.85	3.83	7.53	8.62
Pt/C	0.90	0.96	0.82	0.88	3.99	3.99	0.35	0.49

Regarding the double pyrolysis step, in contrast to what expected from the overall decrease in the crystallinity rate after second pyrolysis, comparing the LSV data from figure 47 in both acid and basic conditions at the same rotation speed, a 20 mV higher onset potential appears for sample 1c_Fe-N@CMK-8_IIpyr with respect to the sample pyrolysed only once, while a decrease in the half wave potential occurs of almost the same value. The average number of electrons increased in both acid and alkali conditions, and a significant drop of 4.4% and 13.7% in the generated H_2O_2 have been recorded in alkali and acid electrolytes, respectively.
This can be linked to a better iron atoms redispersion and an increased graphitisation degree in the sample that was originally showing just a hint of porosity within the mesoporous structure, directly linked to a higher number of active sites provided for the ORR.
On the other two samples the results barely changed; the improvements showed in one electrolyte are balanced by a simultaneously worsening in the other one.
On overall, among these catalysts the most actives appear to be 1b_Fe-N@CMK-3/8 obtained from the dual mesoporous silica, immediately followed by 1d_Fe-N@CMK-3, since it has 250 mV higher E_{on} and 442 mV higher $E_{1/2}$ with respect to the less active one, which is 1c_Fe-N@CMK-8.

As a final comparison, in the following table 7 the Fe-N-C catalysts ORR activities from the state-of-the-art synthesised through different approaches are listed, demonstrating that the performance of the best synthesised catalysts (1b_Fe-N@CMK-3/8 and 1d_Fe-N@CMK-3) makes their use as cathodic catalyst in an PEMFC very promising.

Table 7. *ORR performances of catalysts from this work and from the literature.*

Electrocatalyst	Synthesis method and precursors	Electrolyte	E_{onset} vs RHE (V)	$E_{1/2}$ vs RHE (V)	Reference
1b_Fe-N@CMK-3/8	Sacrificial support methods from dual KIT-6 and SBA-15 + 1,10-phenanthroline	0.1 M $HClO_4$	0.80	0.69	This work
1d_Fe-N@CMK-3		0.1 M KOH	0.91	0.81	
NHMC (Fe-N-C)	Hybrid dual-templating: SiO_2 nanoparticles, F127 and iron-functionalized phenol-formaldehyde	0.5 M H_2SO_4	0.91	0.76	Deng et al. (40)
Fe-N/C-SAC	Molten salts mediated pyrolysis: nitrilotriacetic acid, iron acetylonate, KCl and $ZnCl_2$	0.1 M $HClO_4$	-	0.78	Xin et al. (41)
		0.1 M KOH	-	0.91	
Fe_3C/C-700	Fe3C nanoparticles encased by graphitic layers from ferrocene and cyanamide	0.1 M $HClO_4$	0.90	0.73	Hu et al. (42)
Fe_3C/C-800		0.1 M KOH	1.05	0.83	
FeNC-900	Sacrificial support method: SiO_2 nanospheres and Fe-doped ZIF-8 from MeIm, N,N-dimethylformamide, $Zn(NO_3)_2{\cdot}6H_2O$ and $FeSO_4{\cdot}7H_2O$	0.1 M $HClO_4$	0.84	0.71	Li et al. (43)
		0.1 M KOH	0.96	0.85	
FeN/MPC2	Sacrificial support method for the synthesis of a carbon support (MPC) for Fe^{III}–1,10-phenanthroline complex	0.5 M H_2SO_4	0.82	0.70	Osmieri et al. (19)
		0.1 M KOH	1.00	0.89	
3DOM Fe–N–C-900	Iron doped ZIF-8 from MeIm, $Zn(NO_3)_2{\cdot}6H_2O$, ferrocene and methanol	0.1 M $HClO_4$	-	0.78	Zhang et al. (44)
		0.1 M KOH	-	0.88	
Fe_{SA}-N-C	Iron doped porphyrinic MOF (PCN-222)	0.1 M $HClO_4$	0.93	0.78	Jiao et al. (45)
		0.1 M KOH	1.00	0.89	
Fe-NMP	Sacrificial support method: $Fe(NO_3)_3{\cdot}9H_2O$, pipemedic acid, nicarbazin, MeIm, urea, zinc, carbon nanotube and LM150 fumed silica	0.1 M KOH	0.97	0.84	Hossen et al. (46)
Fe-SAC/NC	Molten salt mediated pyrolysis: adenine, $ZnCl_2$, NaCl and Fe_2O_3	0.5 M H_2SO_4	0.80	0.69	Hu et al. (47)
		0.1 M KOH	0.95	0.84	
		0.1 M KOH	-	0.89	

Conclusions and future perspectives

In conclusion, this study explored the development of a non-precious metal-based catalyst for the oxygen reduction reaction (ORR) in fuel cells. The focus was on creating a catalyst with high activity and selectivity towards the 4-electron pathway, aiming to overcome the sluggish kinetics at the cathode and reduce the formation of hydrogen peroxide which affects efficiency. This approach aligns with the need for cost-effective and widely available clean energy technologies. The synthesised Fe-N-C catalyst exhibited good morphological characteristics, confirmed by nitrogen physisorption analysis, with a high surface area and appropriate pore size, also showing the crucial role played by the choice of the silica template and the followed nanocasting approach on the final results.

Looking forward, further research could investigate the impact of varying iron content within the catalyst on its performance. Additionally, optimising the etching process to completely remove the template and minimise silicon contamination is crucial to ensure the catalyst's true electrochemical behaviour.
From a commercial perspective, a life cycle assessment (LCA) and an economic feasibility analysis of large-scale production would provide valuable insights into the overall sustainability and practicality of this Fe-N-C catalyst compared to existing Pt-based alternatives.

BIBLIOGRAPHY

1. NASA CO2 [Internet]. [cited 2024 Jun 4]. Available from: https://climate.nasa.gov/vital-signs/carbon-dioxide/?intent=121#:~:text=Carbon%20dioxide%20%28CO%202%29%20is%20an%20important%20heat-trapping,from%20wildfires%2C%20and%20natural%20processes%20like%20volcanic%20eruptions.

2. Sun, T., Mitchell, S., Li, J., Lyu, P., Wu, X., Pérez-Ramírez, J., & Lu, J. (2021). Design of Local Atomic Environments in Single-Atom Electrocatalysts for Renewable Energy Conversions. In *Advanced Materials* (Vol. 33, Issue 5). Wiley-VCH Verlag. https://doi.org/10.1002/adma.202003075

3. Liang, Z., Zheng, H., & Cao, R. (2019). Importance of Electrocatalyst Morphology for the Oxygen Reduction Reaction. In *ChemElectroChem* (Vol. 6, Issue 10). https://doi.org/10.1002/celc.201801859

4. Yu, J., Su, C., Shang, L., & Zhang, T. (2023). Single-Atom-Based Oxygen Reduction Reaction Catalysts for Proton Exchange Membrane Fuel Cells: Progress and Perspective. In *ACS Nano* (Vol. 17, Issue 20). https://doi.org/10.1021/acsnano.3c06522

5. Singh, H., Zhuang, S., Ingis, B., Nunna, B. B., & Lee, E. S. (2019). Carbon-based catalysts for oxygen reduction reaction: A review on degradation mechanisms. In *Carbon* (Vol. 151). https://doi.org/10.1016/j.carbon.2019.05.075

6. Peighambardoust, S. J., Rowshanzamir, S., & Amjadi, M. (2010). Review of the proton exchange membranes for fuel cell applications. *International Journal of Hydrogen Energy*, *35*(17). https://doi.org/10.1016/j.ijhydene.2010.05.017

7. Garraín, D., Lechón, Y., & Rúa, C. de la. (2011). Polymer Electrolyte Membrane Fuel Cells (PEMFC) in Automotive Applications: Environmental Relevance of the Manufacturing Stage. *Smart Grid and Renewable Energy*, *02*(02). https://doi.org/10.4236/sgre.2011.22009

8. Zhang, J. (2008). PEM fuel cell electrocatalysts and catalyst layers: Fundamentals and applications. In *PEM Fuel Cell Electrocatalysts and Catalyst Layers: Fundamentals and Applications*. https://doi.org/10.1007/978-1-84800-936-3

9. Bhuvanendran, N., Ravichandran, S., Xu, Q., Maiyalagan, T., & Su, H. (2022). A quick guide to the assessment of key electrochemical performance indicators for the oxygen reduction reaction: A comprehensive review. In *International Journal of Hydrogen Energy* (Vol. 47, Issue 11). https://doi.org/10.1016/j.ijhydene.2021.12.072

10. He, C., Sankarasubramanian, S., Matanovic, I., Atanassov, P., & Ramani, V. (2019). Front Cover: Understanding the Oxygen Reduction Reaction Activity and Oxidative Stability of Pt Supported on Nb-Doped TiO 2 (ChemSusChem 15/2019) . *ChemSusChem*, *12*(15). https://doi.org/10.1002/cssc.201902005

11. Humayun, M., Israr, M., Khan, A., & Bououdina, M. (2023). State-of-the-art single-atom catalysts in electrocatalysis: From fundamentals to applications. In *Nano Energy* (Vol. 113). https://doi.org/10.1016/j.nanoen.2023.108570

12. Ozoemena, K. I. (2016). Nanostructured platinum-free electrocatalysts in alkaline direct alcohol fuel cells: Catalyst design, principles and applications. In *RSC Advances* (Vol. 6, Issue 92). https://doi.org/10.1039/c6ra15057h

13. Maruccia, E., Lourenço, M. A. O., Priamushko, T., Bartoli, M., Bocchini, S., Pirri, F. C., Saracco, G., Kleitz, F., & Gerbaldi, C. (2022). Nanocast nitrogen-containing ordered mesoporous carbons from glucosamine for selective CO2 capture. *Materials Today Sustainability*, *17*. https://doi.org/10.1016/j.mtsust.2021.100089

14. Priamushko, T., Guillet-Nicolas, R., & Kleitz, F. (2019). Mesoporous nanocast electrocatalysts for oxygen reduction and oxygen evolution reactions. In *Inorganics* (Vol. 7, Issue 8). https://doi.org/10.3390/inorganics7080098

15. Yamauchi, Y., & Kuroda, K. (2008). Rational design of mesoporous metals and related nanomaterials by a soft-template approach. In *Chemistry - An Asian Journal* (Vol. 3, Issue 4). https://doi.org/10.1002/asia.200700350

16. Kleitz, F., Choi, S. H., & Ryoo, R. (2003). Cubic Ia3d large mesoporous silica: Synthesis and replication to platinum nanowires, carbon nanorods and carbon nanotubes. *Chemical Communications*, *3*(17). https://doi.org/10.1039/b306504a

17. Kim, T. W., Kleitz, F., Paul, B., & Ryoo, R. (2005). MCM-48-like large mesoporous silicas with tailored pore structure: Facile synthesis domain in a ternary triblock copolymer-butanol-water system. *Journal of the American Chemical Society*, *127*(20). https://doi.org/10.1021/ja042601m

18. Guillet-Nicolas, R., Bérubé, F., Thommes, M., Janicke, M. T., & Kleitz, F. (2017). Selectively tuned pore condensation and hysteresis behavior in mesoporous SBA-15 silica: Correlating material synthesis to advanced gas adsorption analysis. *Journal of Physical Chemistry C*, *121*(39). https://doi.org/10.1021/acs.jpcc.7b06745

19. Osmieri, L. (2019). Transition metal–nitrogen–carbon (M–N–C) catalysts for oxygen reduction reaction. Insights on synthesis and performance in polymer electrolyte fuel cells. In *ChemEngineering* (Vol. 3, Issue 1). https://doi.org/10.3390/chemengineering3010016

20. Wang, S., Feng, S. Y., Zhao, C. C., Zhao, T. T., Tian, Y., & Yan, L. K. (2023). Regulating Efficient and Selective Single-atom Catalysts for Electrocatalytic CO2 Reduction. *ChemPhysChem*, *24*(19). https://doi.org/10.1002/cphc.202300397

21. Xiong, Y., Li, H., Liu, C., Zheng, L., Liu, C., Wang, J. O., Liu, S., Han, Y., Gu, L., Qian, J., & Wang, D. (2022). Single-Atom Fe Catalysts for Fenton-Like Reactions: Roles of Different N Species. *Advanced Materials*, *34*(17). https://doi.org/10.1002/adma.202110653

22. Bunaciu, A. A., Udriştioiu, E. gabriela, & Aboul-Enein, H. Y. (2015). X-Ray Diffraction: Instrumentation and Applications. In *Critical Reviews in Analytical Chemistry* (Vol. 45, Issue 4). https://doi.org/10.1080/10408347.2014.949616

23. Loganathan, S., Valapa, R. B., Mishra, R. K., Pugazhenthi, G., & Thomas, S. (2017). Thermogravimetric Analysis for Characterization of Nanomaterials. In *Thermal and Rheological Measurement Techniques for Nanomaterials Characterization* (Vol. 3). https://doi.org/10.1016/B978-0-323-46139-9.00004-9

24. Sotomayor, F. J., Cychosz, K. A., & Thommes, M. (2018). Characterization of Micro/Mesoporous Materials by Physisorption: Concepts and Case Studies. In *Acc. Mater. Surf. Res* (Vol. 3, Issue 2).

25. Alothman, Z. A. (2012). A review: Fundamental aspects of silicate mesoporous materials. In *Materials* (Vol. 5, Issue 12). https://doi.org/10.3390/ma5122874

26. Ponce, A., Mejía-Rosales, S., & José-Yacamán, M. (2012). Scanning transmission electron microscopy methods for the analysis of nanoparticles. *Methods in Molecular Biology*, *906*. https://doi.org/10.1007/978-1-61779-953-2_37

27. Thommes, M., Kaneko, K., Neimark, A. v., Olivier, J. P., Rodriguez-Reinoso, F., Rouquerol, J., & Sing, K. S. W. (2015). Physisorption of gases, with special reference to the evaluation of surface area and pore size distribution (IUPAC Technical Report). *Pure and Applied Chemistry*, *87*(9–10). https://doi.org/10.1515/pac-2014-1117

28. Kleitz, F., Bérubé, F., Guillet-Nicolas, R., Yang, C. M., & Thommes, M. (2010). Probing adsorption, pore condensation, and hysteresis behavior of pure fluids in three-dimensional cubic mesoporous KIT-6 silica. *Journal of Physical Chemistry C*, *114*(20). https://doi.org/10.1021/jp909836v

29. Chakrabarti, A., Lu, J., Skrabutenas, J. C., Xu, T., Xiao, Z., Maguire, J. A., & Hosmane, N. S. (2011). Conversion of carbon dioxide to few-layer graphene. *Journal of Materials Chemistry*, *21*(26). https://doi.org/10.1039/c1jm11227a

30. Freitas, W. da S., Pico, P. P. M., D'epifanio, A., & Mecheri, B. (2021). Nanostructured Fe-N-C as bifunctional catalysts for oxygen reduction and hydrogen evolution. *Catalysts*, *11*(12). https://doi.org/10.3390/catal11121525

31. Bradley MS. TGA-IR Analysis Using the OMNIC Mercury TGA Software.

32. Sing, K. S. W., & Williams, R. T. (2004). Physisorption hysteresis loops and the characterization of nanoporous materials. *Adsorption Science and Technology*, *22*(10). https://doi.org/10.1260/0263617053499032

33. Sotomayor, F. J., Cychosz, K. A., & Thommes, M. (2018). Characterization of Micro/Mesoporous Materials by Physisorption: Concepts and Case Studies. In *Acc. Mater. Surf. Res* (Vol. 3, Issue 2).

34. Siburian, R., Sihotang, H., Lumban Raja, S., Supeno, M., & Simanjuntak, C. (2018). New route to synthesize of graphene nano sheets. *Oriental Journal of Chemistry*, *34*(1). https://doi.org/10.13005/ojc/340120

35. Das, R., Hamid, S., Ali, Md., Ramakrishna, S., & Yongzhi, W. (2014). Carbon Nanotubes Characterization by X-ray Powder Diffraction – A Review. *Current Nanoscience*, *11*(1). https://doi.org/10.2174/15734137106661408182100 43

36. Liang, Y., Ouyang, J., Wang, H., Wang, W., Chui, P., & Sun, K. (2012). Synthesis and characterization of core-shell structured SiO 2 @YVO 4 :Yb 3+ ,Er 3+ microspheres. *Applied Surface Science*, *258*(8). https://doi.org/10.1016/j.apsusc.2011.12.006

37. Osmieri, L., Escudero-Cid, R., Armandi, M., Monteverde Videla, A. H. A., García Fierro, J. L., Ocón, P., & Specchia, S. (2017). Fe-N/C catalysts for oxygen reduction reaction supported on different carbonaceous materials. Performance in acidic and alkaline direct alcohol fuel cells. *Applied Catalysis B: Environmental*, *205*. https://doi.org/10.1016/j.apcatb.2017.01.003

38. Xing, W., Yin, G., & Zhang, J. (2014). Rotating Electrode Methods and Oxygen Reduction Electrocatalysts. In *Rotating Electrode Methods and Oxygen Reduction Electrocatalysts*. https://doi.org/10.1016/C2012-0-06455-1

39. Pu, Z., Cheng, R., Zhao, J., Hu, Z., Li, C., Li, W., Wang, P., Amiinu, I. S., Wang, Z., Min Wang, Chen, D., & Mu, S. (2020). Anion-Modulated Platinum for High-Performance Multifunctional Electrocatalysis toward HER, HOR, and ORR. *IScience*, *23*(12). https://doi.org/10.1016/j.isci.2020.101793

40. Deng, C., Pan, L., Ji, F., Du, W., Zhang, J., Sun, Y., & Zhong, H. (2021). Hybrid dual-template induced nitrogen-doped hierarchically porous carbon as highly efficient oxygen reduction electrocatalyst. *International Journal of Hydrogen Energy*, *46*(73). https://doi.org/10.1016/j.ijhydene.2021.08.156

41. Xin, C., Shang, W., Hu, J., Zhu, C., Guo, J., Zhang, J., Dong, H., Liu, W., & Shi, Y. (2022). Integration of Morphology and Electronic Structure Modulation on Atomic Iron-Nitrogen-Carbon Catalysts for Highly Efficient Oxygen Reduction. *Advanced Functional Materials*, *32*(2). https://doi.org/10.1002/adfm.202108345

42. Hu, Y., Jensen, J. O., Zhang, W., Cleemann, L. N., Xing, W., Bjerrum, N. J., & Li, Q. (2014). Hollow spheres of iron carbide nanoparticles encased in graphitic layers as oxygen reduction catalysts. *Angewandte Chemie - International Edition*, *53*(14). https://doi.org/10.1002/anie.201400358

43. Li, Z., Liang, X., Gao, Q., Zhang, H., Xiao, H., Xu, P., Zhang, T., & Liu, Z. (2019). Fe, N co-doped carbonaceous hollow sphere with self-grown carbon nanotubes as a high performance binary electrocatalyst. *Carbon*, *154*. https://doi.org/10.1016/j.carbon.2019.08.036

44. Zhang, X., Han, X., Jiang, Z., Xu, J., Chen, L., Xue, Y., Nie, A., Xie, Z., Kuang, Q., & Zheng, L. (2020). Atomically dispersed hierarchically ordered porous Fe–N–C electrocatalyst for high performance electrocatalytic oxygen reduction in Zn-Air battery. *Nano Energy*, *71*. https://doi.org/10.1016/j.nanoen.2020.104547

45. Jiao, L., Wan, G., Zhang, R., Zhou, H., Yu, S. H., & Jiang, H. L. (2018). From Metal–Organic Frameworks to Single-Atom Fe Implanted N-doped Porous Carbons: Efficient Oxygen Reduction in Both Alkaline and Acidic Media. *Angewandte Chemie - International Edition*, *57*(28). https://doi.org/10.1002/anie.201803262

46. Hossen, M. M., Artyushkova, K., Atanassov, P., & Serov, A. (2018). Synthesis and characterization of high performing Fe-N-C catalyst for oxygen reduction reaction (ORR) in Alkaline Exchange Membrane Fuel Cells. *Journal of Power Sources*, *375*. https://doi.org/10.1016/j.jpowsour.2017.08.036

47. Hu, J., Wu, D., Zhu, C., Hao, C., Xin, C., Zhang, J., Guo, J., Li, N., Zhang, G., & Shi, Y. (2020). Melt-salt-assisted direct transformation of solid oxide into atomically dispersed FeN4 sites on nitrogen-doped porous carbon. *Nano Energy*, *72*. https://doi.org/10.1016/j.nanoen.2020.104670